OPTICAL NONLINEAR PROPERTIES OF NOVEL TWO DIMENSIONAL TRANSITION METAL DICHALCOGENIDES

TANG CHUN YIN

PhD

The Hong Kong Polytechnic University

2020

The Hong Kong Polytechnic University

Department of Applied Physics

OPTICAL NONLINEAR PROPERTIES OF NOVEL TWO DIMENSIONAL TRANSITION METAL DICHALCOGENIDES

Tang Chun Yin

A thesis submitted in partial fulfilment of the requirements for the

degree of Doctor of Philosophy

February 2020

CERTIFICATE OF ORIGINALITY

I hereby declare that this thesis is my own work and that, to the best of my knowledge and belief, it reproduces no material previously published or written, nor material that has been accepted for the award of any other degree or diploma, except where due acknowledgment has been made in the text.

_____ (Signed)

Tang Chun Yin (Name of student)

Abstract

Apart from the development of scientific theories and mechanisms, the sustained investigation on the material properties of newly synthesised substance had also underpinned the advancement of modern technology. In the optical aspect, according to the evolution of high power pulsed laser, it had opened up a new research branch on the material optical properties, which is known as nonlinear optics. Under the illumination of high-intensity light, the optical response of nonlinear materials show unique phenomenons as compared to that observed in conventional optics, for instance, incident light intensity-dependent absorbance and wavelength modulation of the output light. In the same time, these unique nonlinear properties of the novel materials can be applied to synthesise advanced optical devices, including saturable absorber for inducing laser pulses with pico- to femtosecond pulse duration, and photonic crystal fibre for supercontinuum generation. Therefore, the exploration and investigation of novel nonlinear materials is a vital test for promoting modern optics development.

Contributed by the works on graphene, it had motivated the study on low-dimensional materials in the past two decades, for example, two-dimensional layered material, nanotube, and quantum dot. The previous literature had shown that these nanomaterials possess superior material properties, such as high charge carrier mobility and mechanical strength, especially strong nonlinear optical response. In this work, the research objective is mainly focused on the exploration of the nonlinear optical properties of novel two-dimensional layered transition metal dichalcogenides(TMDs), where the TMDs materials were applied as the

saturable absorber(SA) and installed into different laser cavity to induce ultrashort laser pulses generation. The applied laser systems include of diode-end-pumped solid-state (DPSS) Nd: YVO$_4$ laser and Erbium-doped fiber laser (EDFL). The studies on nonlinear optical absorption(NOA) properties of TMDs materials began with the promising nonlinear group 6 tungsten disulfide (WS$_2$).

The WS$_2$ saturable absorber was inserted within a DPSS Nd: YVO$_4$ laser cavity to test the corresponding NOA properties. In the experiment, Q-switched operation was demonstrated, where maximum single pulse energy of 145 nJ was achieved and is comparable to the results of other WS$_2$-SA-based Q-switched lasers. This work has enriched the understanding of the applicability of WS$_2$-SA in diverse laser systems. Meanwhile, in the synthesis process, experiences of TMDs material properties modulation were obtained. The synthesis parameters, such as the thickness of the precursor thin film, post-annealing time and temperature profile will significantly affect to the TMDs nanosheets growth direction, crystalline structure and stoichiometry ratio of the synthesised thin film. These experiences had built the foundation of the successor works of applying vertically aligned group 10 TMDs to fabricate high-efficient photodetector and image sensor, which was demonstrated and published in high-quality Journal.

Remarkably, the NOA study had also extended to group 10 air-stable TMDs candidates, which both platinum disulfide (PtS$_2$) and platinum ditelluride (PtTe$_2$) saturable absorber-based passively mode-locked EDFLs were experimentally demonstrated. The achieved pulse duration of the mode-locked EDFLs are 2.064 ps and 1.66 ps corresponding to the PtS$_2$ and PtTe$_2$ saturable absorber, respectively, which are comparable to other low dimensional materials-based results. It indicates that both of the platinum-based TMDs can apply as a promising nonlinear

saturable absorber. To the best of our knowledge, the demonstrations of mode-locked EDFLs based on PtS_2 and $PtTe_2$ saturable absorber are a pioneer study within the nonlinear photonic field and has not been reported previously.

Furthermore, the NOA dependence on the lateral size and layer thickness of PtS_2 nanosheets was also demonstrated. By using the individual centrifugation method with distinct centrifugal forces, four PtS_2-NMP suspension samples with different distributions of lateral dimension and thickness were prepared. By the Z-scan measurement, it shows that as the PtS_2 nanosheets lateral dimension and layer thickness reduced, it will enhance the excited state photon absorption (ESA) effect and two-photon absorption (TPA) effect, which promoted the reverse saturable absorption (RSA) response of the PtS_2 samples. If the RSA response of the nonlinear sample is already close to the saturation limit, further enhancement of photon absorption will result in a weakening of the RSA response, and eventually induced a change of the NOA behavior from RSA to saturable absorption response. This work provides the method and strategy for further optimising the group 10 Pt/Pd-based saturable absorber performance by modifying the morphological features of the TMDs nanosheets.

List of publications

Journal Publications

1. **<u>C. Y. Tang</u>**, P. K. Cheng, L. Tao, H. Long, L. H. Zeng, Q. Wen, and Y. H. Tsang, "Passively Q-Switched Nd:YVO$_4$ Laser Using WS$_2$ Saturable Absorber Fabricated by Radio Frequency Magnetron Sputtering Deposition," IEEE Journal of Lightwave Technology 35(19), 4120-4124 (2017).

2. **<u>C. Y. Tang</u>***, P. K. Cheng*, X. Y. Wang, H. Long, and Y. H. Tsang, "Size-Dependent Nonlinear Optical Properties of Atomically Thin PtS$_2$ nanosheet," Optical materials 101, 109694(2020). (***Co-First/Equal contribution**)

3. **<u>C. Y. Tang</u>***, P. K. Cheng*, W. X. Yu, D. Xu, L. Wu, C. Yan and Y. H. Tsang, "Passively Q-switched and mode-locked Erbium-doped fiber laser based on two dimensional layered Platinum Ditelluride (PtTe$_2$) saturable absorber," In submission phase (***Co-First/Equal contribution**)

4. H. Long*, **<u>C. Y. Tang*</u>**, P. K. Cheng, X. Y. Wang, W. Qarony, and Y. H. Tsang, "Ultrafast Laser Pulses Generation by Using 2D Layered PtS$_2$ as a Saturable Absorber," IEEE Journal of Lightwave Technology 37(4), 1174–1179(2019). (***Co-First/Equal contribution**)

5. P. K. Cheng*, **<u>C. Y. Tang</u>***, X. Y. Wang, H. Long, and Y. H. Tsang, "Passively Q-switched Ytterbium-doped fiber laser based on broadband multilayer Platinum Ditelluride (PtTe$_2$) saturable absorber," Scientific reports 9 (2019). (***Co-First/Equal contribution**)

6. P. K. Cheng*, **<u>C. Y. Tang</u>***, W. X. Yu, L. H. Zeng, and Y. H. Tsang, "Passively Q-switched and Femtosecond mode locked Erbium-doped fiber laser based on 2D Palladium Disulfide (PdS$_2$) saturable absorber," Photonic research, accepted (2020) (***Co-First/Equal contribution**)

7. X.Y. Wang, P. K. Cheng, **<u>C.Y. Tang</u>**, H. Long, H. Yuan, L. Zeng, S. Ma, W. Qarony, and Y. H. Tsang, "Laser Q-switching with PtS$_2$ microflakes saturable absorber," Optics Express 26, (10), 13055-13060 (2018).

Conferences Publications:

1. **<u>C. Y. Tang</u>**, P. K. Cheng, L. Tao, Y. H. Tsang "Pulsed laser photonic based on novel two dimensional group-10 transition metal dichalcogenides," SPIE Nanoscience Engineering (2019)

Acknowledgments

I want to express my gratitude to my chief supervisor **Dr Y. H. Tsang** for their excellent guidance and constant encouragement throughout my research. Their high requirement, profound academic insight, and inspired discussions greatly contribute to improving the quality of my Ph.D. research.

I would also like to thank Prof. S. F. Yu, Dr C. L. Mak and Dr X. M. Zhang for their assistance on my Ph.D. research.

I want to give my thanks to my research group members, Mr G. X. Bai, Ms H. Long, Dr Lili Tao for their great help in my experiments.

Finally, I would like to thank my parents for their support of my research study and life.

Table of contents

CHAPTER 4

Passively Q-switched and mode-locked fibre laser based on group-10 TMDs-SA

LIST OF FIGURES

LIST OF TABLES

CHAPTER 1
Introduction

1.1 Background and Motivation

Light is one of the most important forms of energy. Since the beginning of civilisation, the study and manipulation of light are always a sustained quest among human society. The advancement of laser system underpinned the foundation of extensive modern technologies, for instance, optical communication, astronomic observation, medicine, and even military system [1-4]. Remarkably, the utilisation of laser also deepened the fundamental understanding of the nonlinear optics and broadened the corresponding applications.

Nonlinear optics studies and describes how the matter interacts with intense light, e.g. laser [5]. In the view of conventional optics, the optical properties of a material respond linearly to the magnitude of electric field E of the interaction light. However, if the intensity of the incident light scaled-up dramatically, the optical response of the material system will shift to a nonlinear manner and simultaneously exhibit different nonlinear optical effects, such as optical limiting [6], saturable absorption [7-9], self-focusing [10-11], and high-order harmonic generation [12]. Noticeably, depending on different nonlinear optical effects, the resultant optical characteristics of light will change after interacting with the nonlinear material. The study on nonlinear optics has shown a mutual and inseparable bonding with the diverse development of advanced laser systems.

In the past few decades, the evolution of saturable absorber (SA) has drawn enormous attention due to their applications of ultrafast laser pulses generation and the capability of these laser pulses used for high-precision material processing. In fact, the ultrafast laser can also be used for laser processing of high-end electronic components [13-14], biology tissue [15], and even transparent material [16]. The saturable absorber is a nonlinear optical device in which the corresponding absorbance is greatly reduced as illuminated by intense light [7-9]. This nonlinear phenomenon is known as the saturable absorption effect. Integration of SA within the laser cavity can induce either passive mode-locking [8-9] or passive Q-switching [17-18] operation, and consequently, generate laser pulses with pulse duration ranged from nano- to femtosecond. Compared to the counterpart of active operation, which complicated and costly Acousto-Optical or Electro-Optical Modulators (AOM/EOM) is required to control the intracavity loss, the passively Q-switched and mode-locked laser systems have shown the merits of simplicity, compactness, and cost-effectiveness [19-20]. Therefore, SA is one of the mainstream methods used in commercial laser systems nowadays.

However, an important question comes, what is the best nonlinear material for making these commercial SAs? Perhaps, there is no definite answer. Previously, doped crystals (e.g. Co^{2+}: MALO [21] and Cr^{4+}: YAG [22]) and semiconductor saturable absorber mirror (SESAM, e.g. InGaAs [23]) are the most commonly utilised commercial SAs for inducing either passively Q-switched or mode-locked operation, respectively. Nevertheless, the corresponding fabrication methods generally involve lengthy and costly crystal growth processes, for instance, metal oxide chemical vapor deposition (MOCVD). Undoubtedly, the involved high-cost

and complicated synthesis processes will limit the utilisation of these corresponding pulsed laser systems [24]. Besides, the operation bandwidths of doped crystal and SESAM are restricted to narrow range as originated from the material natural properties, which also reduced the flexibility and applicability of these SAs [25]. Therefore, the exploration of novel substitutional nonlinear material for SA synthesis is a sustained and attractive topic in pulsed laser development.

Contributed by the previous research works of graphene, it had unveiled the tremendous application potential of the novel low-dimensional materials, including laser pulses generation. The nonlinear saturable absorption properties of carbon-based low-dimensional materials were extensively investigated and demonstrated, for instance, graphene [26-27], graphene oxide [28-29], reduced graphene oxide [29], and carbon nanotube [30-31]. Furthermore, other graphene-like two dimensional (2D) layered materials, such as transition metal dichalcogenides (TMDs) have also drawn considerable attention due to the outstanding material properties, for instance, broadly tunable bandgap, high charge carrier mobility, strong mechanical strength, and prominent nonlinear optical (NLO) response [32-35]. 2D layered TMDs have a stoichiometry of MX_2. M represents the group 4 to 10 transition metals (e.g. Nb, Mo, W, Re), and X stands for the chalcogen atoms (S, Se, Te). As shown in Fig. 1.1, the TMD layers are weakly bound together by van der Waals force [36]. Few-layer TMD can be obtained by processing mechanical exfoliation, e.g. scotch tape method, to the bulky TMDs crystal or utilizing bottom-up approaches methods, e.g. CVD growth. The study of the NLO properties of TMDs can be traced back to 2013, where Wang

et. al. demonstrated the strong nonlinear saturable absorption property of MoS_2 by using the Z-scan technique [37]. Afterwards, the study of the saturable absorption property has extended to other TMDs and dominated within the group 6 families, such as $MoSe_2$ [38-39], WS_2, and WSe_2 [40]. Meanwhile, literature also demonstrated that the NLO properties of TMDs can be modulated by modifying the material lateral size, the number of layers [41-42], stoichiometry ratio [24], and concentration [43]. Up to the present, as a 2D group of 40+ layered materials, the explored TMDs-SAs only occupied a small portion in the TMDs family. Thus, It is worth to further extend the SA exploration scope to other potential TMDs candidates, which will lead to fruitful results in the nonlinear optics field eventually.
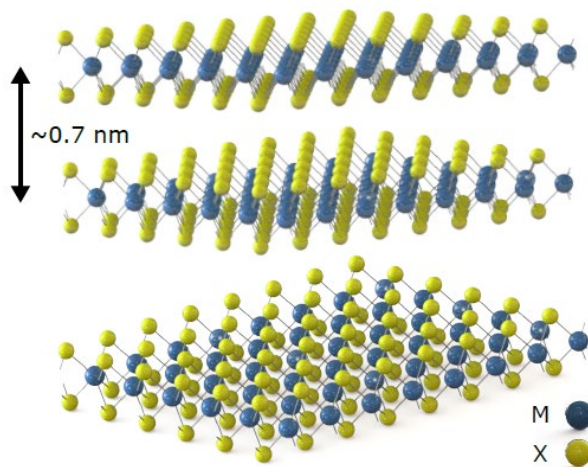
Fig 1.1 Schematic 3D crystal structure of TMDs [36]

1.2 Thesis organisation

This thesis included my Ph.D. research results about exploring the applicability of different TMDs materials used as a saturable absorber for laser pulses generation and studying their NLO response under high-power laser excitation. The study scope is mainly focused on group-10 platinum (Pt), or Palladium (Pd) based TMDs due to the exceptional material properties and will discuss in the following chapter. Meanwhile, the effect of the TMDs-SA fabrication process on the pulsed laser performance will also discuss. The organisation of this thesis is briefly introduced as follows.

Chapter 2 introduces several fundamental concepts of nonlinear optical effects, including the mechanism of saturable absorption and passive laser pulses generation. Additionally, the novelty, characteristic, and preparation methods of the 2D materials will also be discussed in this chapter.

Chapter 3 demonstrates the application of group 6 TMDs, Tungsten disulfide (WS_2) as SA and the Q-switched laser operation in the diode pump solid-state laser system. In the solid-state laser cavity, it is difficult to scale down the beam spot size of the propagating intracavity light by the configuration of optical components, thus the achieved incident fluence is relatively lower as compared to fibre laser cavity. Therefore, high average intracavity power is generally required to trigger the saturable absorption effect of the SA. However it may induce optical damage to the SA, and the production quality of the SA needs to be improved to withstand the high-power intracavity illumination. In this chapter, the design, and

configuration of the Q-switched solid-state laser cavity are demonstrated. Meanwhile, the bottom-up fabrication process of WS$_2$-SA is also discussed.

Chapter 4 mainly discusses the application of group-10 TMDs-SA in Er-doped fibre laser systems. As a newly developing TMDs member, group-10 TMDs have shown distinguished merits, including high air stability in ambient condition, high charge carrier mobility, as well as promising saturable absorption property. In this chapter, the mode-locked Er-doped fibre lasers based on PtS$_2$ and PtTe$_2$-SA are demonstrated and discussed.

Chapter 5 demonstrates the modification of the nonlinear optical absorption (NOA) response of PtS$_2$ nanosheets by modulating the material lateral size as well as the layer thickness. It shows that the NOA properties of Pt-based TMD can shift from reverse saturable absorption to saturable absorption, which can further be utilized in various applications.

Chapter 6 is a summary of this thesis and outlook for future work.

1.3 References

1. M. J. Digonnet, "Rare-earth-doped fiber lasers and amplifiers, revised and expanded," CRC press. (2001).
2. Abramovici, , W. E. Althouse, R. W. Drever, Y. Gürsel, S. Kawamura, F. J. Raab, and R. E. Vogt, "LIGO: The laser interferometer gravitational-wave observatory," science, 256(5055), 325-333(1992).
3. E. J. Reddick, D. O. Olsen, J. F. Daniell, W. B. Saye, B. McKernan, W. Miller, snd M. Hoback, "Laparoscopic laser cholecystectomy," Laser Medicine and Surgery News and Advances, 7(1), 38-40(1989).
4. B. Anderberg, and M. L. Wolbarsht, "Laser weapons: the dawn of a new military age," Springer(2013).
5. Y. R. Shen, "The principles of nonlinear optics," New York, Wiley-Interscience575, (1984).
6. J. M. Ralston, and R. K. Chang, "Optical limiting in semiconductors," Applied Physics Letters, 15(6), 164-166(1969).
7. M. Hercher, "An analysis of saturable absorbers," Applied optics 6(5), 947-954(1967).
8. A. J. DeMaria, , D. A.Stetser, and H. Heynau, "Self mode-locking of lasers with saturable absorbers," Applied Physics Letters, 8(7), 174-176(1966).
9. E. Garmire, and A. Yariv, "Laser mode-locking with saturable absorbers," IEEE Journal of Quantum Electronics, 3(6), 222-226(1967).
10. P. L. Kelley, "Self-focusing of optical beams," Physical Review Letters, 15(26), 1005(1965).
11. M. Hercher, "Laser-induced damage in transparent media," J. Opt. Soc. America, 54, 563(1964)
12. E. P. Franken, A. E. Hill, C. W.Peters, and G. Weinreich, "Generation of optical harmonics," Physical Review Letters, 7(4), 118(1961).
13. N. Bärsch, K. Körber, A. Ostendorf, K.H. Tönshoff, "Ablation and cutting of planar silicon devices using femtosecond laser pulses," Appl, Phys. A, 77(2), 237-242(2003).
14. L. Qi, K. Nishii, M. Yasui, H. Aoki, and Y. Namba, "Femtosecond laser ablation of sapphire on different crystallographic facet planes by single and multiple laser pulses irradiation," Opt. Laser Eng. 48(10),1000-1007(2010).
15. Shen, N. et al., "Ablation of cytoskeletal filaments and mitochondria in live cells using a femtosecond laser nano scissor," Mech. Chem. Biosystems 2, 17–25 (2005).
16. Rafael R. Gattass and Eric Mazur," Femtosecond laser micromachining in transparent materials" Nature photonics 2 , 219-225(2008).
17. P. Kafalas, J. I.Masters, and E. M. E. Murray, "Photosensitive Liquid used as a Nondestructive Passive Q-Switch in a Ruby Laser," Journal of Applied Physics, 35(8), 2349-2350(1964).
18. B. H. Soffer,. "Giant pulse laser operation by a passive, reversibly bleachable absorber," J. Appl. Phy. 35(8), 2551-2551(1964).
19. C. Ma, X. Tian, B. Gao, and G. Wu, "Dynamic evolution of the dissipative soliton in passively mode-locked fiber laser based on black phosphorus as a new saturable absorber," Opt. Commun. 406, 177-182 (2018).
20. Y. Chen, G. Jiang, S. Chen, Z. Guo, X. Yu, C. Zhao, H. Zhang, Q. Bao, S. Wen, D. Tang, and D. Fan, "Mechanically exfoliated black phosphorus as a new saturable absorber for both Q-switching and Mode-locking laser operation," Opt. Express 23(10), 12823-12833 (2015).
21. K. V. Yumashev, I. A. Denisov, N. N. Posnov, N.V. Kuleshov, and R. Moncorge, "Excited state absorption and passive Q-switch performance of Co^{2+}doped oxide crystals," J Alloys and Comp 341, 366–370, (2002).
22. J. Dong, P. Deng, Y. Liu, Y. Zhang, J. Xu, W. Chen, and X. L. Xie, "Passively Q-switched Yb:YAG laser with Cr^{4+}:YAG as the saturable absorber," Appl. Opt. 40(24), 4303-4307 (2001).
23. G. J. Spühler, R. Paschotta, R. Fluck, B. Braun, M. Moser, G. Zhang, E. Gini, and U. Keller, "Experimentally confirmed design guidelines for passively Q-switched microchip lasers using semiconductor saturable absorbers," J Opt Soc Am B 16(3), 376-388, (1999).
24. C. Y. Tang, P. K. Cheng, L. Tao, H. Long, L. H. Zeng, Q. Wen, and Y. H. Tsang, "Passively Q-Switched Nd: YVO4 Laser Using WS_2 Saturable Absorber Fabricated by Radio Frequency Magnetron Sputtering Deposition," J Lightwave Techno 35, 4120-4124, (2017).
25. L. Tao, X. Huang, J. He, Y. Lou, L. Zeng, Y. Li, H. Long, J. Li, L. Zhang, and Y. H. Tsang, "Vertically standing $PtSe_2$ film: a saturable absorber for a passively mode-locked Nd:LuVO4 laser," Photonics Research 6, 750-755(2018).
26. Z. Luo, M. Zhou, J. Weng, G. Huang, H. Xu, C. Ye, and Z. Cai, "Graphene-based passively Q-switched dual-wavelength erbium-doped fiber laser," Opt. Lett. 35(21), 3709-3711 (2010).
27. Z. Sun, T. Hasan, F. Torrisi, D. Popa, G. Privitera, F. Q. Wang, F. Bonaccorso, D. M. Basko, and A. C. Ferrari, "Graphene mode-locked ultrafast laser," ACS Nano 4, 803–810 (2010).
28. Y. G. Wang, H. R. Chen, X. M. Wen, W. F. Hsieh, and J. Tang, "A highly efficient graphene oxide absorber for Q-switched Nd: GdVO4 lasers," Nanotechno. 22(45), 455203 (2011).
29. G. Sobon, J. Sotor, J. Jagiello, R. Kozinski, M. Zdrojek, M. Holdynski, P. Paletko, J. Boguslawski, L. Lipinska, and K. M. Abramski, "Graphene Oxide vs. Reduced Graphene Oxide as saturable absorbers for Er-doped passively mode-locked fiber laser," Opt. Express 20(17), 19463-19473 (2012).
30. H. Yu, L. Zhang, Y. Wang, S. Yan, W. Sun, J. Li, Y. H. Tsang, and X. Lin, "Sub-100 ns solid-state laser Q-switched with double wall carbon nanotubes," Opt. Commun. 306, 128–130 (2013).
31. C. Y. Tang, Y. Chai, H. Long, L. Tao, L. H. Zeng, Y. H. Tsang, and X. Lin, "High-power passively mode-locked Nd: YVO4 laser using SWCNT saturable absorber fabricated by dip coating method," Opt. Express. 23, 4880-4886 (2015).
32. K. F. Mak and J. Shan, "Photonics and optoelectronics of 2D semiconductor transition metal dichalcogenides," Nat. Photon. 10(4), 216 (2016).
33. M. Chhowalla, Z. Liu, and H. Zhang, "Two-dimensional transition metal dichalcogenide (TMD) nanosheets," Chem. Soc. Rev. 44, 2584-2586 (2015).
34. S. Manzeli, D. Ovchinnikov, D. Pasquier, O. V. Yazyev, and A. Kis, "2D transition metal dichalcogenides," Nat. Rev. Mater. 2, 17033 (2017).

35. K. Wu, B. Chen, X. Zhang, S. Zhang, C. Guo, Chao, Li, P. Xiao, J. Wang, L. Zhou, W. Zou, and J.Chen, "High-performance mode-locked and Q-switched fiber lasers based on novel 2D materials of topological insulators, transition metal dichalcogenides and black phosphorus: review and perspective," Opt. Comm. 406, 214-229(2018).

36. R. I. Woodward, and E. J. Kelleher, "2D saturable absorbers for fibre lasers," Appl. Sci. 5(4), 1440-1456(2015)

37. K. Wang, J. Wang, J. Fan, M. Lotya, A. O'Neill, D. Fox, and H. Zhang,. "Ultrafast saturable absorption of two-dimensional MoS2 nanosheets," ACS nano, 7(10), 9260-9267(2013).

38. R.I.Woodward, R.C.T. Howe, T.H. Runcorn, G. Hu, F. Torrisi, E.J.R. Kelleher, T. Hasan, "Wideband saturable absorption in few-layer molybdenum diselenide (MoSe2) for Q-switching Yb-, Er- and Tm-doped fibre lasers," Opt. Exp. 23, 1–11(2015).

39. Z. Luo, Y. Li, M. Zhong, Y. Huang, X.Wan, J. Peng, J. Weng, "Nonlinear optical absorption of few-layer molybdenum diselenide (MoSe2) for passively mode-locked soliton fibre laser [Invited] ," Photonics Res. 3, A79–A86(2015).

40. B. Chen, X. Zhang, K. Wu, H. Wang, J. Wang, and J.Chen, "Q-switched fibre laser based on transition metal dichalcogenides MoS_2, $MoSe_2$, WS_2, and WSe_2," Opt. Exp.23, 26723–26737(2015).

41. H. Long, L. Tao, C. Y. Tang, B. Zhou, Y. Zhao, L. Zeng, S. F. Yu, S. P. Lau, Y. Chai, and Y. H. Tsang, "Tuning nonlinear optical absorption properties of WS_2 nanosheets," Nanoscale 7, 17771-17777 (2015).

42. G. Liang, L. Zeng, Y. H. Tsang, L. Tao, C. Y. Tang, P. K. Cheng, H. Long, X. Liu, J. Li, J. Qu, and Q. Wen, "Technique and model for modifying the saturable absorption (SA) properties of 2D nanofilms by considering interband exciton recombination," J. Mater. Chem. C 6, 7501-7511 (2018).

43. L. Tao, B. Zhou, G. Bai, Y. Wang, S. F. Yu, S. P. Lau, Y. H. Tsang, J. Yao, and D. Xu, "Fabrication of covalently functionalized graphene oxide incorporated solid-state hybrid silica gel glasses and their improved nonlinear optical response," J. Phys. Chem. C 117, 23108-23116 (2013).

CHAPTER 2
Theory

The main theme of this thesis is to investigate the nonlinear optical properties of the novel two-dimension layered material, where the concept and characteristic of 2D materials, will be discussed in this chapter. Meanwhile, the mechanism of passive laser pulses generation will be illustrated as follows.

2.1 Two-dimensional layered materials

2.1.1 Brief introduction of 2D materials

The research work of material with a two-dimensional (2D) layered structure can be traced back to 1950s [1-2]. However, restricted by the synthesis process, as well as the characterisation method, the material properties which contributed by the 2D structure had not been comprehensively explored at that time. In the year 2004, Andre Deim et al. demonstrated the preparation of two-dimensional mono-element material, graphene, by utilising the scotch-tape method, in which inspired and attracted vast attention toward the study on 2D layered material.

For applying the 2D materials in photonic aspect, it induced a great impact within the field due to its exceptional properties as compared to the conventional bulk photonic material, for instance, silicon (Si) and gallium arsenide (GaAs) [3]. By delamination and reduction of the dimensionality of the 2D materials, the

quantum confinement effect in the direction perpendicular to the 2D plane becomes significant and thus brings distinctive electronic and optical properties to the layered 2D materials [4-7]. One of the examples is that the electron mobility of graphene is around 100 times greater than that of Si [8]. Meanwhile, different from the traditional bulk crystal, where the synthesis of heterostructures need to consider the epitaxy and lattice matching issue, it is favourable for utilising different 2D materials to construct vertical heterostructures as the layers with the different lattice constants are merely bonded by weak van der Waals force (similar to that in their bulk form). Hence, novel applications can be achieved by using heterostructure with a distinct combination of 2D material, for stance, a p-n heterojunction for light emission usage, as shown in Fig. 2.1 [9].
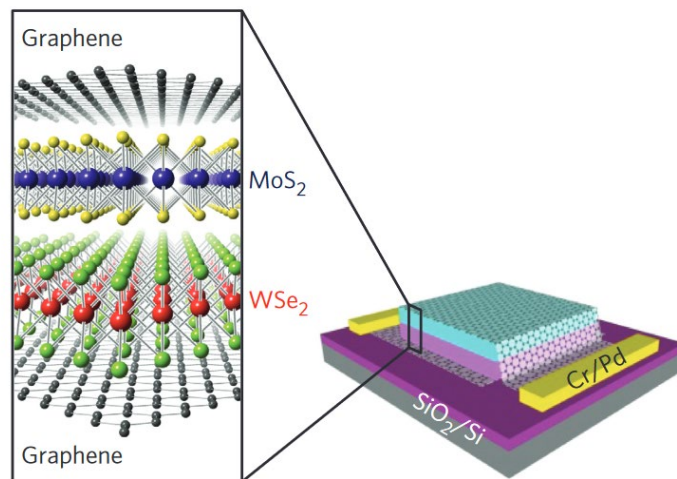
Fig. 2.1 Schematic diagram of a p-n TMDs heterojunction [9].

Furthermore, the surfaces of 2D material are generally passivated, which means there are no dangling bonds attached on the 2D materials surface, and thus allow the 2D materials be readily integrated with the different photonic structures, such as waveguide [10-11] and cavity [12-13] to form practical devices, including ultrafast laser. Remarkably, the diverse and extensive bandgap structure allows the

operation wavelength range of 2D materials to be widely extended, as shown in Fig. 2.2, and which provided excellent design flexibility and applicability for the application of 2D materials as photonic devices.
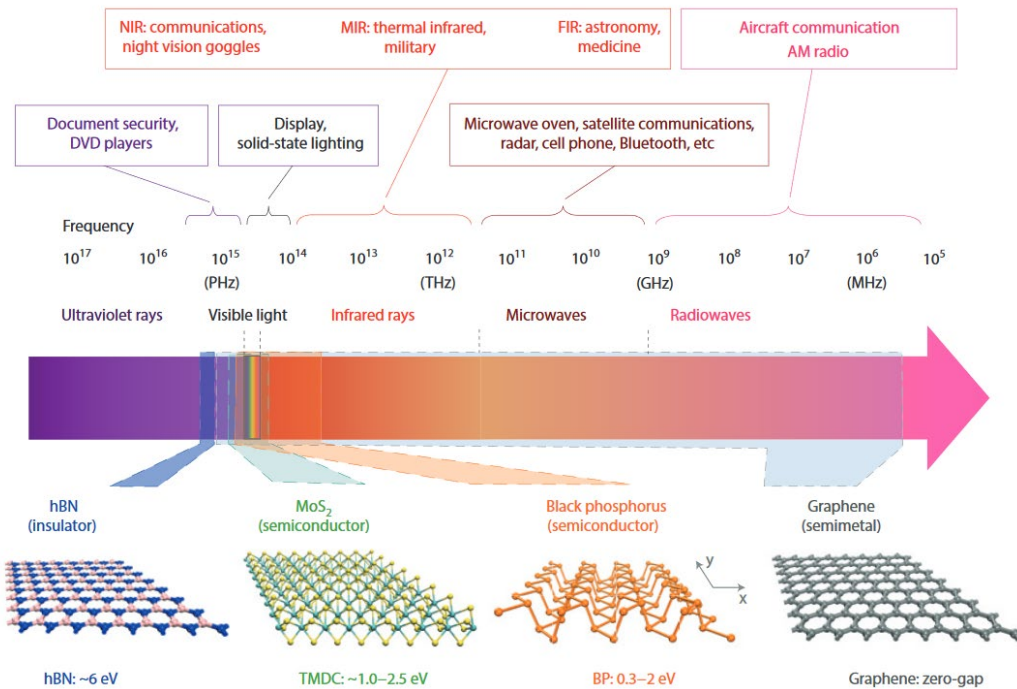
Fig. 2.2 Schematic diagram for showing the operational wavelength coverage of 2D materials, where NIR, MIR and FIR represent near-, mid-, and far-infrared, respectively. The natural or tunable bandgap energy ranges are shown at the bottom of the figure. [3]

Dedicated by the effort of numerous research groups, vast numbers of 2D materials and the corresponding material properties have been explored, as shown in Fig. 2.3 [14]. Nevertheless, the work and exploration of 2D material are still actively continuing, in which new 2D candidates kept be discovered currently, for instance, MXene and air-stable group 10 Pt/ Pd based TMDs.

Graphene family	Graphene	hBN 'white graphene'		BCN	Fluorographene	Graphene oxide
2D chalcogenldes	MoS_2, WS_2, $MoSe_2$, WSe_2		Semiconducting dichalcogenides: $MoTe_2$, WTe_2, ZrS_2, $ZrSe_2$ and so on	Metallic dichalcogenides: $NbSe_2$, NbS_2, TaS_2, TiS_2, $NiSe_2$ and so on		
				Layered semiconductors: GaSe, GaTe, InSe, Bi_2Se_3 and so on		
2D oxides	Micas, BSCCO	MoO_3, WO_3	Perovskite-type: $LaNb_2O_7$, $(Ca,Sr)_2Nb_3O_{10}$, $Bi_4Ti_3O_{12}$, $Ca_2Ta_2TiO_{10}$ and so on		Hydroxides: $Ni(OH)_2$, $Eu(OH)_2$ and so on	
	Layered Cu oxides	TiO_2, MnO_2, V_2O_5, TaO_3, RuO_2 and so on			Others	

Fig. 2.3 A brief introduction list of current 2D materials [14].

2.1.2 Preparation of 2D materials

There are two general approaches for preparing 2D layered materials, which are top-down and bottom-up methods. Literally, the bottom-up synthesis method involves a fabrication process that originated from a bare ground substrate and which the element atoms accumulated and bonded to grow crystalline structure on the substrate. The bottom-up method typically includes of CVD growth [15] and two-step annealing/sulfurization [16]. As shown in Fig. 2.4, it shows the general procedures of the two-step annealing/ sulfurization method. This fabrication method generally starts with the deposition of a precursor thin film, in which the deposition can be accomplished by using magnetron sputtering deposition, thermal evaporation and pulsed-laser deposition, etc. The precursor thin film may compose of the pure transition metal, oxide of the transition metal, or even TMD in the amorphous phase. Afterwards, the precursor thin film will be annealed or sulfurised under specific temperature profile and time. The advantage of the bottom-up growth method is that it can produce 2D materials with large surface area scale and high crystallinity. However, this method usually involves costly and

lengthy procedures. The two-step annealing/ sulfurization synthesis method was utilised to fabricate WS_2 saturable absorber for applying in the pulsed laser system and will be discussed in chapter 3.
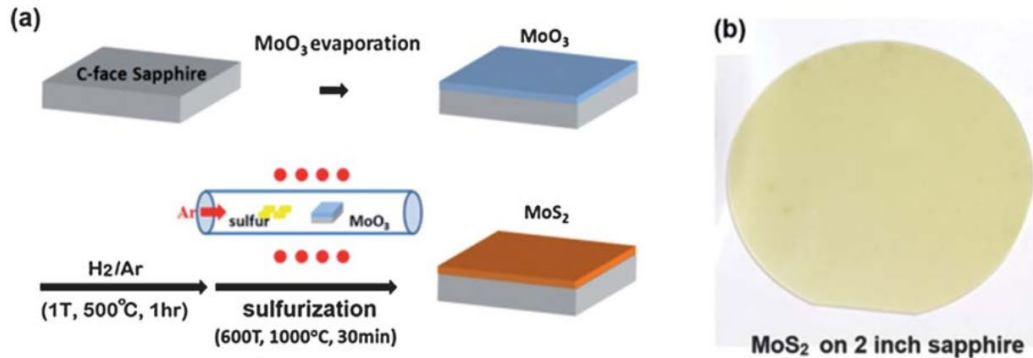
Fig. 2.4 A Schematic diagram of the synthesis of a few layers MoS_2 film by utilising a two-step annealing/ sulfurization. [16]

The second type of 2D material synthesis method is the top-down approach, in which the few layers 2D material is fabricated by the delamination of the bulk crystal. The bulk crystal can be prepared by CVD growth or hydrothermal reaction [17]. And the delamination is typically achieved by using liquid-phase ultrasonic exfoliation, as shown in Fig. 2.5 [18]. The bulk crystal, usually in powder form, is firstly mixed with a selected solvent. Different solvents have been utilised for the effective exfoliation of 2D materials in previous literature, including N- methyl-2-pyrrolidone (NMP), N-vinyl-2-pyrrolidone (NVP), isopropanol (IPA), dimethyl sulfoxide (DMSO), dimethylformamide (DMF), etc. [19]. And the selection of the solvents depends on the surface energies of the solvent and 2D materials. Afterwards, the ultrasonic wave in the solvent will generate cavitation microbubbles. As these microbubbles collapse, it will produce a high-energy shock wave to break the interlayer bonding and thus generate exfoliated 2D materials [18]. Besides, fragmentation of the 2D material flakes can also be achieved nearby

the microbubbles collapse, in which 2D materials quantum-dot may be generated by applying appropriate sonication power and solvent [20]. The liquid-phase ultrasonic exfoliation is a simple, time and cost-saving delamination method for synthesising few layers 2D materials. However, the distribution range of the exfoliated nanosheet lateral dimension and layer thickness is generally broad, and a post-centrifugation method is usually applied to filter out the required nanosheet distribution set. In this work, group 10 TMDs, PtS_2 and $PtTe_2$ were exfoliated by applying liquid-phase ultrasonic exfoliation. The exfoliated 2D TMDs nanosheets were further applied as a saturable absorber, and the corresponding performance is discussed in Chapter 4.
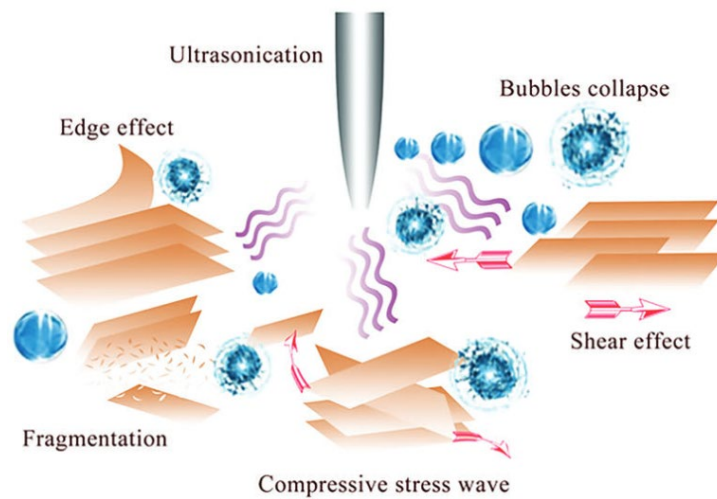
Fig. 2.5 Schematic diagram showing the liquid-phase ultrasonic exfoliation process of layered 2D material [18].

2.2 Nonlinear optics

2.2.1 Introduction

As electromagnetic radiation with an electrical field amplitude E irradiates on a certain medium, the electric charge of molecules or atoms within the medium will be displaced relatively under the action of the radiation's E-field. Remarkably, this displacement of electrical charges will induce a secondary E-field inside the medium and is described as electric polarization P. If the intensity of the incident radiation is weak, the induced polarization P is depending linearly on the E-field strength of the incident radiation,

$$P = \varepsilon_0 \chi^{(1)} E, \qquad\qquad \text{Eq 2.1}$$

where $\chi^{(1)}$ is a complex number tensor and is defined as the linear susceptibility. ε_0 is the dielectric coefficient in the vacuum. Actually, the magnetic field of the incident electromagnetic radiation will also affect the magnetic polarization of the interacting medium. Nevertheless, for most of the common materials, this magnetic field induced effect is very weak and thus can be neglected.

By the invention and practical application of laser. It provided a light source with the intensity much greater than that of common light in several orders of magnitude, in which induced a distinctive nonlinear optical response within the interacting medium. In this condition, the expression of the induced polarization P is modified by expanding P into a power series of E-field strength E,

$$P(\text{t}) = \varepsilon_0 \chi^{(1)} E + \varepsilon_0 \chi^{(2)} E^2 + \varepsilon_0 \chi^{(3)} E^3 + \cdots, \qquad \text{Eq 2.2}$$

$$P(\text{t}) = P^{(1)} + P^{(2)} + P^{(3)} + \cdots, \qquad\qquad \text{Eq 2.3}$$

$\chi^{(2)}$ and $\chi^{(3)}$ are known as the second- and third-order nonlinear optical susceptibilities, respectively. The total induced polarization can be expressed as

the sum of the linear polarization $P^{(1)}$, second-order nonlinear polarization $P^{(2)}$, third-order nonlinear polarization $P^{(3)}$ and the higher-order nonlinear polarization. By expressing the polarization P(t) in terms of applied E-field, it can describe different nonlinear optical phenomena since a time-varying polarization is a source of new components of the electromagnetic field.

Generally, it can apply the linear, second- and third-nonlinear optical susceptibilities to imply most of the nonlinear optical effect, for instance, second harmonic generation and nonlinear absorption. In this work, the nonlinear absorption response of novel 2D TMDs material is mainly studied. Saturable absorption is one of the most prominent and practical nonlinear optical effect, which can be applied to induce ultrashort laser pulses. The theory of nonlinear saturable absorption will be discussed in the following section.

2.2.2 Saturable absorption

Saturable absorber generally is a nonlinear optical device in which the corresponding absorbance is highly depending on the intensity of the incident light. The absorbance of the absorber will be reduced under high-intensity illumination which caused by the saturation of the light absorption within the nonlinear materials. The mechanism can be simply expressed in Fig. 2.6, at low-intensity illumination, the valence electrons are excited to the conduction band by photon absorption, and the electron density of state (eDOS) in the conduction band is not be fully occupied. As a result, it induces a base level of the optical absorbance, which is also known as linear absorbance. However, as the incident light intensity

scaled up, the eDOS in conduction band will be readily filled up and blocking

further photon absorption. Hence, the absorbance of the nonlinear material is

relatively reduced and is know as saturable absorption.
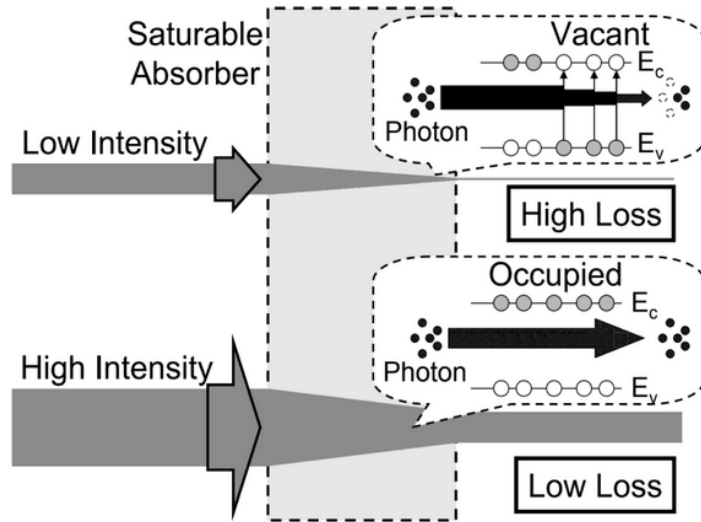
Fig. 2.6 Schematic diagram showing the mechanism of saturable absorber absorption, where E_v and E_c represent the energy levels of the valence band and conduction band, respectively. [21]
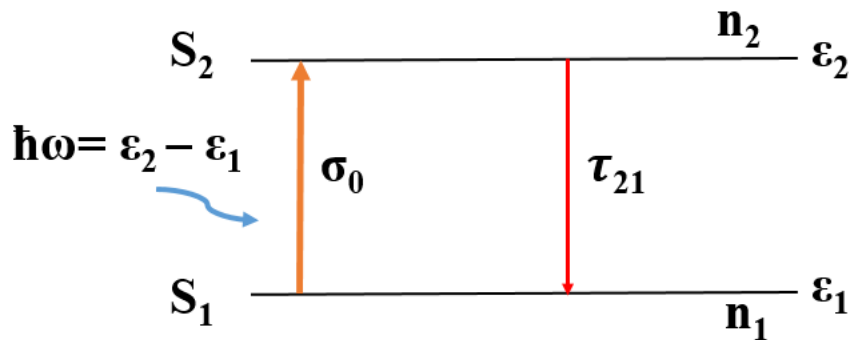
Fig. 2.7 Light-induced saturable absorption in a two-level molecular model

Based on the simple two-level molecular model shown in Fig. 2.6, the nonlinear

absorption coefficient of a saturable absorber is deduced as follow. For the two-

level model, it consists of the ground-state S_1 and first excited-state S_2. As shown

in Fig. 2.7, the S_1 and S_2 state possess with energy ε_1 and ε_2, the electron density

of state n_1 and n_2, respectively. In the photoexcitation, as photons with energy equal

to the energy difference of two states (ε_2 - ε_1) interact with the absorber, the

electrons on ground-state will be excited to S_2 as a stimulated transition with an absorption cross-section σ_0. Meanwhile, the excited electrons may return to the ground-state by either stimulated emission or spontaneous emission. Typically, the spontaneous emission takes the dominant effect where most of the excited electrons return to the ground-state through spontaneous radiation with a relaxation time τ_{21} and transition probability of $1/\tau_{21}$. Also part of the excited electrons will return to ground-state through stimulated emission with the same transition probability of σ_0. Consider the change of n_2 with time, it can be expressed by the following rate equation,

$$\frac{\partial n_2}{\partial t} = \frac{\sigma_0}{\hbar\omega}I(n_1 - n_2) - \frac{n_2}{\tau_{21}} \qquad \text{(Eq 2.4)}$$

Which is equivalent to the pumping rate minus the decay rate. Meanwhile, the total and difference of the electron density of the two states are,

$$N = n_1 + n_2 \qquad \text{(Eq 2.5)}$$

$$\Delta n(t, I) = n_1(t, I) - n_2(t, I) \qquad \text{(Eq 2.6)}$$

and

$$\frac{\partial n_2}{\partial t} = -\frac{\partial n_1}{\partial t} \qquad \text{(Eq 2.7)}$$

Combining the above equations, the change of Δn with time is expressed as follow,

$$\frac{\partial \Delta n(t,I)}{\partial t} = -\frac{2\sigma_0 I \Delta n}{\hbar\omega} - \frac{\Delta n - N}{\tau_{21}} \qquad \text{(Eq 2.8)}$$

If the pulse-width of the incident light is relatively much greater than that of τ_{21}, the steady-state condition is fulfilled where the change of Δn with time is equal to 0 in Eq 2.8, where

$$\Delta n(I) = \frac{\hbar\omega N}{2\sigma_0 I \tau_{21} + \hbar\omega} \qquad \text{(Eq 2.9)}$$

Consider the nonlinear absorption coefficient $\alpha(I)$ of the absorber, it is the product of $\Delta n(I)$ and the absorption cross-section of the stimulated transition σ_0,

$$\alpha(I) = \Delta n(I)\sigma_0 \qquad \text{(Eq 2.10)}$$

When the light intensity tends to be 0, the linear absorption coefficient α_0 is,

$$\alpha_0 = N\sigma_0 \qquad \text{(Eq 2.11)}$$

By defining the saturation intensity I_s as a phenomenological parameter, in which the nonlinear absorption coefficient $\alpha(I)$ reduced to the half of its initial value at the low incident light intensity (i.e. $\alpha(I_s) = \alpha_0 / 2$) and equal to,

$$I_s = \frac{\hbar\omega}{2\sigma_0\tau_{21}} \qquad \text{(Eq 2.12)}$$

Conclusively, by substituting Eq 2.10, Eq 2.11 and Eq 2.12 to Eq 2.9, the nonlinear absorption coefficient $\alpha(I)$ can be expressed as

$$\alpha(I) = \frac{\alpha_0}{1 + \frac{I}{I_s}} \qquad \text{(Eq 2.13)}$$
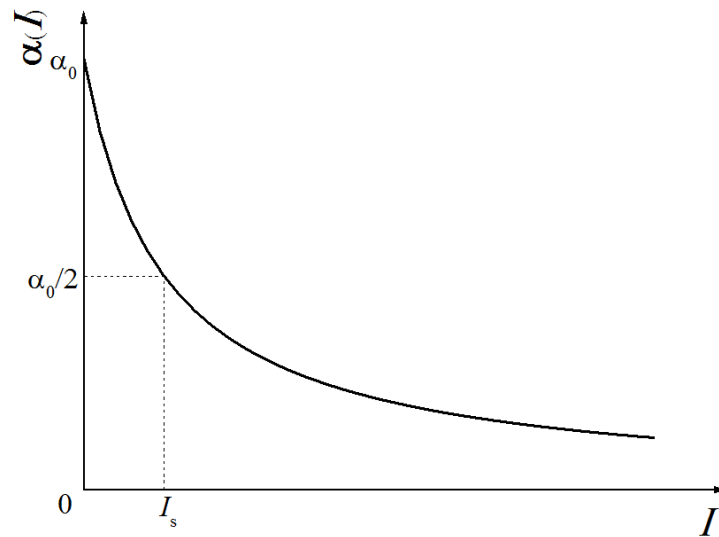
Fig. 2.8 Schematic diagram showing the simple hyperbolic model of the nonlinear absorption coefficient of a two-level system with respect to the incident light intensity.

From the above equations, it shows that when the intensity of the incident light is extremely large, then the difference of the electron density of the two states $\Delta n(I)$ tends to be 0. In this balance condition, incident photons cannot be further absorbed by the absorber and just pass through the medium, which is the essence of the saturable absorption of the simple two-level molecular model.

2.2.3 Passive mode-locking

For the application of short or ultrashort laser pulses generation, it can be achieved by applying passive Q-switching and mode-locking mechanism, respectively. In passive mode-locking, the ultrashort laser pulses generation is based on the interaction between the intracavity resonator modes and the nonlinear saturable absorber. In a simple two-mirror laser cavity, by the boundary condition, there is discrete sets of waves with different frequencies propagating in the intracavity, which is known as resonator modes. For the wavelength λ of the resonator modes,

it can be calculated by the equation of 2L/n, where L is the length of the laser cavity and n is an integer defined the order of the modes. Generally, the cavity length is much longer than that of the wavelength of the modes, and thus the number of modes within the cavity can be extended to the value of 10^5 to 10^6. Besides, the frequency separation Δv between two successive resonator modes is estimated as c/2L, where c is the speed of light. Meanwhile, the propagating modes within the cavity are governed by the gain bandwidth of the active gain media as shown in Fig. 2.7. The allowed resonator modes are enclosed within the gain bandwidth envelope. For a Ti: sapphire laser with 128 nm bandwidth and 3 meters cavity length, it is able to support around 256,000 modes in the cavity.
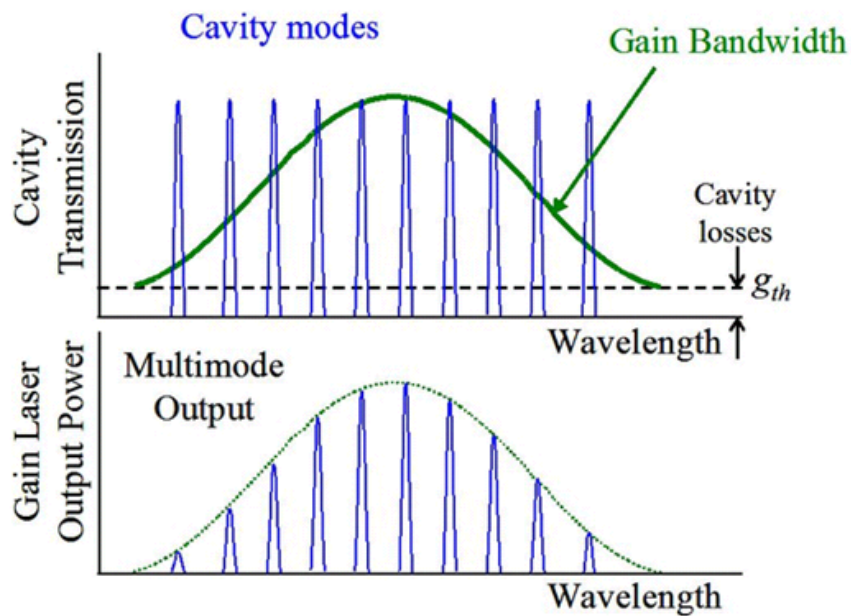
Fig. 2.9 Schematic diagram shows the cavity resonator modes distribution and gain bandwidth envelope [22].

Each of the individual resonator modes has no fixed phase relationship between each other. The superimposition of the modes can produce intensity fluctuation within the cavity, in which a temporal pulse will be induced at a certain point of time, as shown in Fig. 2.8. The higher the number of involved resonator modes,

the greater is the peak intensity of the temporal pulse. As the phases relationships between each mode are not fixed, if there is no preserving process, the temporal pulse will be vanished and restored to a continuous wave (CW) pattern in a short time due to chromatic dispersion, as shown in Fig. 2.9.
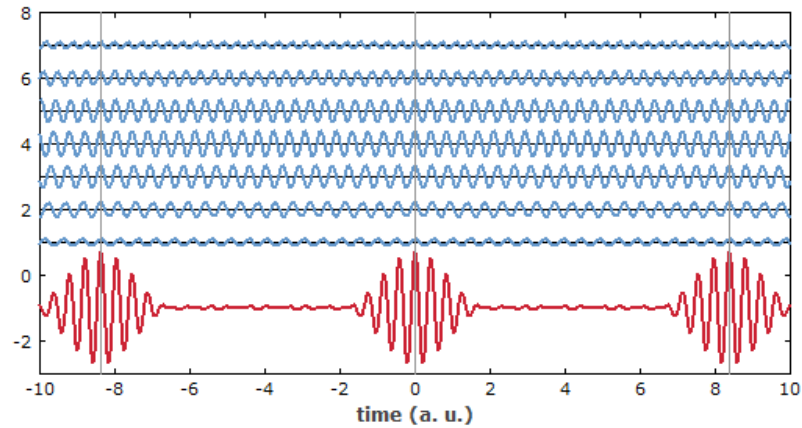
Fig. 2.10 The simulation of superimposition result (red curve) of several oscillations modes with a different frequency (blue curves) within a resonator cavity. [23]
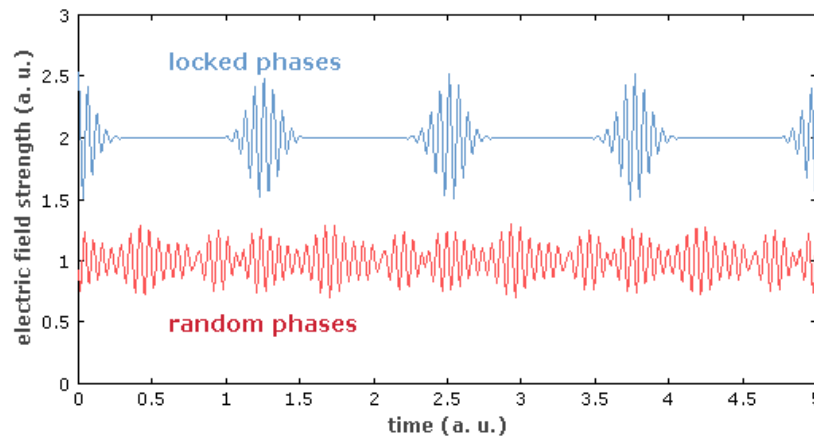
Fig. 2.11 The temporal evolution of the intracavity field within a laser system, the blue curve represents a phase-locked pattern, while the red curve represents a phase-unlocked pattern [23].

In the mode-locking process, a modulator is applied to control the intracavity loss, which can periodically provide a pulse-shaping effect to the superimposed pulse and thus shorten the corresponding pulse duration value, as shown in Fig. 2.10 [24]. The modulation of intracavity loss can be accomplished by using acoustic-optic modulator (AOM) [25] or electro-optic modulator (EOM) [26], as well as the saturable absorber. By utilising an electronic driver modulus and the

AOM/EOM, the intracavity loss is actively modulated, in which net gain is selectively provided to the centre region of the transmitted temporal pulse and the wing parts are suppressed. This pulses generation mechanism is known as active mode-locking. Typically the AOM/EOM system is bulk and expensive. Meanwhile, restricted by the reaction time of the electronic driver and modulator, the loss modulation speed is relatively slow in the actively mode-locked laser and thus limited the further pulse shortening effect [24]. These limitations have motivated the exploration of a substitutional modulator, which is the saturable absorber. As the temporal pulse incident on the absorber, the leading and trailing parts (low-intensity light) of the pulse are absorbed preferentially due to unsaturation condition of the absorber. Once the intensity of the passing pulse reached the saturable intensity limit, the absorbance of the absorber will be reduced and thus provided a net gain to the most centre part of the temporal pulse. Generally, a mode-locked pulse with relatively shorter pulse duration can be achieved by applying passive mode-locking because of the fast recovery time of saturable absorber. Remarkably, the passive mode-locked laser, for instance, mode-locked EDFL and YDFL are compact in size and cost-effective, thus applied extensively in the modern laser processing industry.
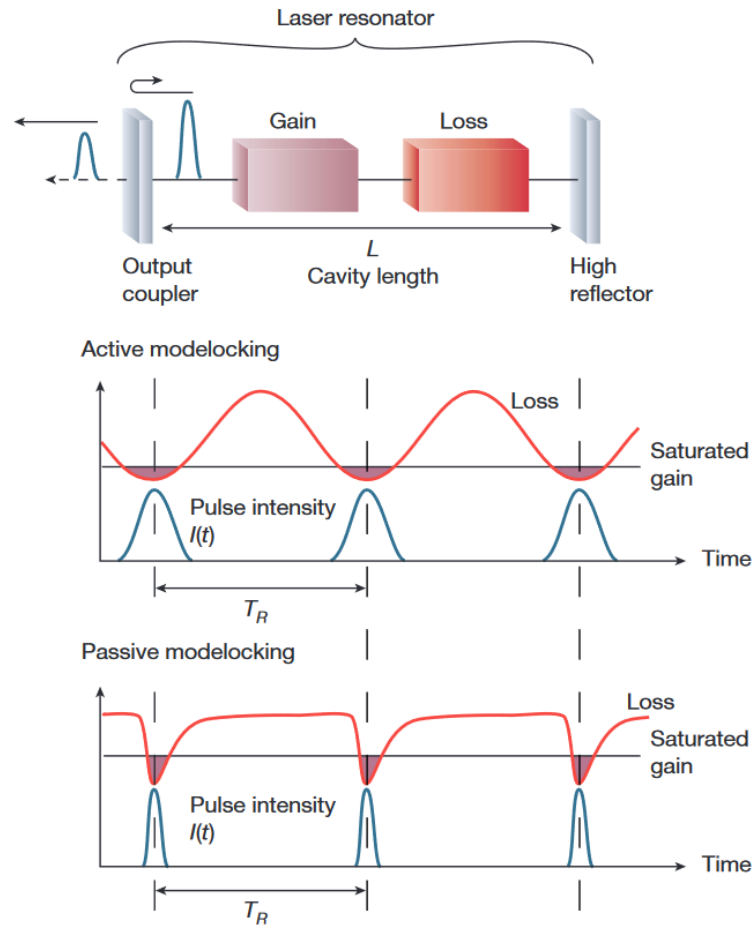
Fig. 2.12 (Top) The schematic diagram of a compact two-mirror mode-locking laser. The laser pulse-shaping loss dynamics for (middle) active and (bottom) passive mode-locking [24].

2.2.4 Passive Q-switching

Not limited to mode-locked laser, the saturable absorber can also be applied to induce passive Q-switching for generating microsecond to nanosecond laser pulses. In Q-switched laser, the intracavity losses are modulated from an initial high-value to low-value, which is corresponding to from low-quality factor (low Q) to high-quality factor (high Q). The suddenly shift to a high Q condition may induce a significantly high net gain in the cavity and thus generate a steeply rising intense pulse [27]. As shown in Fig. 2.11, the population of upper laser level is started to

increase as the pump light introduced into the cavity. Once the population level scaled beyond the threshold value of the low-Q (N_{th}^{LQ}) condition, the lasing action begins. If the intensity of generated radiation reaches the saturable intensity of the absorber, the absorbance of the absorber and total cavity losses will be reduced. Once the population of upper laser level drop to the threshold of high-Q (N_{th}^{HQ}) condition, maximum amplification efficiency achieved, accompanying with the formation of intense Q-switched pulse. This intense pulse will deplete the population of upper laser level and thus terminate the lasing action.
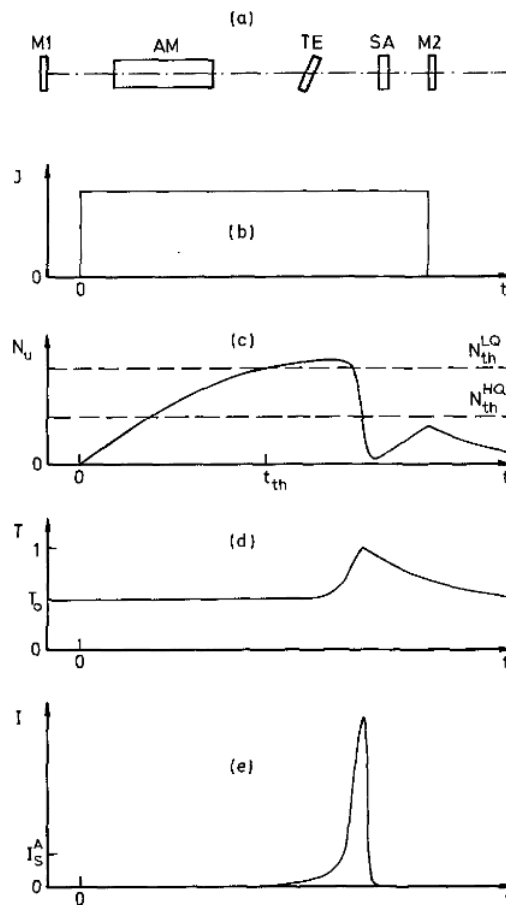
Fig. 2.13 (a) Schematic diagram of a two-mirror Q-switched laser setup, where M1 and M2 are laser mirror, AM respresent the active medium, TE represent the tunning element, and SA represent the saturable absorber. (b) The temporal profile of excitation pulse J (W/cm^3). (c) The upper laser level population N_u (solid curve). And the dashed curves represent the low-Q (N_{th}^{LQ}) and high-Q (N_{th}^{HQ}) laser threshold population, where the t_{th} represent the begin of the laser action. (d) Temporal transmission through the saturable absorber, where T_0 stands for the linear transmission. (e) Temporl pulse development, where I_S^A stands for the saturable intensity of the absorber [27].

2.3 Chapter summary

In this chapter, it had briefly introduced the concept and history of the development of the 2D materials for nonlinear optical applications. Meanwhile, the two general preparation approaches, top-down and bottom-up method, of the 2D materials are illustrated. The common 2D material synthesis methods of liquid-phase ultrasonic exfoliation and two-step annealing/ sulfurization are introduced. Finally, the mechanism of saturable absorption, as well as the passive mode-locking and Q-switching, are also explained.

2.4 Reference

1. K. ARNE, and F. GRQNVOLD, "High Temperature X-Ray Study of the Thermal Expansion of PtS_2, $PtSe_2$, $PtTe_2$, and $PdTe_2$," Acta Chemica Scandinavica 13.9, 1767-1774(1959).
2. V. R. Johnson, and G. W. Vaughn, "Investigation of the mechanism of MoS_2 lubrication in vacuum" Journal of Applied Physics, 27(10), 1173-1179(1956).
3. F. Xia, H. Wang, D. Xiao, M. Dubey, and A. Ramasubramaniam, "Two-dimensional material nanophotonics," Nature Photonics 8(12), 899(2014).
4. K. S. Novoselov et al., "Two-dimensional gas of massless Dirac fermions in graphene," Nature 438, 197–200 (2005).
5. Y. Zhang, Y. W. Tan, H. L. Stormer, and P. Kim, "Experimental observation of the quantum Hall effect and Berry's phase in graphene," Nature 438, 201–204(2005).
6. K. F. Maket al., "Atomically thin MoS_2: A new direct-gap semiconductor," Phys. Rev. Lett. 105, 136805 (2010).
7. A. Splendiani et al, "Emerging photoluminescence in monolayer MoS_2," Nano Lett.10, 1271–1275 (2010).
8. K. S. Novoselov, V. I. Fal'ko, L. Colombo, P. R. Gellert, M. G. Schwab, and K. Kim, "A roadmap for graphene," Nature 490, 192(2012).
9. C. H. Lee, G. H. Lee, A. M. Van Der Zande, W. Chen, Y. Li, M. Han, and J. Guo, "Atomically thin p–n junctions with van der Waals heterointerfaces," Nature nanotechnology 9(9), 676(2014).
10. M. Liu et al., "A graphene-based broadband optical modulator," Nature 474, 64–67 (2011).
11. X. Gan et al., "Chip-integrated ultrafast graphene photodetector with high responsivity," Nature Photon.7, 883–887 (2013).
12. X. Gan et al., "Strong enhancement of light-matter interaction in graphene coupled to a photonic crystal nanocavity," Nano Lett.12, 5626–5631 (2012).
13. A. Majumdar, J. Kim, J. Vuckovic, and F. Wang, "Electrical control of silicon photonic crystal cavity by graphene," Nano Lett.13, 515–518 (2013).
14. A. K. Geim, and I. V. Grigorieva, "Van der Waals heterostructures," Nature 499(7459), 419-425(2013).
15. C. Cong, J. Shang, X. Wu, B. Cao, N. Peimyoo, C. Qiu, S. Litao, and T. Yu, "Synthesis and optical properties of large-area single-crystalline 2D semiconductor WS_2 monolayer from chemical vapor deposition," Adv. Opt. Mater. 2, 131, (2014).
16. L. Y. Chuan, Z. Wenjing, J. K. Huang, L. K. Ku, Y. H. Lee, C. Te Liang, C. W. Chu, and L. L. Jong, "Wafer scale MoS_2 thin layers prepared by MoO_3 sulfurization," Nanoscale 4, 6637, (2012).
17. Y. Peng, Z. Meng, C. Zhong, J. Lu, W. Yu, Y. Jia, and Y. Qian, "Hydrothermal synthesis and characterization of single-molecular-layer MoS_2 and $MoSe_2$," Chemistry Letters 30(8), 772-773(2001).
18. H. Tao, Y. Zhang, Y. Gao, Z. Sun, C. Yan, and J. Texter, "Scalable exfoliation and dispersion of two-dimensional materials–an update," Physical Chemistry Chemical Physics, 19(2), 921-960(2017).
19. Y. Nonoguchi, K. Hata, and T. Kawai, "Dispersion of Synthetic MoS_2 Flakes and Their Spontaneous Adsorption on Single-Walled Carbon Nanotubes," ChemPlusChem, 80(7), 1158-1163(2015).
20. H. Long, L. Tao, C. P. Chiu, C. Y. Tang, K. H. Fung, Y. Chai, Y. H. Tsang, "The WS_2 quantum dot: preparation, characterization and its optical limiting effect in polymethylmethacrylate," Nanotechno. 27, 414005(2016).
21. Ken Kashiwagi and Shinji Yamashita, "Optical Deposition of Carbon Nanotubes for Fiber-based Device Fabrication," DOI: 10.5772/39546
22. Rosa Ana Perez-Herrera and Manuel Lopez-Amo, "Current Developments in Optical Fiber Technology," chapter 17, (2013). (ISBN 978-953-51-1148-1)
23. Mode Locking , RP Photonics Consulting GmbH, https://www.rp-photonics.com/mode_locking.html
24. U. Keller, "Recent developments in compact ultrafast lasers," Nature 424(6950), 831(2003).
25. J. K. Jabczyński, W. Zendzian, and J.Kwiatkowski, "Q-switched mode-locking with acousto-optic modulator in a diode pumped Nd: YVO_4 laser," Opt. exp., 14(6), 2184-2190(2006).
26. K. Iwakuni, H. Inaba, Y. Nakajima, T. Kobayashi, K. Hosaka, A. Onae, and F. L. Hong, "Narrow linewidth comb realized with a mode-locked fiber laser using an intra-cavity waveguide electro-optic modulator for high-speed control," Optics Express, 20(13), 13769-13776(2012).
27. A. Penzkofer, "Passive Q-switching and mode-locking for the generation of nanosecond to femtosecond pulses," Applied Physics B 46(1), 43-60(1988).

CHAPTER 3

Passively Q-switched Nd: YVO$_4$ DPSS laser based on Tungsten disulfide saturable absorber

Diode-pumped solid-state (DPSS) pulsed laser is one of the most applicable laser systems nowadays. The ultrahigh single pulse energy of the Q-switched DPSS laser has granted the system with the extensive capability of industrial material processing, and thus the development of the DPSS pulsed system and the implementation of the saturable absorber (SA) are a continued hot topic. In this chapter, the saturable absorption property of WS$_2$-SA, which fabricated by radio frequency (RF) magnetron sputtering deposition, is experimentally explored. Stable Q-switched DPSS laser operation is demonstrated by utilising a few-layer WS$_2$-SA within the diode-pumped Nd:YVO$_4$ laser cavity. The maximum average output power achieved is 19.6 mW. The corresponding repetition rate, pulse duration and single pulse energy are 135 kHz, 2.3 μs, and 145 nJ, respectively. This result has shown the promising Q-switching performance and nonlinear saturable absorption property of the fabricated WS$_2$-SA, as well as the applicability in the high power DPSS laser system.

3.1 Background and motivation

DPSS pulsed laser is widely applied in the modern industry nowadays due to the merits of compactness, high efficiency, possess high average output power, and the potential of TEM_{00} beam quality [1-5]. In our previous works, commercial SESAM was utilised to induce passive mode-locking and passive Q-switching operation in Nd:YVO_4 DPSS laser system. The SESAM (Model: SAM-1064-2-10ps, operation wavelength: 1064nm, low-intensity absorbance of 2%, and modulation depth of 1.2 %) was purchased from Batop GmbH. As a commercial saturable absorber, the SESAM-based pulsed operation has shown superior spectral and power stability, which can be illustrated by the regular continuous-wave (CW) mode-locking envelope of the output mode-locked signal as shown in Fig. 3.1. However, the operation wavelength of the SESAM is highly-restricted by the semiconductor material properties. Meanwhile, due to the complicated fabrication process, the cost of the SESAM is relatively high as well (~ 62 USD per 1 mm^2). The limitations of SESAM reflected the importance of further exploration of the substitutional nonlinear materials for pulsed laser development. Tungsten disulfide (WS_2) is one of the most prominent SA candidates within the 2D layered TMDs family due to its exceptional saturable absorption property. As similar to Molybdenum disulfide (MoS_2), both of the MoS_2 and WS_2 monolayers have two atomic structure phase, 1T, and 2H [6]. As shown in Fig. 3.2, in the 1T phase, the transition metals are orientated with octahedral coordination. And the 2H MoS_2 / WS_2 possesses prismatic coordination for the transition metal atoms. Different from the semiconductor properties of the 2H structure, the 1T structure

44

demonstrates metallic behaviour [6-7]. Generally, the 1T structure is formed by processing chemical exfoliation on bulky TMDs, such as lithium intercalation accompanying with hydrothermal delamination [8]. And a further annealing process (~ 300℃) can restore the exfoliated 1T phase TMDs to the 2H structure. Typical vapour growth and mechanical exfoliation will result in a 2H structure. In this chapter, based on the RF magnetron sputtering deposition method, the fabricated WS_2 possesses with a 2H structure.
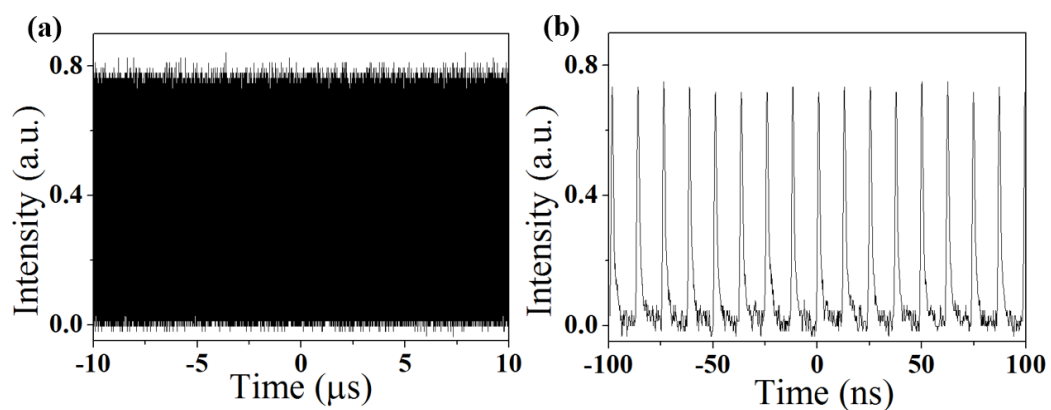
Fig. 3.1 The observation of pulse train output from SESAM-based Nd:YVO$_4$ DPSS mode-locked laser in (a) microsecond time interval and (b) nanosecond time interval
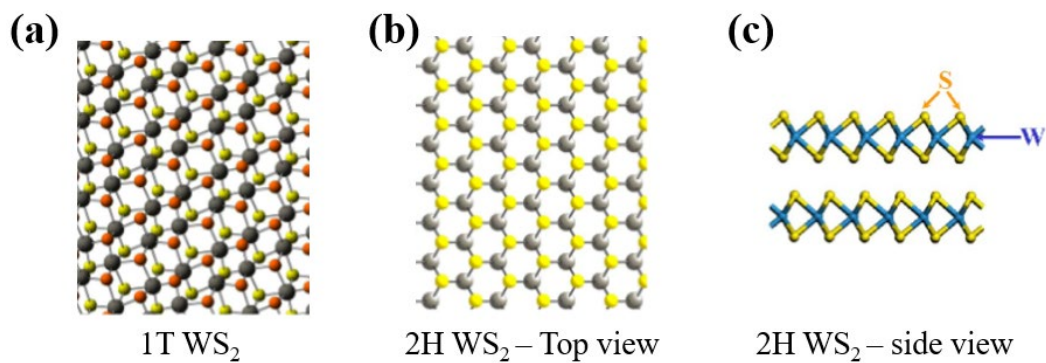
Fig. 3.2 (a) Atomic structure of 1T-WS$_2$ monolayer, where the W atoms are present in grey colour and S atoms are in orange and yellow for top and bottom layers, respectively (Top view). (b) Top view (W and S atoms are in grey and yellow colour, respectively) and (c) side view of the atomic structure of 2H-WS$_2$ monolayer. [6, 9]

2H WS$_2$ possesses the hexagonal space group of P6$_3$/mmc [9], where the lattice constant a and c equal to 3.1532 Å and 12.323 Å, respectively [10]. As shown in

45

Fig. 3.2 (c), a tungsten atoms layer is hexagonally packed between two trigonal sulfide atoms layers to form the monolayer of WS_2. For the electronic band structure of the 2H WS_2, the quantum confinement effect will become dominant as the number of layers decreases [11-13], which leads to a variation of the electronic bandgap structure from indirect bandgap energy of 1.3 eV to direct bandgap of 2.05 eV [9, 14]. Followed the first demonstration of the saturable absorption property of the TMDs (MoS_2) in 2013 [15], the works had extended to WS_2 in 2014 where Fu et al. reported the strong ultrafast saturable absorption response of WS_2 nanoplates under the excitation of a 532 nm picosecond laser light [16]. Afterward, the number of studies and applications of WS_2 as a saturable absorber for inducing passive mode-locking and passive Q-switching was dramatically growing [17-23]. Noticeably, the fabricated WS_2-SAs were mainly applied to the fibre laser systems [17-21]. It is due to the ultrahigh intracavity incident fluence within the single-mode fibre core, and thus readily stimulates the saturable absorption effect of the SA. Nevertheless, the gain per unit length of the rare-earth-doped fibre is relatively lower as compared to rare-earth-doped crystals in the DPSS system, which generally leads to a smaller single pulse energy of pulsed fibre laser. For contributing to the diverse development of the passively pulsed laser systems, it is worth to further investigate the applicability of 2D layered functional material-SA (WS_2) in DPSS system, for instance, Pr: $LiYF_4$ laser [22], Yb: GAB laser [23], and the Nd:YVO_4 laser in this work.

Nd: YAG and Nd: YVO_4 crystals are commonly utilised as the gain medium within the 1 μm DPSS pulsed laser systems and well applied in modern industrial material processing. Compared with Nd: YAG, the Nd: YVO_4 crystal provides the

merits of higher absorption coefficient α_a (Nd: YVO$_4$: 41 cm^{-1}, Nd: YAG: 12 cm^{-1}) and a significant gain cross-section σ_g (Nd:YVO$_4$: 13 to 30 x 10^{-19}, Nd:YAG: ~3.3 x 10^{-19}), and thus is more preferable for utilizing in the DPSS pulsed laser [24]. In this chapter, WS$_2$-SA, which fabricated by radio frequency magnetron sputtering deposition, was applied within the cavity of the Nd:YVO$_4$ DPSS system. The proposed synthesis process has the advantages of cost-saving, large surface area size of the deposited thin film accompanying with high uniformity, and controllable film thickness. To the best of our knowledge, this application of RF magnetron sputtering deposited WS$_2$-SA to the Nd:YVO$_4$ DPSS system is first demonstrated in the nonlinear pulsed laser field.

3.2. Laser cavity design and simulation

For the design of the pulsed DPSS laser system, a compact cavity which consists of 3 laser mirrors was applied and shown in Fig. 3.3(a). In fact, a two-mirror cavity [23] is preferable as compared to the proposed 3-mirrors configuration due to the compactness and lower mirror-induced optical loss. However, due to the deficiency of appropriate laser mirrors, the proposed 3-mirrors cavity was utilised instead. The concave surface of the end mirror was coated with a highly reflective coating at 1064 nm wavelength (HR 1064) and possessed a radius of curvature of 300 mm. Both the two flat surfaces of the middle mirror were coated with a highly transmissive coating at 808 nm wavelength (HT 808), and the inner surface was coated with HR1064 coating as well. The inner flat surface of the output coupler (OC) was coated with a 5 % partially transmissive coating at 1064 nm wavelength

(PT 1064- 5%), and a HT 1064 coating at the outer flat surface as well. The total cavity length is about 144 mm, where the distance between the end concave mirror and the middle mirror is 47 mm, and 97 mm of between the OC and middle mirror. The fabricated transmission-type WS_2-SA was placed 3 mm apart from the OC. The variation of the intracavity spot radius was simulated by using the ABCD matrix method in the computer MathLab program, in which the program code is attached in the appendix of this thesis. As shown in Fig. 3.3(b), the spot radius of the intracavity incident light on the WS_2-SA is around 0.225 mm. Under the limitation of the optical alignment process, the proposed cavity setting and the achieved minimum spot size on the SA is the optimized result in this work.

The utilized laser crystal, $Nd:YVO_4$, was purchased from Castech Inc. Chian which accompanies a dimensional size of 3 mm x 3 mm x 8 mm, and a 0.5 % Nd doping concentration. Besides, the crystal was processed with an a-cut geometric treatment to facilitate the following Q-switching operation [25]. In the experiment, $Nd:YVO_4$ crystal was wrapped with an indium foil and placed in the copper heat sink for inhibiting the thermal lensing effect within the gain media. Afterwards, the gain media was end-pumped by an 808 nm continuous-wave diode laser by using a coupling focus modulus.
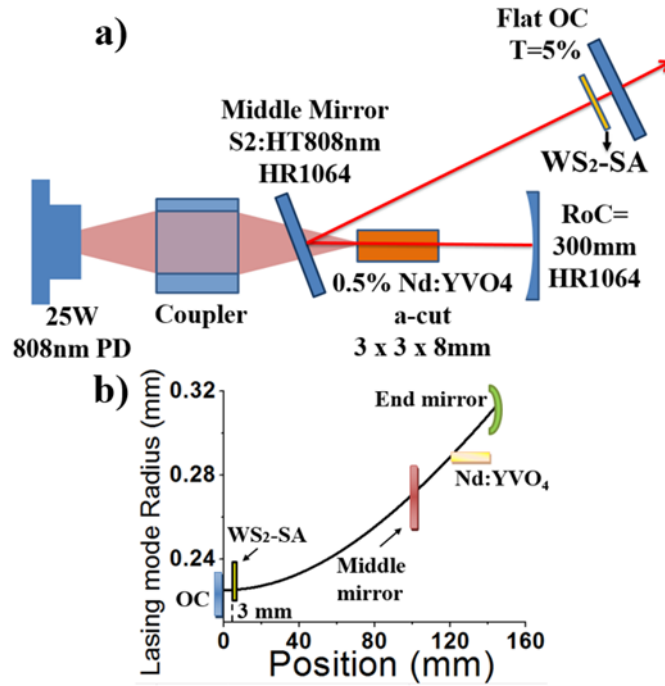
Fig. 3.3 (a) Schematic diagram of the Q-switched Nd:YVO$_4$ DPSS laser. (b) The simulated lasing mode radius variation within the laser cavity (OC-output coupler).

3.3 WS$_2$-SA fabrication and characterization

The fabrication process consists of two steps, in which the magnetron sputtering deposition was followed by a post-annealing process. The WS$_2$ sputtering target was purchased from China New Metal Material Technology Co. Ltd. with a purity of 99.99%. As the WS$_2$ target is non-metallic material, the radio-frequency power source was used instead of direct-current (DC) power. By applying constant RF power of 60W, the thickness of the deposited WS$_2$ thin film can be modulated by controlling the sputtering exposure time. A 2 cm x 2 cm x 1 mm size UV fused quartz was used as the sputtering substrate. Before deposition, the chamber was evacuated to 5×10^{-3} Pa. The deposition was performed at a working pressure of 0.5 Pa. The patial pressure ratio of the sputtering gas of Argon and Oxygen is 16:4, which is an optimized value for facilitating the plasma generation. Since the

49

deposited film (WS₂ precursor) is in the amorphous structure, 2 hours post-annealing process with 800 ℃ temperature is required to form the polycrystalline structure of the WS₂ film as shown in Fig. 3.4. In the post-annealing process, a few mg of sulfur powder was placed at the edge of the tube to produce sulfur vapour, in which the flow of inert gas will carry the sulfur vapour to pass across the WS₂ precursor. This act aims to compensate for the deficiency of S atoms in the deposited WS₂ precursor and thus preserved the stoichiometry. From Fig. 3.5, the characteristic yellowish-green colour of the few-layer WS₂ crystal was observed in the post-annealed WS₂ sample, which suggests the successful synthesis process [26].

As refer to the previous section of intracavity-mode simulation, the minimum intracavity spot radius is located at the position of OC inner surface. Thus the WS₂ thin film can receive relatively higher incident fluence if directly deposited onto the OC and act as a reflective type SA. However, the high annealing temperature may damage the original PT 1064 coating of the OC mirror. Meanwhile, a lengthy laser cavity alignment process is required if the incident area of the reflective type WS₂-SA is damaged by the intracavity light. As a result, a transmissive type SA can provide better flexibility and applicability within the pulsed laser experiment.
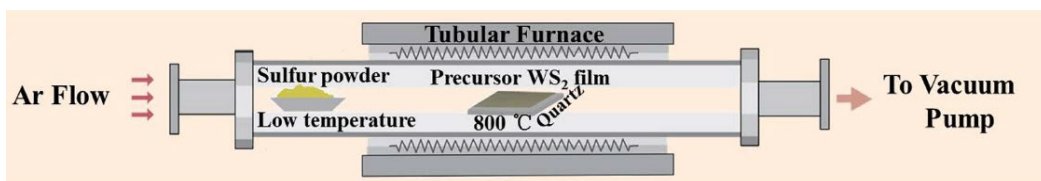
Fig. 3.4 The schematic diagram of the post-annealing treatment [26].
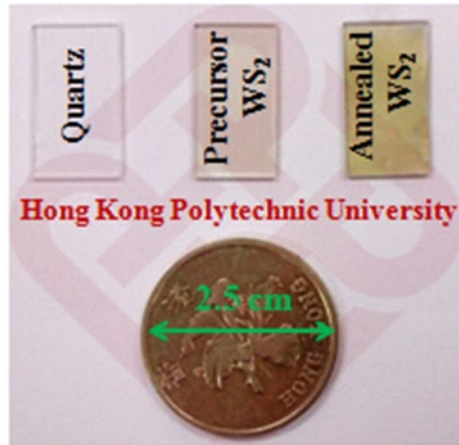
Fig. 3.5 Comparison of the bare quartz (left), WS$_2$ precursor (center), and annealed WS$_2$ film (right).

WS$_2$-SAs, which fabricated under different sputtering exposure time and thus possessed of distinct layer thicknesses, had been tested within the built DPSS laser cavity. Due to the tight material properties requirement for the saturable absorber, only certain WS$_2$-SA candidates had successfully induced the Q-switching effect. Hence the following illustration of characterisation data and Q-switched laser performance solely focused on the optimised WS$_2$-SA sample.

After the synthesis process, the fabricated WS$_2$-SA sample was further characterized. First, the post-annealed WS$_2$ thin film was transferred to the copper grid and characterised by the field-emission transmission electron microscopy (FETEM- JEM-2100F). As shown in Fig. 3.6(a), the fabricated WS$_2$ is composed of hexagonal and triangular single-crystal sheets with few hundreds of nanometers lateral size. Meanwhile, the High-resolution (HR)TEM observation (Fig. 3.6(b)) shows that the thickness of the sample is about 10 layers at the stepped edge. A further SAED measurement confirms the hexagonal crystal structure of the fabricated WS$_2$ sample, where the diffraction pattern of (100) and (110) crystalline planes of WS$_2$ are observed in Fig. 3.6(c). For the chemical purity of the fabricated

samples, the EDS pattern shows that there is none of the impurity consists in the WS$_2$ film and hence proved the production quality of the proposed synthesis method (the element peaks of carbon (C), oxygen (O) and copper (Cu) are originated from the carbon-copper TEM grid substrate).
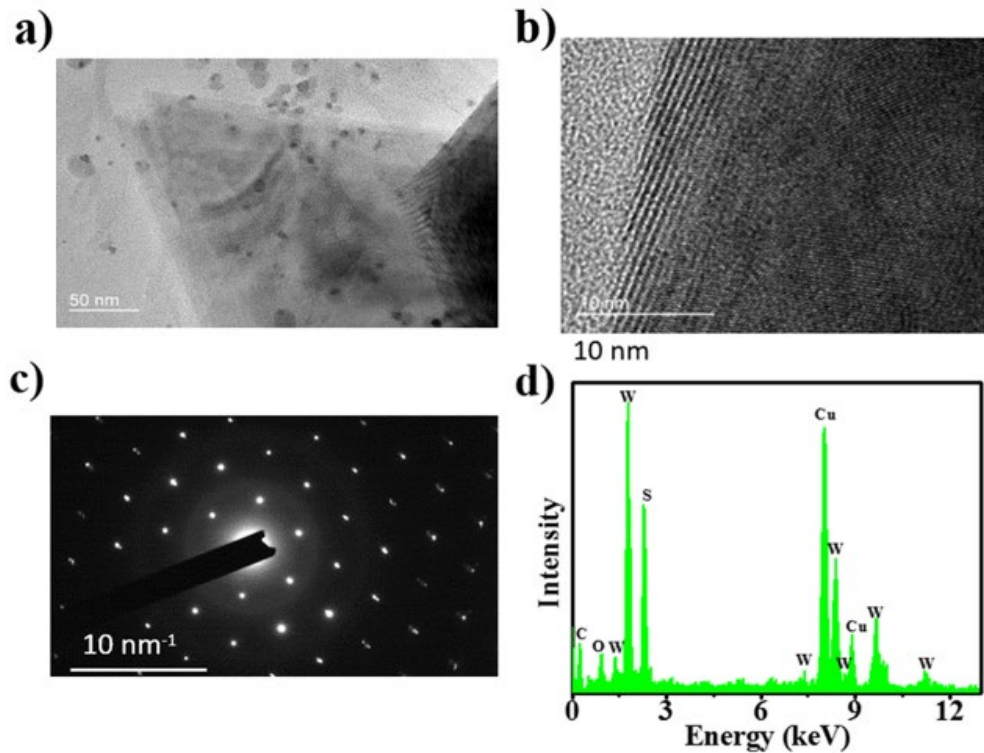
Fig. 3.6 (a) The TEM observation, (b) HRTEM, (c) SAED pattern, and (d) EDS spectrum of the fabricated WS$_2$ sample.

Furthermore, the WS$_2$ film was characterized by Raman spectroscopy with an excitation laser of 488 nm wavelength. As shown in Fig. 3.7(a), two Raman peaks are located at 353.1 cm^{-1} and 417.4 cm^{-1}, which represent the in-plane E$_{2g}$ and out-of-plane A$_{1g}$ mode, respectively. These data are well-matched with the previous literature [26-27] and indicated that the fabricated SA sample is composed of the few-layered WS$_2$ nanostructure. The transmission spectrums of the bare quartz and WS$_2$-SA under excitation of weak intensity light are shown in Fig. 3.7(b), indicates the optimised WS$_2$-SA has an initial absorbance of 3.7 % at 1064 nm wavelength

by subtracted the absorption of the quartz substrate. The atomic force microscopic (AFM) observation (Fig. 3.7(c) & 3.7(d)) indicates the fabricated WS_2 thin film possessed a thickness of 11.05 nm (~18 layers) [28], which cohered with the HRTEM observation result.
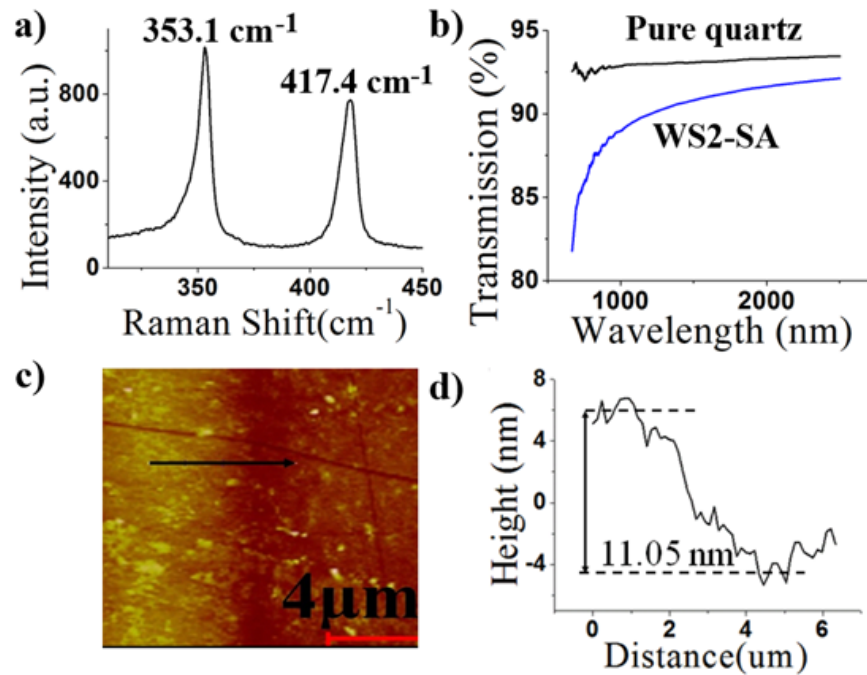
Fig. 3.7 (a) The Raman spectra of the WS_2 film. (b) The transmission spectra of the bare quartz and WS_2 film on the quartz substrate. (c) AFM image, and (d) the corresponding height profile along the black line highlighted in (c).

3.4 Q-switched Nd:YVO$_4$ DPSS laser operation result and discussion

The built Nd:YVO$_4$ DPSS laser has a lasing threshold of 190 mW input pump power and a slope efficiency of 18 % in continuous-wave (CW) operation mode. Once the successful integration of the optimized WS2-SA within the cavity, the input pump power was gradually scaling up to test the capability of laser pulses generation of the fabricated sample. As shown in Fig. 3.8(a), by using a fast photodetector (Thorlabs, DET10A/M) and a digital oscilloscope (LeCroy Wave

Runner 44MXi 400MHz), Q-switched pulses were observed as the input pump power scaled beyond a threshold value of 485 mW. However, the Q-switched pulses have vanished and the output signal restored to CW mode as the input pump power scaled beyond 664 nm, which is due to the over-saturation of the WS_2-SA [29]. The modulation range of the average output power, repetition rate, and pulse duration are 3.33 mW to 19.6 mW, 55 kHz to 135 kHz, and 4.94 μs to 2.3 μs, respectively, as shown in Fig. 3.8(a) and 3.8(b). The achieved maximum single pulse energy is 145 nJ. Fig. 3.8(c) and 3.8(d) show the pulses train and single pulse profile of the Q-switched output at 664 mW input pump power, in which the regular peak intensity of the Q-switched pulses indicated the highly stable operation of the pulsed DPSS laser system.
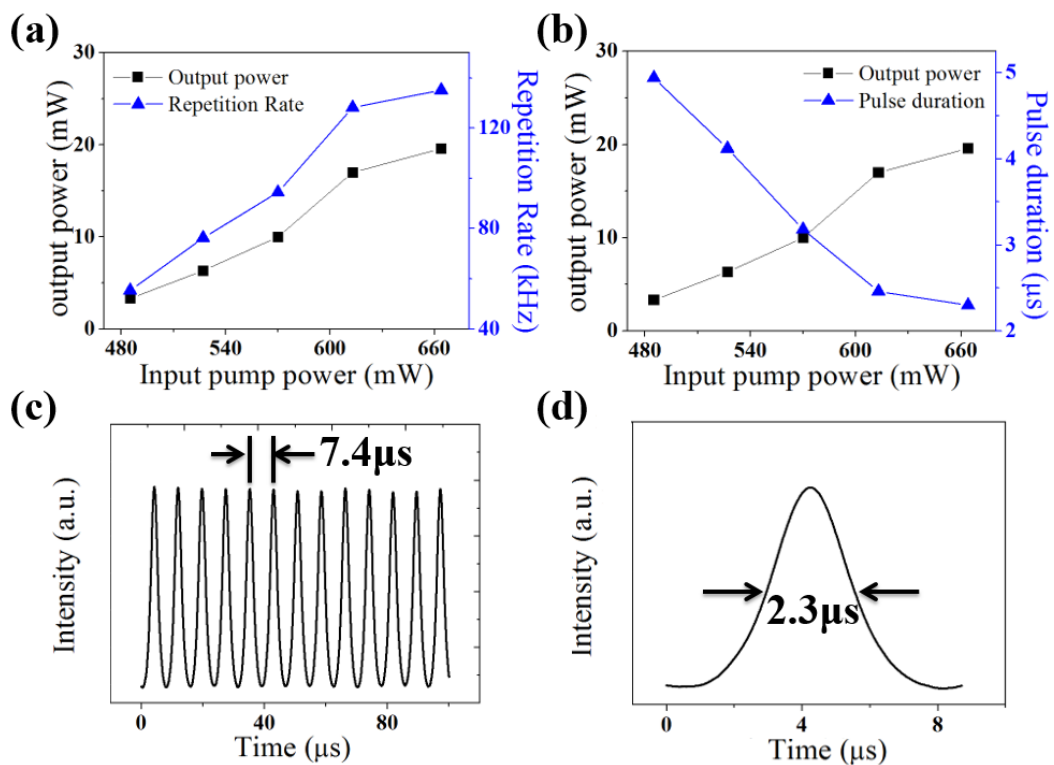
Fig. 3.8 (a) The variation of the repetition rate and output power, (b) pulse duration with respect to the input pump power. (c) Pulses train and (d) single pulse profile of the Q-switched Nd:YVO$_4$ DPSS laser output under 664 mW input pump power.

Besides of the Q-switched operation, a further modification of the input pump power was processed in order to investigate the mode-locking ability of the fabricated WS_2-SA. However, optical damages were observed as the input pump power further scaled up to the relatively high value (> 1W) and there are none of the observable mode-locked pulses as well. Two alternative solutions can be applied in future work. One is the application of a protective layer coating onto the SA surface in order to further enhance the corresponding damage threshold. Simultaneously, the cavity configuration can be further modified to achieve a relative smaller incident spot size onto the SA, in which the SA can receive sufficient incident fluence under lower average intracavity power. Meanwhile, there is another important discovery observed in this work. From the TEM observation of individual post-annealed WS_2 film samples, vertically grown WS_2 nanosheets were observed. Based on this observation, further investigations and experimental works had shown that the grown direction of the TMDs nanosheets can be modulated by controlling the stoichiometry and thickness of deposited precursor film, as well as the post-annealing conditions. Different from the horizontally grown TMDs nanosheets, the vertically grown structure provides the merits of a high density of active edge sites [30], which may contribute to extensive optoelectronic applications. Recently, this valuable grown technique had further applied to different TMDs candidates (e.g.: $PtSe_2$, as shown in Fig. 3.9) for fabricating practical optoelectronic devices, including photodetector [31], hydrogen evolution [30], and saturable absorber as well [32]. Noticeably, the effect of TMDs nanosheets orientation to the pulsed laser performance is currently investigating.
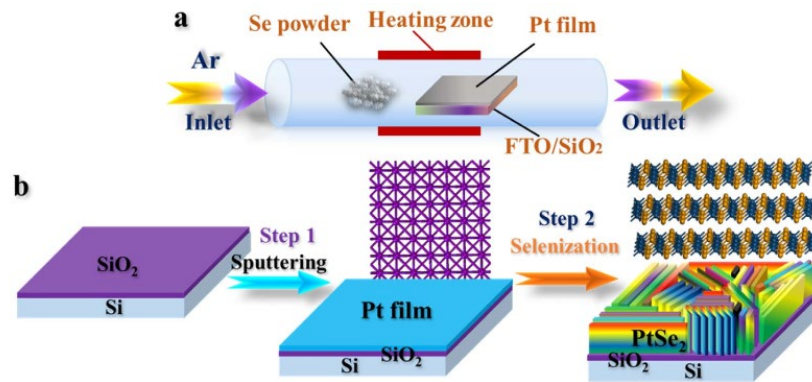
Fig. 3.9 The schematic synthesis process of vertically grown PtSe$_2$ thin film on SiO$_2$/Si substrate [30].

Restricted by the experimental conditions, Q-switched operation, which based on the magnetron sputtering deposited WS$_2$-SA, was solely be demonstrated. The achieved maximum single pulse energy of 145 nJ in this work is comparable to the results of other WS$_2$-SA based Q-switched systems as shown in Table. 3.1. The successful Q-switching demonstration in this work had contributed to the diverse development of the pulsed laser systems, in which the further optimization of the WS$_2$-SA and introduction of another novel TMDs-SAs within the DPSS laser system are in progress now.

Table 3.1 Comparison of WS$_2$-SA based passively Q-switched lasers (EDFL: erbium-doped fiber laser, YDFL: ytterbium-doped fiber laser)

Gain media	Center wavelength (nm)	Maximum average output power (mW)	Maximum single pulse energy (nJ)	Ref
Nd: YVO$_4$	1064	19.6	145	This work
EDFL	1570	5.3	46.3	17
EDFL	1567	2.5	19	18
EDFL	1558	16.4	179.6	20
YDFL	1030	/	13.6	20
Pr:YLF	639.3	21.5	240	22

3.5 Chapter summary

In this chapter, WS_2-SA based passively Q-switched DPSS $Nd:YVO_4$ laser is experimentally demonstrated. The transmissive type WS_2-SA was fabricated by a two-step synthesis method, which consists of RF magnetron sputtering deposition of WS_2 precursor and followed by a post-annealing treatment. The Q-switched performance achieved in this work is comparable to other WS_2-SAs based laser systems, which proved the promising saturable absorption ability of the fabricated sample. This work showed the applicability of the proposed synthesis method as well as the adaptability of the fabricated SA in the DPSS laser system. Remarkably, the proposed synthesis method grants the possibility of modulating the nanosheets grown direction, which motivated a further study on the dependence of the pulsed laser performance on TMDs nanosheet grown orientation.

3.6 References

1. D. Xu, Y. Wang, H. Li, J. Yao, and Y. H. Tsang, "104 W high stability green laser generation by using diode laser pumped intracavity frequency-doubling Q-switched composite ceramic Nd: YAG laser," Opt. Exp. , vol. 15, no. 27, pp. 3991-3997, (2007).
2. Y. H. Tsang, and D. J. Binks, "Record performance from a Q-switched Er3+:Yb3+:YVO$_4$ laser," Appl. Phys. B Lasers and Optics, vol. 96, pp. 11-17, (2009).
3. R. L. Byer., "Diode laser-pumped solid-state lasers," Science, vol. 239, no. 4841, pp.742-745, (1988).
4. B. Davarcioglu, "An Overview of Diode Pumped Solid State (DPSS) Lasers," Int. Acad. Arts. Sci. Technol., vol. 1, (2010).
5. R. A .Fields, M. Birnbaum, and C. L. Fincher, "Highly efficient Nd: YVO$_4$ diode-laser end-pumped laser," Appl. Phys. Lett. 51(23), 1885-1886(1987).
6. B. Mahler, V. Hoepfner, K. Liao, and G. A. Ozin, "Colloidal synthesis of 1T-WS$_2$ and 2H-WS$_2$ nanosheets: applications for photocatalytic hydrogen evolution," J. Amer. Chem. Soc. 136(40), 14121-14127(2014).
7. F. Wypych, and R. Schöllhorn, "1T-MoS$_2$, a new metallic modification of molybdenum disulfide," J. Chem. Soc. Chem. Commun. (19), 1386-1388(1992).
8. R. I. Woodward, R. C. T. Howe, G. Hu, F. Torrisi, M. Zhang, T. Hasan, and E. J. R. Kelleher, "Few-layer MoS$_2$ saturable absorbers for short-pulse laser technology: current status and future perspectives," Photon.Res. 3(2), A30-A42(2015).
9. H. R. Gutiérrez, N. Perea-López, A. L. Elías, A. Berkdemir, B. Wang, R. Lv, and M. Terrones, "Extraordinary room-temperature photoluminescence in triangular WS$_2$ monolayers," Nano Lett. 13(8), 3447-3454(2012).
10. W. J. Schutte, J. L. Deboer, F. Jellinek, "Crystal-Structures of Tungsten Disulfide and Diselenide," J. Solid State Chem.70, 207−209(1987).
11. R. I. Woodward, and E. J. Kelleher, "2D saturable absorbers for fiber lasers," Appl. Sci. 5(4), 1440-1456(2015).
12. K. S Novoselov, D. Jiang, F. Schedin, T.J. Booth, V.V. Khotkevich, S.V. Morozov, A.K. Geim, "Two-dimensional atomic crystals," Proc. Natl. Acad. Sci. USA, 102, 10451–10453(2005).
13. Q.H. Wang, K. Kalantar-Zadeh, A. Kis, J.N. Coleman, M.S. Strano, "Electronics and optoelectronics of two-dimensional transition metal dichalcogenides," Nat. Nanotechnol.,7, 699–712(2012).
14. C. Ballif et al. "Preparation and characterization of highly oriented, photoconducting WS$_2$ thin films," Appl. Phys. A: Mater. Sci.Process.,62, 543−546(1996).
15. K. Wang, J. Wang, J. Fan, M. Lotya, A. O'Neill, D. Fox, and H. Zhang, "Ultrafast saturable absorption of two-dimensional MoS2 nanosheets," ACS nano, 7(10), 9260-9267(2013).
16. X. Fu, J. Qian, X. Qiao, P. Tan, and Z. Peng, "Nonlinear saturable absorption of vertically stood WS$_2$ nanoplates," Opt. Lett. 39(22), 6450-6453(2014).
17. K. Wu, X. Zhang, J. Wang, X. Li, and J. Chen, "WS$_2$ as a saturable absorber for ultrafast photonic applications of mode-locked and Q-switched lasers," Opt. Exp. 23(9), 11453-11461, (2015).
18. S. H. Kassani, R. Khazaeinezhad, H. Jeong, T. Nazari, D.I. Yeom, and K. Oh, "All-fiber Er-doped Q-Switched laser based on Tungsten Disulfide saturable absorber," Opt. Mat. Exp. 5(2), 373-379, (2015).
19. D. Mao, Y. Wang, C. Ma, L. Han, B. Jiang, X. Gan, S. Hua, W. Z. T. Mei, and J.I. Zhao, "WS$_2$ mode-locked ultrafast fiber laser," Sci. Rep. 5(7965), 1-7, (2015).
20. M. Zhang, G. Hu, G. Hu, R. C. T. Howe, L. Chen, Z. Zheng, and T. Hasan, "Yb- and Er-doped fiber laser Q-switched with an optically uniform, broadband WS$_2$ saturable absorber," Sci.Rep. 5(17482), (2015).
21. R. Khazaeinezhad, S. H. Kassani, H. Jeong, D. I. Yeom, and K. Oh, "Femtosecond Soliton Pulse Generation Using Evanescent Field Interaction Through Tungsten Disulfide (WS$_2$) Film," J. Lightwave Tech., 33(17), 3550-3557, (2015).
22. Y.Cheng, J. Peng, B. Xu, H. Yang, Z. Luo, H. Xu, and J. Weng, "Passive Q-switching of a diode-pumped Pr: LiYF$_4$ visible laser using WS$_2$ as saturable absorber," IEEE Photon. J. 8(3), 1-6(2016).
23. X.Wang, J. Xu, Z. You, Y. Sun, Z. Zhu, and C.Tu, "Tri-wavelength passively Q-switched Yb^{3+}: GdAl$_3$ (BO$_3$) 4 solid-state laser based on WS$_2$ saturable absorber," Opt. Mat. 62, 621-625(2016).
24. Y. Bai, N. Wu, J. Zhang, J. Li, S. Li, J. Xu, and P. Deng, "Passively Q-switched Nd: YVO$_4$ laser with a Cr^{4+}: YAG crystal saturable absorber," Appl. Opt. 36(12), 2468-2472(1997).
25. A. Agnesi, and S. Dell'Acqua, "High-peak-power diode-pumped passively Q-switched Nd: YVO$_4$ laser," Appl. Phys. B 76(4), 351-354(2003).
26. L. Zeng, L. Tao, C.Y. Tang, B. Zhou, H. Long, Y. Chai, and Y. H. Tsang, "High-responsivity UV-vis photodetector based on transferable WS$_2$ film deposited by magnetron sputtering," Sci. rep. 6, 20343(2016).
27. Perea-Lopez, N. et al. "Photosensor Device Based on Few-Layered WS$_2$ Films," Adv. Funct. Mater. 23, 5511–5517 (2013).
28. F. Cheng, A. D. Johnson, Y. Tsai, P. H. Su, S. Hu, J. G. Ekerdt, and C. K. Shih, Enhanced "Photoluminescence of Monolayer WS$_2$ on Ag Films and Nanowire–WS$_2$–Film Composites," ACS Photon. 4(6), 1421-1430(2017).
29. Y. Huang, Z. Luo, Y. Li, M. Zhong, B. Xu, K. Che, and J. Weng, "Widely-tunable, passively Q-switched erbium-doped fiber laser with few-layer MoS$_2$ saturable absorber," Opt. Exp. 22(21), 25258-25266(2014).
30. S. Lin, Y. Liu, Z. Hu, W. Lu, C. H. Mak, L. Zeng, and X. Zhang, "Tunable active edge sites in PtSe$_2$ films towards hydrogen evolution reaction," Nano Energy, 42, 26-33(2017).
31. L. H. Zeng, S. H. Lin, Z. J. Li, Z. X. Zhang, T. F. Zhang, C. Xie, and Y. H. Tsang, "Fast, self-driven, air-Stable, and broadband photodetector based on vertically aligned PtSe2/GaAs heterojunction," Adv. Funct. Mat. 28(16), 1705970(2018).
32. L. Tao, X. Huang, J. He, Y. Lou, L. Zeng, Y. Li, H. Long, J. Li, L. Zhang, and Y. H. Tsang, "Vertically standing PtSe2 film: a saturable absorber for a passively mode-locked Nd: LuVO4 Laser," Photon. Res. 6, 750-755, (2018).

CHAPTER 4

Passively Q-switched and mode-locked fibre laser based on group-10 TMDs-SA

Besides of the DPSS laser, based on the larger amplification bandwidth of the rare-earth-doped fibre, ultrashort laser pulses are readily generated within the fibre laser system. In this chapter, the synthesis, and application of TMDs based SA within Erbium-doped fibre laser (EDFL) were demonstrated. Meanwhile, the study of the saturable absorption ability of 2D layered functional materials has extended to the newly developed group-10 Platinum (Pt) based TMDs. The mode-locked EDFL, which based on PtS_2-SA and $PtTe_2$-SA, shown comparable performance with respect to other TMDs-SAs based literature.

4.1 Background and motivation

As demonstrated in the previous section, the stable operation and high single pulse energy make the DPSS pulsed laser still one of the most applicable processing systems within the modern industrial market. Noticeably, the market share of fibre lasers, including short-pulse and ultrashort-pulse fibre laser, is gradually increasing in recent years. The sustained development and advantages of compactness, robustness, freedom from misalignment and cost-saving [1-2] had conferred significant competitiveness to fibre laser as compared to the conventional DPSS system (e.g. Ti:Sapphire Femtosecond lasers). Meanwhile, the

59

bandwidth of the fibre gain media, such as ytterbium-doped silica fibre, is comparable ($\sim 2\pi \times 11$ rad THz) to Ti:Sapphire, which also make the fibre laser as an ideal platform for ultrashort pulses generation [3].

In a passively mode-locking or Q-switching laser cavity, to provide sufficient incident fluence to SA for inducing either Q-switching or mode-locking, it can directly scale up the intracavity average power. However, an excess power magnitude may deteriorate the thermal-induced damaging problem within the SA. The alternative method is to reduce the spot size of intracavity incident beam to enhance the light intensity. As refer to the previous work, in an Nd:YVO$_4$ DPSS mode-locked laser cavity (Fig. 4.1), the optimised beam spot radius on SA is merely around 40 μm to 50 μm [4]. And it is difficult to further scale down the spot radius by modulating the radius of curvature and numbers of the concave reflective mirror due to the limitation of alignment process. In fibre laser system, contributed by the ultra-small core radius of the single-mode fibre (~ 4 μm), the achieved incident fluence on SA is significantly higher than that of the DPSS cavity (assume both cavities under the condition of same intracavity power). Figure 4.2 summarises several commonly utilised SA designs for applying in the fibre laser cavity [5]. These SA designs can briefly divide into three types. The first one is shown in Fig. 4.2(a), where the functional material is coated on a highly transmissive substrate to form SA [6]. The SA material interacts with the intracavity beam by using a free-space coupling process which is similar to the DPSS pulsed system shown in chapter 3. The second type is to place the SA material right behind the end-face of the fibre connector, as shown in Fig. 4.2 (b) to 4.2(d). The functional material can be incorporated into polymer material to

form a matrix composite thin film followed by sandwiching between two fibre connectors (Fig. 4.2(b)) or directly deposited on laser mirror (Fig. 4.2(c)) / fibre end-face (Fig. 4.2(d)). As mentioned above, due to the ultra-small core radius of single-mode fibre, the achieved incident fluence is remarkably elevated by utilising this type of SA incorporation method. However, these methods are not thoroughly free from thermal damage, in which the ultrahigh intracavity power still pose a threat to the SA. Therefore, a third alternative incorporation type is proposed where the functional material is deposited onto the side-polished fibre or tapered fibre. The evanescent field of propagating light will interact with the functional material and act as SA. Due to the long interaction length, it does not require a high-intensity beam to interact with the functional material, and thus mitigated the thermal-induced damage of the SA. In this work, to study the applicability of 2D layered functional material within fibre laser, TMDs based SAs were incorporated into Erbium-doped fibre laser (EDFL) cavity to induce laser pulses generation, and the influence of SA incorporation methods to the lasing performance will be discussed in the following section.
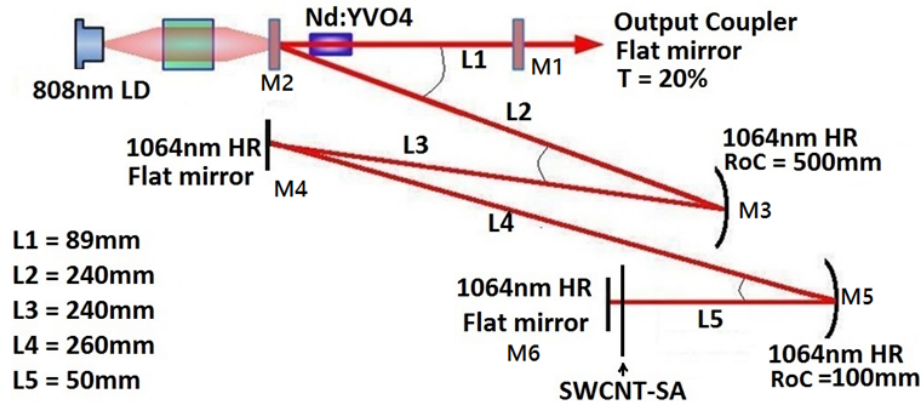
Fig. 4.1 A schematic diagram of the SWCNT-SA based Nd:YVO$_4$ mode-locked laser [4].
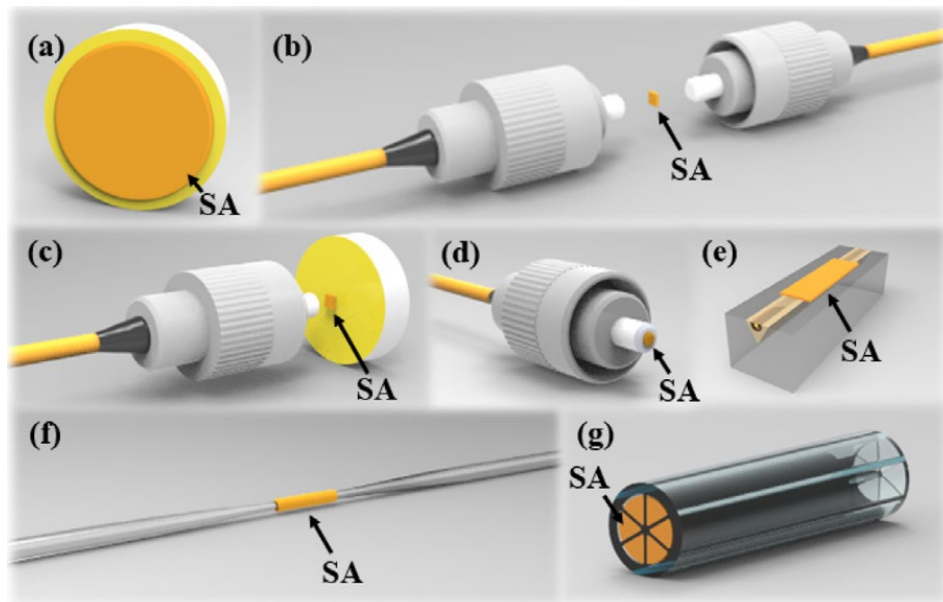
Fig. 4.2 General incorporation methods for functional material saturable absorbers: (a) SA materials deposited on the specific substrates for free-space coupling. (b) SA incorporated polymer or sol-gel thin film sandwiched between two fibre connectors. SA materials deposited on (c) a reflective mirror, (d) fibre end-surface. (e) side polished fibre, (f) tapered-fibre. (g) SA dispersed sol-gel or suspensions filled into the photonic crystal fibre [5]

Meanwhile, the investigation subject has extended from 2D layered group 6 TMDs to the newly developed group-10 Platinum-based candidates. Different to the WS$_2$ crystal structure, the PtX$_2$ has a space group of P$\overline{3}$m1 and two individual crystal structures, 1T and 3R phases, as shown in Fig. 4.3 [7-8]. Both 1T and 3R structure possess octahedral coordination in each unit layer. The difference

between the two structures is originated from the layer stacking manner, where a "AA" format is presented in the 1T phase, and an "ABC" format has occurred in the 3R phase. From literature, it shows that the 1T phase is a comparatively stable structure for the PtX_2 material, where the typical synthesis methods of chemical vapour transport and post-annealing of Pt precursor film will result in 1T PtX_2 structure [7, 9]. The utilised Pt-TMDs in this work is synthesised in 1T structure, and thus the following discussion will focus on the properties of 1T PtX_2 materials solely.

Likes other TMDs, the first study of group-10 TMDs can be dated back to the 50s of the last century [10]. However, the 2D nature and layer-dependent material properties of the group-10 TMDs had not been comprehensively explored at that time. Recently, due to the development of new synthesis methods, the study on group-10 TMDs has rejuvenated once again. Experimental works had demonstrated the prominent material properties and corresponding applications of the Pt-based TMDs [7-9, 11-12]. Remarkably, Pt-based TMDs possess superior air stability [9, 13-14] as compared to other 2D function material, for instance, BP [15], MXene [16-17] and group-6 TMDs (WTe_2 [18-19]). Air stability is a crucial factor for the stable operational performance of functional materials-based optoelectronic devices, especially saturable absorber. Oxygen or humidity-sensitive materials require complex and lengthy passivation process to curb material degradation, which inevitable tapered off the practicability of the devices. As a successor of group 6 family, the study of group-10 TMDs-based SA is just in the beginning within the past two years. Up to the present, the group 10 TMDs-SA applications are mainly reported on $PtSe_2$ [20-23], and thus a further study and

exploration of others Pt-based candidates (PtS$_2$-SA and PtTe$_2$-SA) would be favourable to the understanding of nonlinear optical properties of novel Platinium based dichalcogenides.
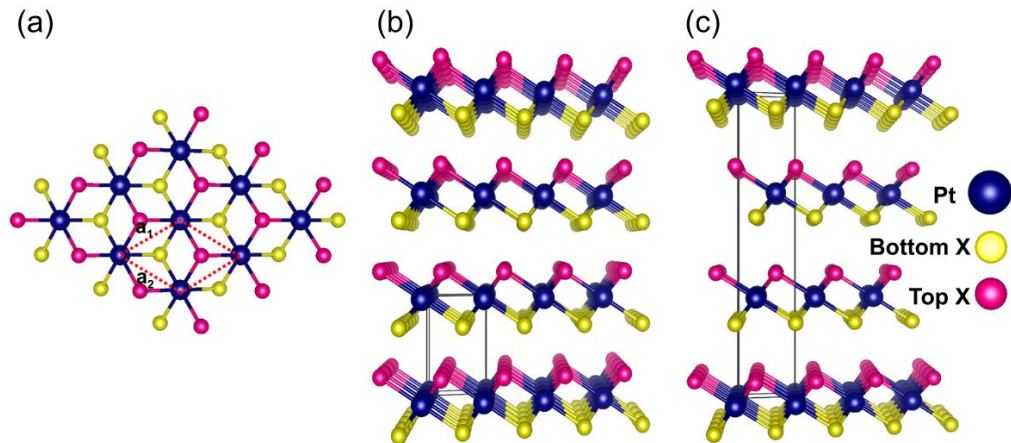
Fig. 4.3 (a)The top view of a 1T layered structure of PtX$_2$. The side view of (b) 1T and (c) 3R structure of the PtX$_2$ [7].

4.2 Passively mode-locked Erbium-doped fibre laser based on PtS$_2$-SA

In recent years, several pioneering works had explored unique material properties of Platinum disulfide (PtS$_2$), which attracted tremendous attention and further application study on this newly developed platinum-based dichalcogenide within the research community. For instance, PtS$_2$ exhibits a charge carrier mobility of 1107 cm^2 V^{-1} s^{-1} at room temperature [24-25], which is comparable or even superior to the black phosphor (BP) [26], not to mention of the competitiveness of high air stability. Within the platinum-based TMDs family, PtS$_2$ has tunable bandgap energy ranged from 0.25 eV (4960 nm) for bulk to 1.6 eV (775 nm) for monolayer. Meanwhile, Platinum diselenide (PtSe$_2$) has an indirect bandgap of 1.18 eV (1050 nm) and 0.21 eV (5904 nm) in the monolayer and bilayer form, respectively (3 layers to bulk: semi-metallic). And Platinum Ditelluride (PtTe$_2$) has the smallest

monolayer indirect bandgap of 0.4 eV (3100 nm, 2 layers to bulk: semi-metallic) within the Platinum TMDs family [7]. The sizable bandgap energy of PtS_2 is even wider than that of group 6 MoS_2 (1.2 eV to 1.8 eV [27]) and WS_2 (1.3 eV to 2.1 eV [28]), which provides design flexibility for various optoelectronic application, for instance, field-effect transistor [29]. Noticeably, the Platinum TMDs family has not shown the shift from indirect-to-direct bandgap as the layer thickness reduces from bulk to monolayer, which is different from that of other TMDs, e.g. group 6 Mo or W based TMDs in 2H phase. The main reason is the difference in the crystal structure, in which PtX_2 (X = S, Se, Te) generally has the 1T structure and thus significantly affect the electronic properties behaviours. However, the inverse relationship between the bandgap magnitude and the layer thickness is still observed in PtX_2 family due to quantum confinement effect and interlayer interaction effect [7]. In this section, the experimental detail of a passively mode-locked erbium-doped fiber laser which based on PtS_2-SA is demonstrated.

4.2.1 PtS_2-SA based mode-locked EDFL cavity setup

As shown in Fig 4.4, an Erbium-doped fibre ring cavity setup was utilised to test the mode-locking ability of the fabricated PtS_2-SA. The cavity was composed of a 0.7 meter long Erbium-doped single-mode fibre (LIEKKITM Er 110- 4/125, cut-off wavelength: 890 ± 90 nm, 110 dB/m absorption at 1530 nm), a 980 nm/1550 nm wavelength-division multiplexer (WDM), a 10 % output coupler, a polarisation-independent isolator and an in-line polarisation controller. The total cavity length is around 10 meters. For the SA insertion, the exfoliated PtS_2

nanosheets were incorporated into polyvinyl alcohol (PVA) polymer to form a matrix composite thin film and followed by sandwiching between two FC/APC fibre connectors. The utilisation of the APC connector instead of PC type is to eliminate the parasitic reflection and ensure the operational stability of the mode-locked system.
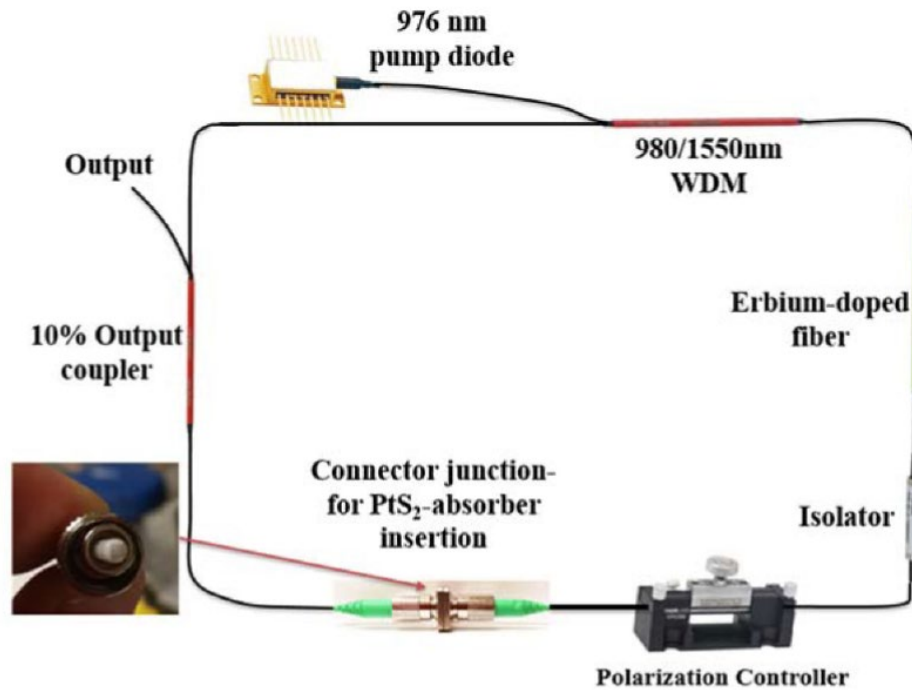
Fig. 4.4 The schematic diagram of the PtS$_2$-SA based passively mode-locked Erbium-doped fibre laser cavity setup.

4.2.2 The fabrication and characterisation of PtS$_2$-SA

The synthesis of the PtS$_2$-SA was started from the exfoliation of the bulky form sample. 1 gram of PtS$_2$ powder, which purchased from Sigma-Aldrich Inc., was first mixed with 100 mL N-Methyl-2-pyrrolidone (NMP) solvent and followed by an ultrasonic exfoliation for exceed 8 hours. The temperature of the exfoliating solution was remaining at 29 ℃ to prohibit the degradation of the powder.

Before incorporating the exfoliated nanosheets into PVA polymer, the material quality of the prepared PtS_2 samples was characterised. Fig. 4.5(a) shows the TEM observation (FETEM- JEM-2100F) of the prepared PtS_2 nanosheet, where the nanosheets lateral size is around two hundred nanometers. Meanwhile, the HRTEM image shows an inter-plane distance of 0.326 nm which well match with the (100) planes of the PtS_2 crystalline structure. Furthermore, as shown in Fig. 4.5(b), the selected area electron diffraction (SAED) pattern indicates the hexagonal lattice structure of PtS_2 with diffraction points corresponding to (110), (011), and (100) planes and demonstrates that the prepared PtS_2 sample possesses with polycrystalline structure. Fig. 4.5(c) shows the XRD measurement pattern (XRD, Bruker D8 Advance) of the PtS_2 sample, where the diffraction peaks (2θ) located on 29° and 55° represent the crystalline plane of (100) and (111), respectively. This XRD observation agrees well with the hexagonal phase (JCPDS File no. 70–1140 [30]). The chemical composition and the stoichiometric ratio of the PtS_2 sample were inspected by dispersive X-ray spectroscopy (EDS, JEOL Model JEM-2011, 2000 kV) and shown in Fig. 4.5(d). From the pattern, none of any impurity was observed (Cu peak is due to copper mesh utilised in EDS measurement). The measured atomic ratio of the PtS_2 sample is around 1:2 (Pt: 32.87% and S: 67.13%), which suggests a good material quality of the prepared sample.

The morphology of the prepared sample was measured by the atomic force microscopy (Veeco Nanoscope V), where Fig. 4.6(a) and 4.6(b) show the topography of two randomly selected nanosheets and the corresponding height profiles, respectively. The lateral size of the two nanosheets were around 150 nm

which agrees with the TEM observation. Besides, the thickness distribution (obtained by analysing 100 AFM data) shows an average value of 3.2 nm, which indicates around 6 atomic layers of the PtS_2 nanosheets.
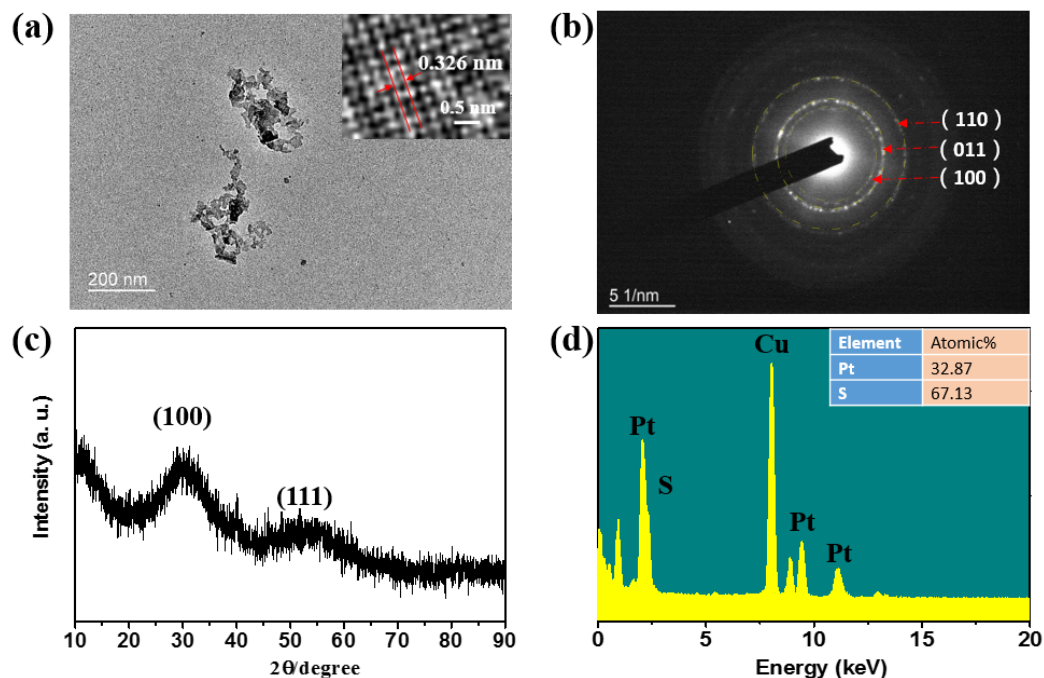
Fig. 4.5 (a) TEM observation (insert with HRTEM image), (b) selected area electron diffraction (SAED), (c) XRD pattern, and (d) EDS spectrum of the prepared PtS_2 nanosheets.
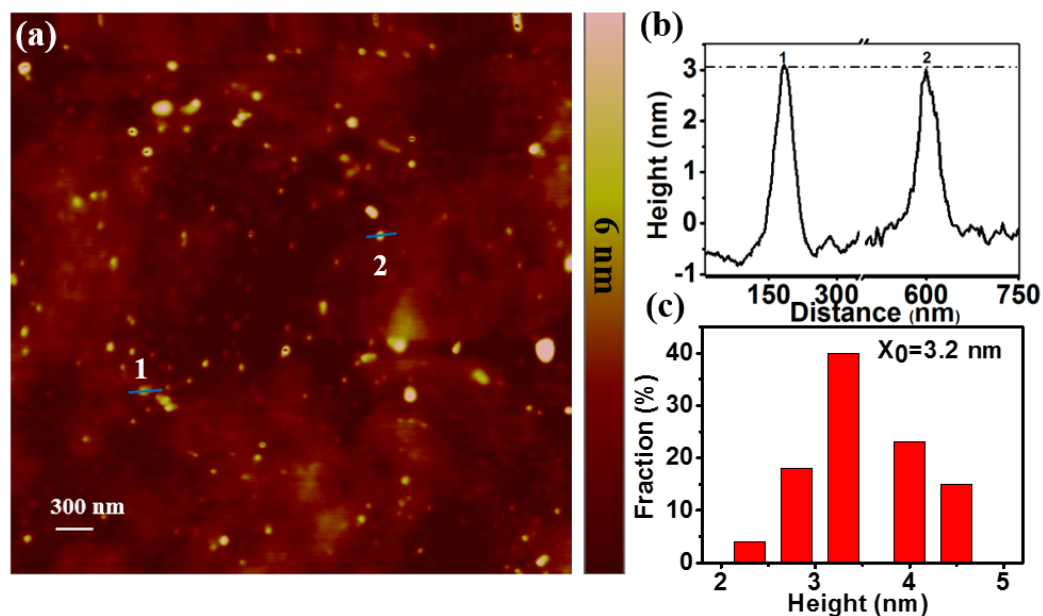
Fig. 4.6 (a) AFM observation of PtS_2 nanosheets, (b) the height profile correspond to the section marked in (a), and (c) the thickness distribution of the PtS_2 nanosheets.

After the characterization, 1 g PtS$_2$ supernatant was mixed with 15 wt% PVA gel-like solution and stirred for 30 minutes. Then the mixture was dried in an oven under 60 °C for 48 hours to form a PtS$_2$-PVA composite thin film. Before insertion within the fibre laser cavity, the nonlinear absorption properties of the PtS$_2$-SA was measured by using a twin-balanced detector measurement system. The laser source of the measuring system possesses 3 ps pulse duration and 1572 nm centre wavelength. Equation 4.1 was utilised to fit the experimental data [31], where $T(I)$ is the optical intensity-dependent transmission, ΔT is the modulation depth, I_{sat} is the saturable intensity, and T_{ns} is the non-saturation loss.

$$T(I) = 1 - \Delta T \cdot \exp\left(\frac{-I}{I_{sat}}\right) - T_{ns} \qquad \text{(Eq. 4.1)}$$

This equation is built based on the Beer-Lambert law $I_t = I_i \exp(-\alpha_0 L)$, which describe the decay of light intensity through a transparent medium, and the saturable absorption coefficient equation (Eq 2.13). Fig. 4.7 shows the measured nonlinear input intensity-dependent transmission curve of the prepared PtS$_2$-SA, where the estimated modulation depth and saturable intensity are 7 % and 9 MW/cm^2, respectively.
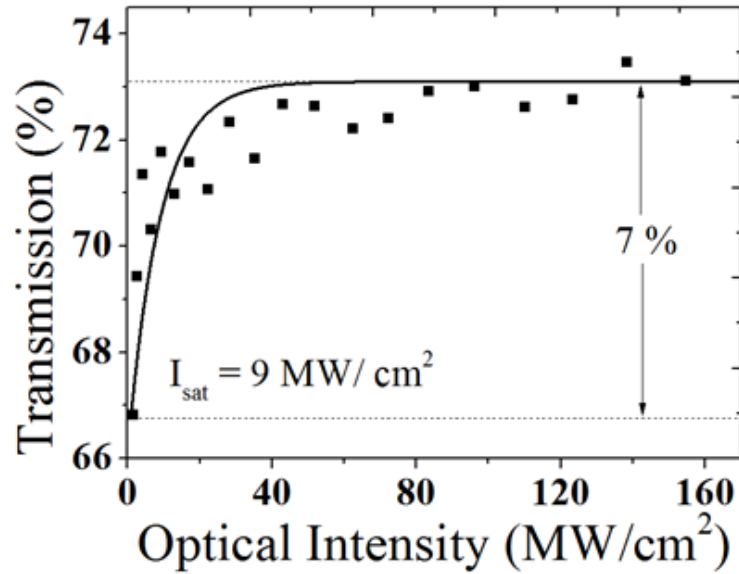
Fig. 4.7 The measured nonlinear saturable absorption of prepare PtS_2-SA.

4.2.3 PtS_2-SA based mode-locked EDFL laser performance and discussion

As mentioned previously, the PtS_2-SA was inserted within the fibre cavity by sandwiching between two connectors, and an insertion loss of 4 dB was recorded. Afterwards, by gradually scaling up the input pump power to the threshold value of 45.7 mW, stable continuous-wave (CW) mode-locked pulses were observed. The pulse train was recorded by using a 1.2 GHz photodetector (Thorlab DET01CFC) and a 400 MHz oscilloscope (Lecroy Waverunner 44MXi), as shown in Fig. 4.8. From the pulse interval time of 66.5 ns, the calculated repetition rate is 15.04 MHz. The obtained repetition rate matches with the cavity length as well as the round trip cavity time, which indicates the successful mode-locked operation within the laser cavity. As the input pump power further scaled beyond 89.1 mW,

the CW mode-locking operation was vanished and restored to CW mode, which is due to the over-saturation of the SA [32-33]. As shown in Fig 4.9(a), the maximum achieved average output power is 1.11 mW. Meanwhile, RF spectra had also recorded which spectra in a span of 20 MHz with RBW of 40 kHz is shown in Fig. 4.9(b). The SNR value is up to 43 dB, indicating high stability of the mode-locked operation. The wavelength spectrum of the pulsed output is shown in Fig. 4.9(c), the centre wavelength is located at 1572 nm with a 3dB bandwidth of 2.47 nm. Moreover, the pulse duration of the mode-locked pulses was measured by using autocorrelator (Femtochrome FR-103XL). The autocorrelation trace was well fitted by the gaussian function, and the measured pulse duration is 2.064 ps. The calculated time-bandwidth product is 0.62, which suggests that the output pulses are not transform-limited and able to be further shortened (The minimum time-bandwidth product of Gaussian-shaped pulses: ~0.44).
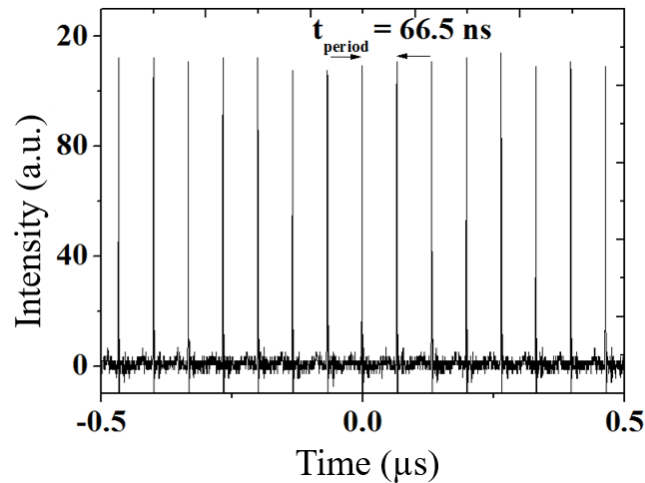
Fig 4.8 The observed CW mode-locking pulse train of the Er-doped fibre laser.
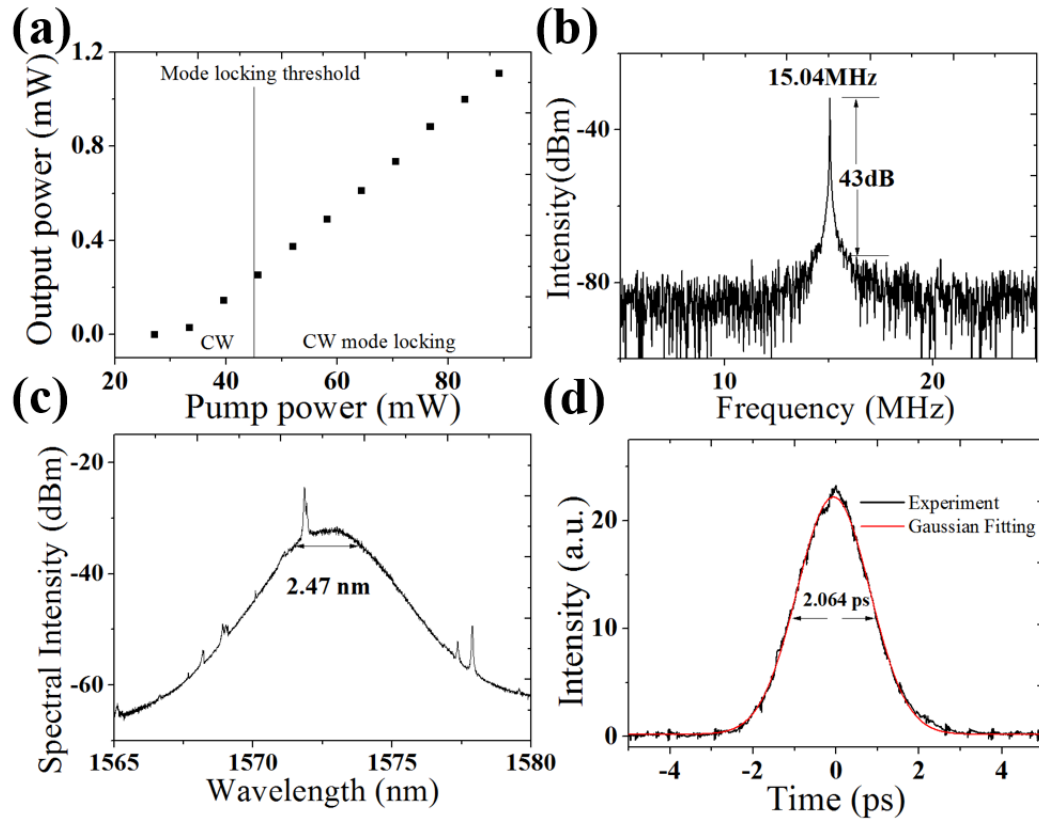
Fig. 4.9 (a) The average output power vary with input pump power. (b) RF spectra, (c) optical spectrum, and (d) autocorrelation trace of the mode-locked EDFL at the maximum input pump power of 89.1 mW.

The average output power and single pulse energy of the PtS_2-SA based mode-locked EDFL are relatively low. In fact, it can be compensated by optimising the cavity setup or applying post-amplification. In order to commercialise new type SAs, the operational stability of the SA is far more critical than the average output power of the mode-locked seed laser source. For the PVA-based PtS_2-SA applied in this work, the fluctuation of average output power and wavelength spectrum are less than 5 % within around 30 minutes measurement period. However, gradual degradation was observed under prolonged operation. The polymer holder is not suitable for long-term operation accompanying with high-intensity illumination. Hence, it is worth to test different substitutional SA incorporation methods and

which motivated the utilisation of side-polished fibre as the SA material substrate holder. The application of SPF-based $PtTe_2$-SA and corresponding mode-locked laser performance will be demonstrated in the following section.

Table 4.1 shows several mode-locked EDFL lasing performances which based on low-dimensional material-SAs. The modulation depth, as well as the pulse duration achieved in this work, is comparable to another group 6/10 TMDs or mono-element 2D material-SAs based mode-locked EDFL, which implies that the PtS_2 is definitely a strong competitor for application as nonlinear saturable absorbers. Besides, as a semiconductor-type TMD, the layer thickness of the PtS_2 will affect its energy bandgap structure and subsequently alternating the nonlinear saturable absorption properties, in which, the size and thickness-dependent optical nonlinearity of atomically thin PtS_2 will be discussed in the next chapter.

Table 4.1 Comparisons of mode-locked Er-doped fibre laser based on low-dimensional material SAs. (SPF: side polished fibre, PVA: Polyvinyl alcohol, BP: Black phosphorus)

SA Materials	SA form	Modulation depth	Saturable Intensity	Center Wavelength	3dB bandwidth	Pulse width	Ref.
MoS_2	Direct deposit on fiber end face	35.4 %	0.34 MW/cm^2	1568.9 nm	2.6 nm	1.28 ps	[34]
$MoSe_2$	Deposit on SPF	1.4 %	/	1557.1 nm	2.3 nm	1.09 ps	[35]
WS_2	Direct deposit on fiber end face	15.1 %	157.6 MW/cm^2	1568.3 nm	1.94 nm	1.49 ps	[36]
WSe_2	Deposit on SPF	0.3 %	/	1556.7 nm	2 nm	1.31 ps	[35]
Graphene	PVA-composite	1.3 %	/	1559 nm	5.24 nm	464 fs	[37]
BP	Direct deposit on fiber end face	8.1 %	6.55 MW/cm^2	1571.5 nm	2.93 nm	946 fs	[32]
$PtSe_2$	Deposit on Mircofiber	1.11 – 4.90 %	340 –1230 MW/cm^2	1563 nm	6 nm	1.02 ps	[22]
PtS_2	PVA-composite	7 ± 0.3 %	9 ± 0.5 MW/cm^2	1572 ± 1 nm	2.47 ± 0.29 nm	2.064 ± 0.22 ps	This work
$PtTe_2$	Deposit on SPF	1.39 ± 0.1 %	400 ± 5 MW/cm^2	1560.6 ± 1.2 nm	4.4 ± 0.33 nm	1.66 ± 0.3 ps	This work

4.3 Passively mode-locked Erbium-doped fibre laser based on PtTe$_2$-SA

In the application of optical communication, infrared pulsed fibre laser is extensively utilised, in which a functional material possess with relative narrow bandgap is preferable for applying as SA and incorporating within the infrared fibre laser system [38]. Generally, group 6 TMDs have a relative broader bandgap, for instance, the bandgap energy of monolayer MoS$_2$ and WS$_2$ are 1.78 eV [38] and 2.1 eV [39], respectively. And thus the resonant absorption wavelength of group 6 TMDs is typically located in the visible range. Literature had suggested that the electronic structure of TMDs can be modulated by modifying the stoichiometric ratio of the material, where the introduction of lattice detects will result in the production of intermediate energy state located within the bandgap [38, 40] and hence assisting the light absorption in the infrared region. However, the precise control and quantification of the stoichiometric ratio are lengthy and complicated, which still tapered off the practicability of the wide bandgap TMDs-SA. Among the group 10 platinum-based TMDs, PtTe$_2$ demonstrates the smallest monolayer indirect bandgap of 0.4 eV (~3 µm optical wavelength) and also exhibits semi-metallic behaviour as from bilayer to bulk form [7]. This distinctive bandgap structure of PtTe$_2$ permit the direct electron excitation from the valence band to the conduction band and does not require the assistant of intermediate energy state, which suggests PtTe$_2$ is a potential broadband saturable absorber candidate.

4.3.1 PtTe$_2$-SA based mode-locked EDFL cavity setup

For the cavity setup of PtTe$_2$-SA based mode-locked EDFL, it is similar to that of the PtS$_2$-SA based system, and which several of modifications had processed to optimise the mode-locking performance. As shown in Fig. 4.10, the cavity was composed of a 0.7 meter long Erbium-doped single-mode fibre (LIEKKITM Er 110- 4/125), a 980nm/1550nm wavelength-division multiplexer (WDM), a 10 % output coupler, a polarisation-independent isolator, and a 3-paddle polarisation controller. The substitution of the in-line PC to a 3 paddle type is to provide sufficient freedom of polarisation manipulation within the cavity. The total cavity length is about 12.3 meters. Meanwhile, a new SA incorporation method was utilised where the exfoliated PtTe$_2$ nanosheets were coated onto the side-polished fibre.
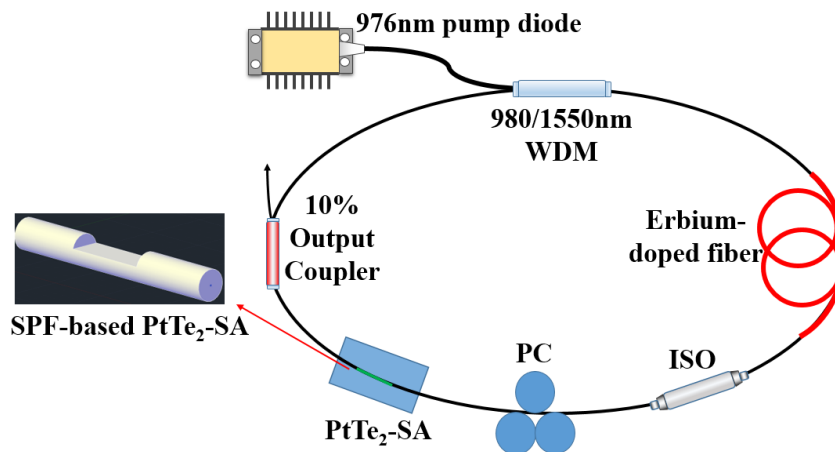
Fig 4.10 The schematic diagram of the PtTe$_2$-SA based EDFL cavity

4.3.2 The fabrication and characterisation of PtTe$_2$-SA

As same as the preparation method of PtS$_2$ nanosheets, liquid phase ultrasonic exfoliation was applied to sever the interlayer bonding of the bulk PtTe$_2$ sample. And an alternative exfoliation solvent, isopropanol (IPA), was used instead of NMP. Under prolonged observation (exceed three months) after the successful exfoliation, there was no any aggregation recorded and suggested that IPA can provide high diffusivity and high solvation power, which is comparable to NMP and also suitable for the liquid exfoliation of Pt-based TMDs. First, the PtTe$_2$ powder, which purchased from Six Carbon Inc., was mixed with IPA in 1 mg/ml ratio and followed by continuous probe sonication (SCIENTZ-1200E, Ningbo Scientz Biotechnology Co., Ltd.) for more than 20 hours. The temperature of the exfoliating solution was remaining at 20 °C to prohibit the degradation of the powder. The material qualities of the exfoliated PtTe$_2$ nanosheets were then characterized

The prepared PtTe$_2$ sample was first examined by using field emission transmission electron microscopy (FETEM - JEM-2100F). The TEM and HRTEM observation of a randomly selected nanosheet is shown in Fig. 4.11 (a). The lateral size of the PtTe$_2$ nanosheet are around 181.7 nm and 85.5nm as respective to long-axis and short-axis, respectively. The inter-plane distance measured from the HRTEM observation is about 0.29, which agree well with the crystalline structure of (011) plane of PtTe$_2$ [41]. Furthermore, as shown in Fig. 4.11 (b), the energy-dispersive X-ray spectroscopy (EDS) measurement (Tescan VEGA3) illustrates that no impurity was observed in the prepared PtTe$_2$ sample (The presented Si peak

is originated from the Silicon substrate holder for the EDS measurement). Then the sample was further characterised by applying Raman spectroscopy (LabRAM HR 8000- 488nm Argon ion laser light source). The Raman spectrum is shown in Fig. 4.11(c), where two major peaks are located at 108 cm^{-1} and 154.3 cm^{-1} with respect to the in-plane E_g vibration mode and out-of-plane A_{1g} vibration mode. The Raman data agree well with the result of previous literature (E_g: 109.05 cm^{-1}, A_{1g}: 154.74 cm^{-1} and layer thickness of 10.8 nm [42]), and suggests a successful exfoliation of the PtTe$_2$ sample.
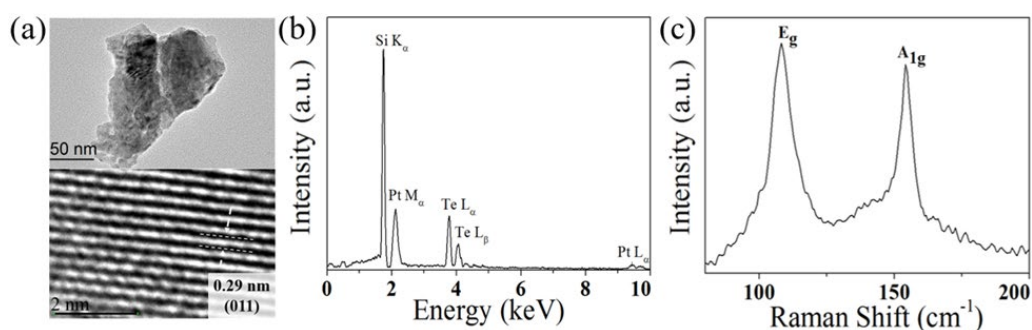
Fig 4.11 (a) The TEM and HRTEM observation a PtTe$_2$ nanosheet. (b) The energy-dispersive X-ray spectroscopy (EDS) and (c) Raman spectrum of the exfoliated PtTe$_2$ sample.

The morphology of the PtTe$_2$ nanosheets was also examined by applying atomic force microscopy (Bruker Nanoscope 8). Fig. 4.12 shows the statistical distribution of the layer thickness and lateral size(along with long- & short-axis) of the prepared PtTe$_2$ supernatant. The distribution was obtained by analysing 120 AFM data of exfoliated PtTe$_2$ nanosheets. The peaks of the lateral size distribution along long- and short-axis are located at 188 nm and 130 nm, respectively, which are coherent with the TEM observation result. Meanwhile, the most prevalently recorded layer thickness is about 16 nm.
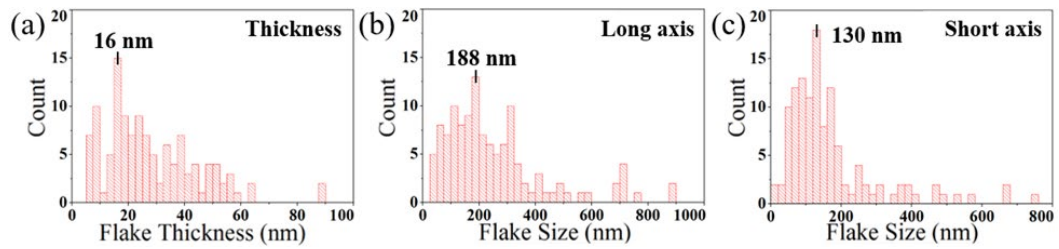
Fig 4.12 The statistical distribution of (a) layer thickness and lateral size along (b) long axis, and (c) short axis of the prepared PtTe$_2$ nanosheets.

Different from the PVA-based PtS$_2$-SA incorporation method, the introduction of PtTe$_2$ within the EDFL cavity was by depositing the prepared sample on side-polished fibre (SPF). The custom-made SPF was prepared by polishing one side of an SMF 28e single fibre. The polishing depth is around 1 μm above the fibre core and accompanying with a polishing width of 10 mm. The PtTe$_2$ nanosheets were coated on the SPF polished surface by evanescent-light guiding method, where a light source with a wavelength of 1566 nm and 20 mW CW average power was injected into the SPF before the immersion of the SPF in the prepared PtTe$_2$ supernatant. After the deposition, the nonlinear saturable absorption properties of this SPF based PtTe$_2$-SA was measured by the twin-balanced detector measurement system. The laser source of the measuring system possesses 2.09 ps pulse duration and 1560 nm centre wavelength. Equation 4.1 was utilised to fit the experimental data. Fig. 4.13 shows the measured nonlinear input intensity-dependent transmission curve of the prepared SPF-based PtTe$_2$-SA, where the estimated modulation depth and saturable intensity are 1.39 % and 400 MW/cm^2, respectively.
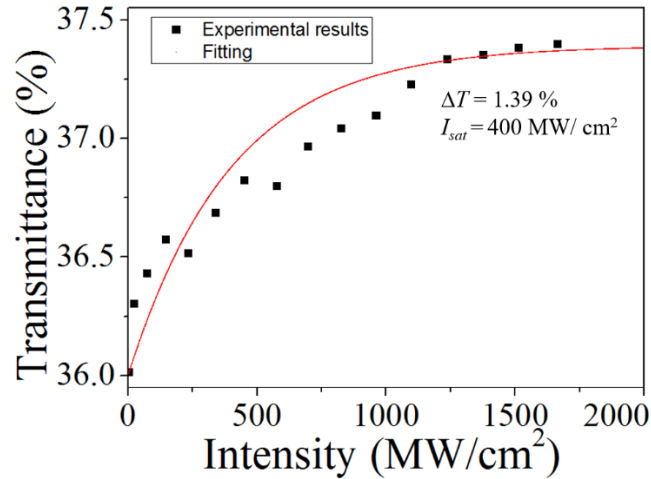
Fig. 4.13 The measured nonlinear saturable absorption of SPF-based PtTe$_2$-SA.

4.3.3 PtTe$_2$-SA based mode-locked EDFL laser performance and discussion

By connecting the SPF-based PtTe$_2$-SA into the ring cavity, the measured insertion loss and polarisation-dependent loss (PDL) of the PtTe$_2$-SA at 1.56 μm were ~ 9.7 dB and ~ 2.8 dB, respectively. Afterwards, by gradually scaling up the input pump power to the threshold value of 90 mW, a stable CW mode-locked pulses train was observed, as shown in Fig. 4.14 (a). The measured pulses interval time of 82.2 ns and corresponding repetition rate of 12.2 MHz are matched with the theoretical round trip cavity time and the cavity length (~12.3 m), which indicates the successful mode-locked operation. As shown in Fig. 4.14(b), the tunable range of the average output power is 0.073 mW to 0.499 mW under an input pump power range of 90 mW to 201.8 mW. As the input pump power scaled beyond 201.8 mW, the CW mode-locked output signal was restored to pure CW mode due to the over-saturation of the SA [32-33]. Fig. 4.14(c) shows the observed wavelength spectrum of the mode-locked signal, where the centre wavelength locates at 1560.6 nm with

a 3-dB bandwidth of 4.4 nn. The SNR value of 43 dB showed in the RF spectra (Fig. 4.14(d), in a span of 20 MHz with RBW of 40 kHz) also indicating that the CW mode-locked operation within the cavity possesses with high stability. Besides, the pulse duration of the mode-locked pulses was measured by using Autocorrelator (Femtochrome 103XL). Fig. 4.15 depicted that the autocorrelation trace can be well fitted by the hyperbolic secant function with a full width at half maximum (FWHM) value of 2.57 ps, which indicates the real pulse width of approximately 1.66 ps. Meanwhile, the calculated time-bandwidth product is 0.9 and suggests the pulse width can be further compressed (The minimum time-bandwidth product of $Sech^2$-shaped pulses: ~0.315).
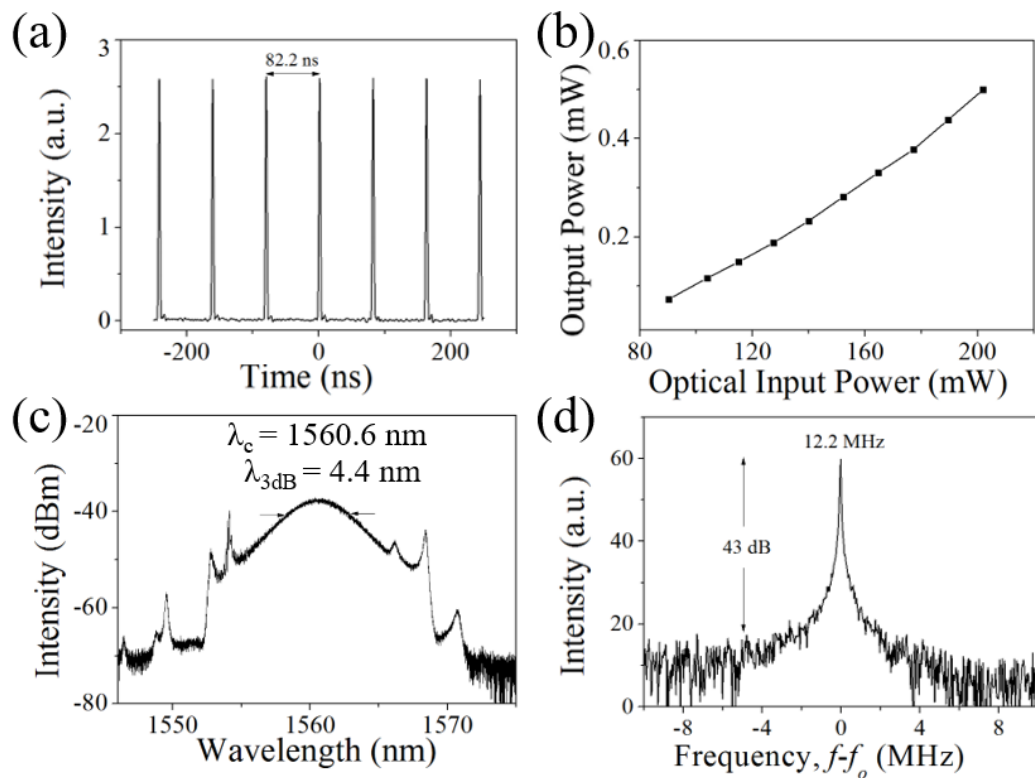
Fig. 4.14. SPF-based $PtTe_2$-SA mode-locked laser performance: (a) output pulse train. (b) The average output power varies with pump power. (c) wavelength and (d) radio frequency (RF) spectrum with respect to the maximum average output power of 0.499 mW.
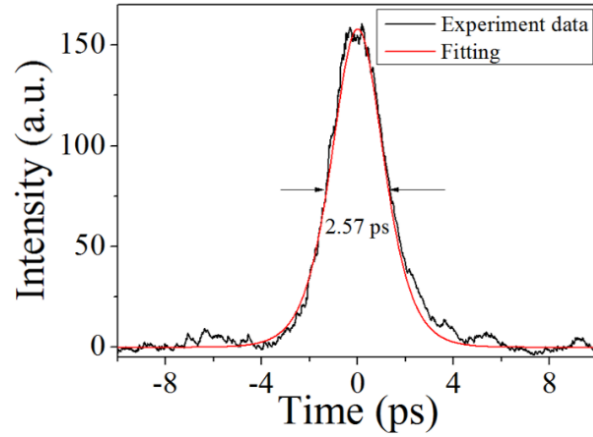
Fig. 4.15 The autocorrelation trace and Sech^2 fitting curve of the PtTe$_2$-SA based mode-locked EDFL output signal.

A greater modulation depth will enhance the pulse shaping effect of the saturable absorber, which leads to shorter pulse duration and reliable self-starting of the passively mode-locked operation[43]. However, it may also induce Q-switching instabilities, and hence the magnitude of the SA modulation depth need to be optimised precisely with respect to the laser dynamic parameters within the cavity, for instance, saturation energy of the gain medium [44]. To compare with PtS$_2$-SA, the modulation depth of the SPF-based PtTe$_2$-SA is relatively lower (PtTe$_2$-SA: 1.39%; PtS$_2$-SA: 7 %). The modulation depth of the SPF-based SA can be enhanced by increasing the deposition thickness of the PtTe$_2$ nanosheets on the SPF evanescent field region, in which the injected light power into the SPF can be further scaled up to elevate the light-guiding effect during the immersion of the SPF in the PtTe$_2$ supernatant. Besides, as refer to the work of Song $et. al.$[45], it showed that the Y component of the LP$_{01}$ mode of the propagating wave within SPF is broader than the X component, where a functional material (e.g. SWCNT) with anisotropic optical absorption will have the maximum absorption efficiency as if aligned along the direction of LP$_{01}$ Y-mode. Based on the experience of

sputtering deposition and post-annealing of TMDs, which discussed in chapter 3, one of our current works aims to study the anisotropic optical absorption properties of Pt-based TMDs by depositing the vertically aligned nanosheet onto the SPF. The modulation depth, as well as the mode-locking performance (e.g. pulse duration) of the growth direction-controlled TMDs-SAs, are expected to be improved due to a stronger nonlinear optical absorption.

As regard to Table 4.1, the measured saturable intensity of SPF-based or microfiber-based SAs (including $PtTe_2$-SA) are relatively higher as compared to another SAs which under alternative incorporation methods, such as polymer composite. Generally, the mode-locking threshold value of the 976 nm input pump power is promoted for triggering the nonlinear optical absorption of the SPF-based SA. But since only the evanescent field of the propagating wave will interact with the SA material, and thus the thermal-induced damage problem within SA was still prohibited. Different from the PVA-based PtS_2-SA, there is no any degradation recorded under the prolonged operation of the SPF-based $PtTe_2$-SA, which proved the superior competitiveness of evanescent-field interaction-based (SPF or microfiber) saturable absorber.

For the mode-locked EDFL performances based on either PtS_2 and $PtTe_2$-SA, the achieved pulse duration in both cavities are comparable to other low-dimensional materials based saturable absorber as shown in Table 4.1, and hence indicates the air-stable group 10 TMDs possess the potential and promising ability to act as the structural material for next-generation SA. The demonstrations of the mode-locked EDFLs are just the preliminary study work, and it needs a in-depth

investigation of the laser system applicability and optical nonlinearity of the novel group 10 TMDs, which is part of the outlooks of our research work.
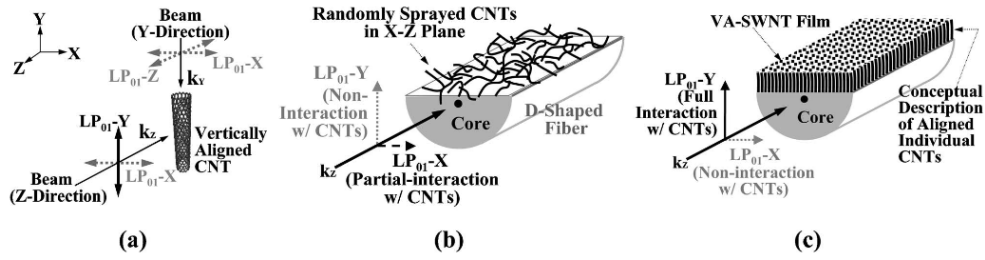
Fig. 4.16 (a) Schematic diagram showing the anisotropic light absorption from the single-walled carbon nanotube (SWCNT). (b) The deposition of SWCNT on side-polished fibre under (b) randomly and (c) vertically aligned manner [45].

4.4 Chapter summary

In this chapter, both PtS_2-SA and $PtTe_2$-SA based passively mode-locked EDFLs are experimentally demonstrated. Two separate synthesis methods were applied to fabricate the SAs. For the PtS_2-SA, the ultrasonic exfoliated PtS_2 nanosheets were incorporated within polyvinyl alcohol (PVA) polymer to form a matrix composite thin film and followed by sandwiching between two FC/APC fibre connectors. And for the $PtTe_2$-SA, the ultrasonic exfoliated $PtTe_2$ nanosheets were deposited onto the evanescent-field region of a side-polished single-mode fibre. The achieved pulse duration of the mode-locked EDFLs are 2.064 ps and 1.66ps with respect to the PtS_2-SA and $PtTe_2$-SA, respectively, which is comparable to other low dimensional materials-based result. And indicates that both of the platinum-based TMDs can act as a promising nonlinear saturable absorber. To the best of our knowledge, the demonstrations of these mode-locked EDFLs based on PtS_2 and $PtTe_2$-SA are still a pioneer study within the nonlinear photonic field.

4.5 References

1. T. Matniyaz, "Free-space NPR mode locked erbrium doped fiber laser based frequency comb for optical frequency measurement," arXiv preprint arXiv:1802.10183(2018).
2. F. Ö. Ilday, J. Buckley, L. Kuznetsova, and F. W. Wise, "Generation of 36-femtosecond pulses from a ytterbium fiber laser," Opt. Exp. 11(26), 3550-3554(2003).
3. A. Chong, H. Liu, B. Nie, B. G. Bale, S. Wabnitz, W. H. Renninger, and F. W. Wise, " Pulse generation without gain-bandwidth limitation in a laser with self-similar evolution," Opt. Exp. 20(13), 14213-14220(2012).
4. C. Y. Tang, Y. Chai, H. Long, L. Tao, L. H. Zeng, Y. H. Tsang, and X. Lin, "High-power passively mode-locked Nd: YVO_4 laser using SWCNT saturable absorber fabricated by dip-coating method," Opt. Express. 23, 4880-4886 (2015).
5. K. Wu, B. Chen, X. Zhang, S. Zhang, C. Guo, Chao, Li, P. Xiao, J. Wang, L. Zhou, W. Zou, and J.Chen, "High-performance mode-locked and Q-switched fiber lasers based on novel 2D materials of topological insulators, transition metal dichalcogenides and black phosphorus: review and perspective," Opt. Comm. 406, 214-229 (2018).
6. G. Sobon, J. Sotor, I. Pasternak, K. Grodecki, P. Paletko, W. Strupinski, and K. M. Abramski, "Er-doped fiber laser mode-locked by CVD-graphene saturable absorber," J. Lightwave Techno. 30(17), 2770-2775(2012).
7. R. A. B. Villaos, C. P. Crisostomo, Z. Q. Huang, S. M. Huang, A. A. B. Padama, M. A. Albao, and F. C. Chuang, "Thickness dependent electronic properties of Pt dichalcogenides," npj 2D Mat. Appl., 3(1), 2(2019).
8. S. Liu, and Z. Liu, "Hybridization induced metallic and magnetic edge states in noble transition-metal-dichalcogenides of PtX_2 (X= S, Se) nanoribbons," Physical Chemistry Chemical Physics, 20(33), 21441-21446(2018).
9. Y. Zhao, J. Qiao, Z. Yu, P. Yu, K. Xu, S. P. Lau, and Y. Chai, "High-electron-mobility and air-stable 2D layered $PtSe_2$ FETs," Adv. Mat. 29(5), 1604230(2017).
10. K., ARNE, and F. GRQNVOLD, "High Temperature X-Ray Study of the Thermal Expansion of PtS_2, $PtSe_2$, $PtTe_2$, and $PdTe_2$," Acta Chemica Scandinavica 13.9, 1767-1774(1959).
11. Y. Wang, et al. "Monolayer $PtSe_2$, a new semiconducting transition-metal-dichal-cogenide, epitaxially grown by direct selenization of Pt," Nano Lett.15, 4013–4018(2015).
12. X. Chia, et al. "Layered platinum dichalcogenides (PtS_2, $PtSe_2$, and $PtTe_2$) electrocatalysis: monotonic dependence on the chalcogen size," Adv. Funct. Mater.26,4306–4318 (2016).
13. P. Lejing, et al. "Temperature dependence of Raman responses of few-layer PtS_2," Nanotechnology 29.50 (2018): 505709.
14. A. Politano, G. Chiarello, C. N. Kuo, C. S. Lue, R. Edla, P.Torelli, and D. W. Boukhvalov,. "Tailoring the Surface Chemical Reactivity of Transition-Metal Dichalcogenide PtTe2 Crystals," Adv. Funct.l Mat. 28(15), 1706504(2018).
15. Y. Cao, X. Tian, J. Gu, B. Liu, B. Zhang, S. Song, F. Fan, and Y. Chen, "Covalent Functionalization of Black Phosphorus with Conjugated Polymer for Information Storage," Angew. 57(17), 4543-4548 (2018).
16. C. J. Zhang, O. Pinilla, N. McEvoy, C. P. Cullen, B. Anasori, E. Long, S. H. Park, A. S. Ascaso, A. Shmeliov, D. Krishnan, C. Morant, X. Liu, G. S. Duesberg, Y. Gogotsi, and V. Nicolosi, "Oxidation Stability of Colloidal Two-Dimensional Titanium Carbides (MXenes)," Chem. Mater. 29, 4848-4856 (2017).
17. A. Lipatov, M. Alhabeb, M. R. Lukatskaya, A. Boson, Y. Gogotsi, and A. Sinitskii, "Effect of Synthesis on Quality, Electronic Properties and Environmental Stability of Individual Monolayer Ti3C2 MXene Flakes," Adv. Electron. Mater 2, 1600255 (2016).
18. J. Koo, Y. I. Jhon, J. Park, J. Lee, Y. M. Jhon, and J. H. Lee, "Near-Infrared Saturable Absorption of Defective Bulk-Structured WTe2 for Femtosecond Laser Mode-Locking," Adv. Funct. Mater. 26 ,7454-7461 (2016).
19. C. H. Lee, E. C. Silva, L. Calderin, M. A. T. Nguyen, M. J. Hollander, B. Bersch, T. E. Mallouk, and J. A. Robinson, "Tungsten Ditelluride: a layered semimetal," Sci. Rep. 5, 10013 (2015).
20. L. Tao, X. Huang, J. He, Y. Lou, L. Zeng, Y. Li, H. Long, J. Li, L. Zhang, and Y. H. Tsang, "Vertically standing $PtSe_2$ film: a saturable absorber for a passively mode-locked Nd:LuVO4 laser," Photonics Res. 6(7), 750-755 (2018).
21. Z. Li, R. Li, C. Pang, N. Dong, J. Wang, H. Yu, and F. Chen, "8.8 GHz Q-switched mode-locked waveguide lasers modulated by $PtSe_2$ saturable absorber," Opt. Express 27(6), 8727-8737 (2019).
22. K. Zhang, M. Feng, Y. Ren, F. Liu, X. Chen, J. Yang, X. Q. Yan, F. Song, and J. Tian, "Q-switched and mode-locked Er-doped fiber laser using $PtSe_2$ as a saturable absorber," Photonics Res. 6(9), 893-899 (2018).
23. B. Huang, L. Du, Q. Yi, L. Yang, J. Li, L. Miao, C. Zhao, and S. Wen, "Bulk-structured $PtSe_2$ for femtosecond fiber laser mode-locking," Opt. Express 27(3), 2604-2611 (2019).
24. W. Zhang, Z. Huang, W. Zhang, and Y. Li, "Two-dimensional semiconductors with possible high room temperature mobility," Nano Research, 7(12), 1731-1737(2014).
25. P. Miró, M. Ghorbani-Asl, and T. Heine, " Two dimensional materials beyond MoS_2: noble-transition-metal dichalcogenides," Angewandte Chemie International Edition, 53(11), 3015-3018(2014).
26. J. Qiao, X. Kong, Z. X. Hu, F. Yang, and W. Ji, "High-mobility transport anisotropy and linear dichroism in few-layer black phosphorus," Nat. Commun. 5, 4475(2014).
27. O. L. Sanchez, D. Lembke, M. Kayci, A. Radenovic, and A. Kis, "Ultrasensitive photodetectors based on monolayer MoS_2," Nat. nanotechno. 8, 497(2013).
28. S. Ma, L. Zeng, L. Tao, C. Y. Tang, H. Yuan, H. Long and X. Zhang, "Enhanced Photocatalytic Activity of WS_2 Film by Laser Drilling to Produce Porous WS_2/WO_3 Heterostructure," Sci. Rep. 7, 3125(2017).
29. L. Li, W. Wang, Y. Chai, H. Li, M. Tian, and T. Zhai, "Few Layered PtS_2 Phototransistor on h-BN with High Gain," Adv. Funct. Mater. 27, 1701011(2017).
30. Yuanet al., "Wafer-scale fabrication of 2D Van der Waals heterojunc-tions for efficient and broadband photo-detection," Mesoscale NanoscalePhys.,arXiv:1803.04695, 2018
31. Y. I. Jhon, J. Koo, B. AnasoriSeo, M. Seo, J. H. Lee, Y. Gogotsi and Y. M. Jhon, "Metallic MXene Saturable Absorber for Femtosecond Mode-Locked Lasers," Adv. Mater. 29, 17024962017.

32. Y. Chen, G. Jiang, S. Chen, Z. Guo, X. Yu, C. Zhao, H. Zhang, Q. Bao, S. Wen, D. Tang and D. Fan, "Mechanically exfoliated black phosphorus as a new saturable absorber for both Q-switching and Mode-locking laser operation", Opt. Express, 2015, 23, 12823-12833.

33. P. P. Kiran, D. R. Reddy, B. G. Maiya, A. K. Dharmadhikari, G. R. Kumar and D. N. Rao, "Nonlinear absorption properties of axial-bonding type tin(IV) tetratolyporphyrin based hybrid porphyrin arrays", Opt. Commun. 252, 150-161(2005).

34. H. Xia, H. Li, C. Lan, C. Li, X. Zhang, S. Zhang, and Y. Liu, "Ultrafast erbium-doped fiber laser mode-locked by a CVD-grown molybdenum disulfide (MoS_2) saturable absorber," Opt. Express 22(14), 17341-17348 (2014).

35. D. Mao, X. She, B. Du, D. Yang, W. Zhang, K. Song, X. Cui, B. Jiang, T. Peng, and J. Zhao, "Erbium-doped fiber laser passively mode locked with few-layer $WSe_2/MoSe_2$ nanosheets," Sci. Rep. 6, 23583 (2016).

36. P. Yan, H. Chen, J. Yin, Z. Xu, J. Li, Z. Jiang, W. Zhang, J. Wang, I. L. Li, Z. Sun, and S. Ruan, "Large-area tungsten disulfide for ultrafast photonics," Nanoscale 9, 1871-1877 (2017).

37. Z. Sun, T. Hasan, F. Torrisi, D. Popa, G. Privitera, F. Q. Wang, F. Bonaccorso, D. M. Basko, and A. C. Ferrari, "Graphene mode-locked ultrafast laser," ACS Nano 4, 803–810 (2010).

38. J. Yuan et al, "Few-Layer Platinum Diselenide as a New Saturable Absorber for Ultrafast Fiber Lasers," ACS Appl. Mater. Interfaces 10,21534-21540, (2018).

39. Long, H. et al. "Tuning nonlinear optical absorption properties of WS_2 nanosheets," Nanoscale 7, 17771-17777, (2015).

40. S. X. Wang, H. H. Yu, H. J. Zhang, A. Z. Wang, M. W. Zhao, Y. X. Chen, L. M. Mei, and J. Y. Wang, "Broadband few-layer MoS2saturable absorbers," Adv. Mater., 263538–44(2014).

41. N. F. Rosli, C. C. M. Martinez, N. M. Latiff, N. Rohaizad, Z. Sofer, A. C. Fisher, and M. Pumera, "Layered $PtTe_2$ Matches Electrocatalytic Performance of Pt/C for Oxygen Reduction Reaction with Significantly Lower Toxicity," ACS Sustainable Chem. Eng. 6, 7432-7441 (2018).

42. H. Ma, P. Chen, Peng B. Li, J. Li, R. Ai, Z. Zhang, G. Sun, K. Yao, Z. Lin, B. Zhao, R. Wu, X. Tang, X. Duan, and X. Duan, "Thickness-tunable synthesis of ultrathin type-II Dirac semimetal $PtTe_2$ single crystals and Their Thickness-Dependent Electronic Properties," Nano Lett. 18, 3523–3529 (2018).

43. W. Liu, L. Pang, H. Han, M. Liu, M. Lei, S. Fang, and Z.Wei, "Tungsten disulfide saturable absorbers for 67 fs mode-locked erbium-doped fiber lasers," Opti. Exp. 25(3), 2950-2959(2017).

44. C. Hönninger et al., "Q-switching stability limits of cw passive mode locking", J. Opt. Soc. Am. B 16 (1), 46 (1999).

45. Y. W. Song, S. Yamashita, E. Einarsson, and S. Maruyama, "All-fiber pulsed lasers passively mode locked by transferable vertically aligned carbon nanotube film," Opt. Lett. 32(11), 1399-1401 (2007).

CHAPTER 5
Size-Dependent Nonlinear Optical Properties of Atomically Thin PtS$_2$ nanosheet

To control the nonlinear optical (NLO) properties of functional materials and further apply to synthesise practical photonic device by cost-saving and straightforward manner is a sustained and attractive topic among the research community. The NLO properties of the novel material can be extensively applied to different fields, for instance, compact optical switcher, ultrashort laser pulses generation (saturable absorber), optical limiter for protecting the components within the optical communication system, even biomedical sensors. In this chapter, the dependence of NLO properties on the layer thickness and lateral size of the platinum disulfide PtS$_2$ is experimentally demonstrated. As a pioneer study on the nonlinear optical absorption (NOA) features of group 10 TMDs, the Z-scan results show that the NOA response of PtS$_2$ depends significantly on the lateral size and layer thickness of the nanosheets, where a transition of NOA behaviour from reserve saturable absorption to saturable absorption is demonstrated.

5.1 Background and motivation

Different from layered mono-element materials, for instance, graphene and black phosphorus (BP), the material properties and crystalline structure of 2D transition metal dichalcogenides (TMDs) depend heavily on the d-electron configuration of the transition metal. The intralayer bonding, energy bandgap structure, lattice

vibration [1], as well as the macroscopic properties (e.g. electrical conductivity[2], and optical absorption behaviors [3-4]) of the TMDs will be influenced by the d-electron number of transition metal. Meanwhile, literature had reported the modification of bandgap and nonlinear optical response of TMDs by modulating the morphological characteristics of the materials [4-5], in which significant nonlinear optical properties, such as optical limiting is able to be promoted by reducing the average lateral size and layer thickness of the TMDs (e.g. WS_2 [4, 6]). Noticeably, it had also been shown that the ultrashort laser pulses generation can be achieved by utilizing 2D TMDs with subsided nanosheets lateral size and layer thickness [7-10]. The availability of manipulating the optical nonlinearity of novel TMDs material is an essential foundation for the development of advanced laser systems as it provides the strategy for optimisation of different TMDs-SA-based pulsed laser systems with respect to extensive operation wavelength range. Undoubtedly, the maturation of NLO properties engineering on 2D TMDs can induce great impact on various application fields, from energy harvesting [11-12], photodetectors [13-14] to optical modulators for optical communication [15].

In the previous chapter, it had been demonstrated that Pt-based TMDs possess superior nonlinear saturable absorption property. And it is worth to has a further investigation on the influence of material morphological features on the NOA response of Pt-TMDs, in which a Z-scan measurement was conducted on several PtS_2 samples with different nanosheet lateral size and thickness and the results will be discussed as follow.

5.2 Setup of the Z-scan measuring system and sample preparation

As shown in Fig. 5.1, a standard open-aperture Z-scan system was constructed to test the NOA properties of PtS_2 samples. An Nd: YAG Q-switched laser was utilised as the excitation light source, where the operation wavelength, pulse duration and repetition rate of the laser are 532nm, 8 ns and 10Hz, respectively. Meanwhile, a fixed single pulse energy value of 670 µJ was selected for triggering the NLO response of the samples. In the setup, the laser beam was split into two paths by the 50:50 beam splitter, where one of the beams will be incident on the pyroelectric energy meter D1 to monitor the operating state of the laser source. And the second laser beam will be focused by the Plano-Convex Lens with a focal length of 50 mm. The PtS_2 samples were presented as a liquid form during the Z-scan test, where the prepared PtS_2-NMP suspensions were filled into a quartz cuvette with 1 mm optical path and mobilised along the Z-optical path of the focused laser beam. Pyroelectric energy meter D2 was used to record the transmittance change of the samples according to different incident light intensity. Noticeably, to avoid heat accumulation and consequent micro-bubble formation within the suspension, an electrical shutter was installed in the system to modulate the laser pulse incident frequency on the cuvette as 1Hz. Otherwise, the thermal-induced micro-bubble will generate extra optical loss and thus interfere with the result of the Z-scan measurement.
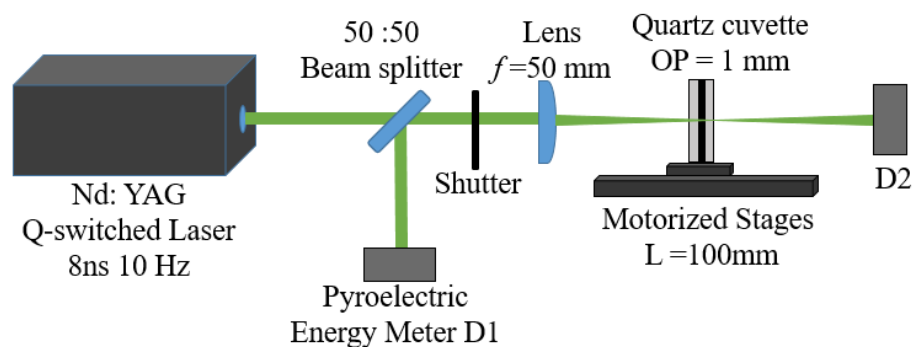
Fig. 5.1 The schematic diagram of the open aperture Z-scan measurement setup(D: Detector; L: operational length; f: focal length; OP: optical path).

To obtain PtS$_2$ samples with the different distributions of lateral size and thickness, a modulation of centrifugal force was applied in the centrifugation process. The utilised PtS$_2$-NMP exfoliated suspension is identical to that used in chapter 4, and hence the material characterisation data can refer to the section 4.2.2. After successful ultrasonic exfoliation, the PtS$_2$-NMP suspension was individually centrifuged at different angular velocities for 30 minutes, where the value of the speeds are 9000, 7000, 5000, and 3000 rpm, corresponding to relative centrifugal force (RCF) of 9072, 5488, 2800 and 1008 g, respectively. The supernatants were extracted in each individual centrifugations and named as S3000, S5000, S7000, and S9000, respectively (S- Centrifugation speed (rpm)). The lateral size and thickness distribution of different centrifugated PtS$_2$ samples were measured by using atomic force microscope (AFM-Asylum MFP-3D Infinity) in tapping mode. Fig 5.2 illustrated the measured average values in different PtS$_2$ samples, which the statistical measurement is achieved by analysing exceed 60 recorded AFM data. Both the lateral size and layer thickness of PtS$_2$ nanosheets decreased as the centrifugation speed scaled up. The average nanosheets lateral size decreased from around 565 nm of S3000 (RCF: 1008 g) to 110 nm of the S9000 sample (RCF:

9072 g), and which the corresponding layer thickness subsided from 30 nm to 10 nm. It shows that the average nanosheet size and layer thickness of sample S9000 is about one-third of that of sample S3000.
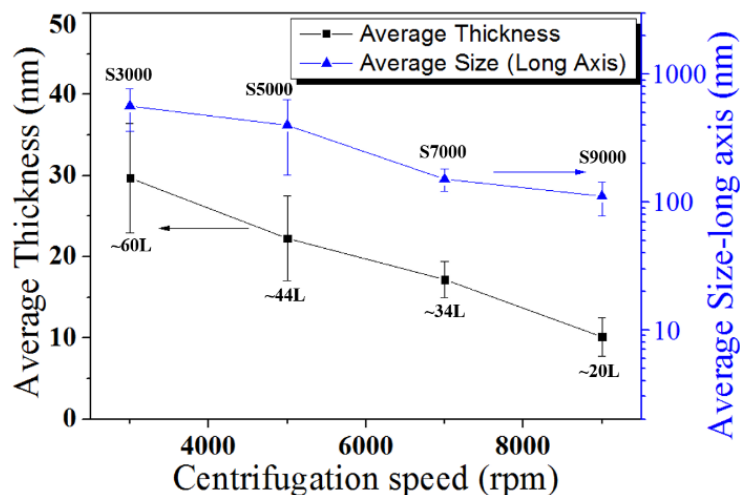
Fig. 5.2 The measured average lateral size and thickness of different centrifugated PtS_2 samples vary with centrifugation speed.

5.3 The result of Z-scan measurement and discussion

After the individual centrifugations, the concentrations of each sample were modified, in which the initial transmission ratio of all PtS_2 samples were set to be 67% to confirm fair comparison. The measured NOA responses of four PtS_2 centrifugated samples and the control data were shown in Fig. 5.3. Pure NMP solvent was utilised as the control data set, in which there was none of the observable NOA response recorded from the control set and proved that all the measured NOA responses were originated from the exfoliated PtS_2 nanosheet solely. From Fig. 5.3(a) and 5.3(b), it shows that except for S9000, all other PtS_2 samples exhibited reverse saturable absorption (RSA) response, which the normalised transmittances of the materials were reduced as the input intensity

raised up and is also well-known as optical limiting. The RSA response of the PtS$_2$ samples became weaker as the nanosheet lateral size, and layer thickness subsided, where the tunable normalised transmittance range of sample S7000 (1 to 0.74) is about half of that of sample S3000 (1 to 0.42). Meanwhile, the NOA starting thresholds (F_s), defined as the input fluence value where the normalised transmittance starts to diverge from linearity, had increased from 0.023 J/cm^2 of sample S3000 to 0.043 J/cm^2 of sample S7000, indicating that the RSA response of sample S3000 is stronger than that of sample S7000. Furthermore, the nonlinear absorption coefficients β were calculated by fitting the experimental data with the nonlinear propagation equation [16],

$$\mathrm{d}I/\mathrm{d}z = - (\alpha_0 I + \beta I^2) \qquad (\text{Eq. 5.1})$$

where α_0 and I represent the linear absorption coefficient and the laser beam irradiance onto the samples, respectively. As shown in Table 5.1, the β value reduced from 1.113 cm/GW of sample S3000 to 0.28 cm/GW of sample S7000, also suggests a weakening of RSA response as the nanosheets size and thickness dropped.
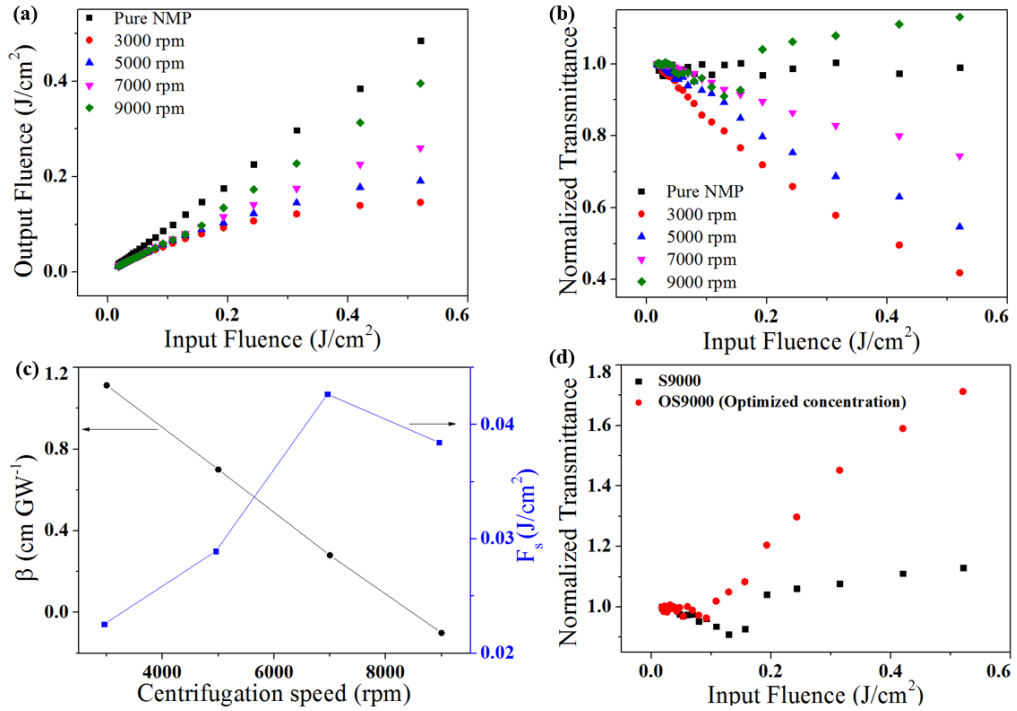
Fig. 5.3 The Z-scan result of PtS$_2$ samples with different nanosheets size and layer thickness distributions at 532 nm wavelength. (a) The output fluence and (b) the normalised transmittance vary with Input fluence. (c) The variation of Nonlinear absorption coefficient (β), NOA starting threshold (F$_S$), on centrifugation speed. (d) The normalised transmittance of S9000 and the OS9000 (OS9000: PtS$_2$ centrifuged sample with optimised concentration) vary with Input fluence at 532 nm.

Table 5.1 The nonlinear optical parameters, including of NOA starting thresholds (F_S), optical limiting thresholds (F_{OL}), Nonlinear absorption coefficient (β) and normalised transmittance at peak input fluence (focus, 0.52 J/cm^2), for different centrifugated samples.

PtS$_2$ samples	Average Thickness (nm)	Average Size (Long Axis) (nm)	NLO response	F_s (J/cm^2)	F_{OL} (J/cm^2)	β (cm/GW)	Normalised Transmittance at peak Input fluence
S3000	29.7	565	RSA	0.023	0.42	1.113 ±0.12	0.42
S5000	22.3	399	RSA	0.029	/	0.7 ±0.11	0.55
S7000	17.2	151	RSA	0.043	/	0.28 ±0.03	0.74
S9000	10.2	110	SA	0.038	/	-0.1 ±0.02	1.13
OS9000	10.2	110	SA	0.049	/	-0.34 ±0.04	1.71

Remarkably, the sample S9000 exhibited a distinctive NOA behaviour, where an RSA response was presented in the input fluence range of 0.018 J/cm^2 to 0.13 J/cm^{2,} and the RSA behaviour was switched to saturable absorption (SA) as the input fluence scaled beyond 0.13 J/cm^2. As shown in Fig. 5.3(b), the normalised transmittance of sample S9000 was gradually rising as the input fluence elevated

92

from 0.13 J/cm^2 to 0.52 J/cm^2. This switch of optical response from RSA to SA had been demonstrated in other nonlinear materials [17-19]. In the situation of low input fluence providing to the nonlinear materials, the photon absorption is dominantly based on the group state excitation, and hence only linear absorption behaviour is observed. However, the electron population density of the first excited state will be dramatically increased because of high-intensity irradiation onto the nonlinear materials and consequently, electron excitation. As a result, the photon absorption from the first excited state to a higher energy level will be enhanced and eventually induce a significant contribution to the overall optical absorbance. This effect is well-known as excited-state absorption (ESA). The extra absorbance caused by the ESA effect will make the overall transmittance decreased under the situation of high-intensity irradiation onto the materials, which lead to RSA behaviour [5]. Nevertheless, if the input fluence further scaled up, the available excitation electrons are depleted, and hence the ESA effect will be saturated. It leads to a drop in the overall absorbance of the materials and causes the RSA behaviour switch to SA, as demonstrated within the sample S9000 [17].

For the observation of RSA response weakening from sample S3000 to S7000, the trend is different from the previous result of the NOA study on WS$_2$ [4], where the optical limiting behaviours of the WS$_2$ samples were promoted as the nanosheets lateral dimension, and layer thickness decreased. And it can be explained by utilising free-carrier absorption (FCA) model which proposed by Boggess et al. [20]. The model suggested that the photon-induced electron excitation within the nonlinear materials can be contributed by both excited-state absorption and two-photon absorption (TPA) effect simultaneously. As shown in

Fig. 5.4, if the layer thickness of the TMDs reduced, the expanded bandgap of the materials will facilitate the TPA effect, which may promote electron population density of the first excited state, as well as the RSA response [4]. Meanwhile, the drop of lateral dimension will generate more active edge site on the TMDs nanosheet, and eventually induced numerous localised edge energy states located near the Fermi-level in the bandgap. These edge energy states may also promote the RSA response [5, 21-22]. In this work, for the NOA response of PtS_2 sample S3000, it is already close to the RSA saturation limit, in which a further promotion of photon absorption by reducing the nanosheets size and thickness will lead to the depletion of available excitation electron and thus weakening of the RSA response. It may also use a four energy model as shown in Fig 5.5 to explain the switch of nonlinear optical response. The energy model composed of four energy levels, L_1, L_2, L_3, L_4, with corresponding population densities N_1, N_2, N_3, and N_4. The population N_4 is typically negligible as the lifetime of L_4 is tend to be 0. σ_{ij} stands for the absorption cross-section of different energy-level transition. At low incident fluence, excitation from ground state L_1 to first excited state L_2 is dominated, where linear absorption is solely be demonstrated. Nevertheless, as the input fluence scaled-up, the magnitude of N_2 and N_3 were enhanced. Thus, the upper-state excitation becomes significant and greatly contribute to the overall photon absorption. This phenomenon is known as excited-state absorption (ESA). For the result of the S9000 PtS_2 sample, the initial RSA performance is due to the unsaturation of the second excited state L_3. But at strong input fluence, the absorption cross-sections will become $\sigma_{12} < \sigma_{23} > \sigma_{34}$. The accumulation of N_3 population will prohibit further photon absorption by depleting the number of

94

available electrons in L_1 and L_2. Thus it causes a drop in the corresponding absorption coefficient, as well as the overall ESA and RSA response (known as bleaching). As a result, the NOA response will be switched to saturable absorption (SA), as shown in Fig. 5.3 (b) .

Besides of the NOA dependence on the nanosheets size and thickness, the concentration of the nonlinear materials or light-matter interaction length also interfere with the NOA response of the material system. One of the examples is the interaction length (evanescent field) of the saturable absorber material coated side-polished fibre will affect to the modulation depth of the absorber [23]. As shown in Fig. 5.3(d), a further modification of the PtS_2 nanosheets concentration in sample S9000 was processed where concentration optimised sample OS9000 had shown an improved saturable absorption response (The concentration of PtS_2 nanosheets in OS9000 is 35 % higher than that of sample S9000). The sample OS9000 has an initial transmission ratio of 49 %, which is lower than that of S3000 to S9000 samples (67 %). Remarkably, the maximum achieved normalised transmittance of OS 9000 had improved to a value of 1.71 and is way beyond of sample S9000 (1.13). This NOA response dependence on material concentration has been demonstrated in different function materials previously, including graphene oxide [24] and TMDs-WS_2[25].
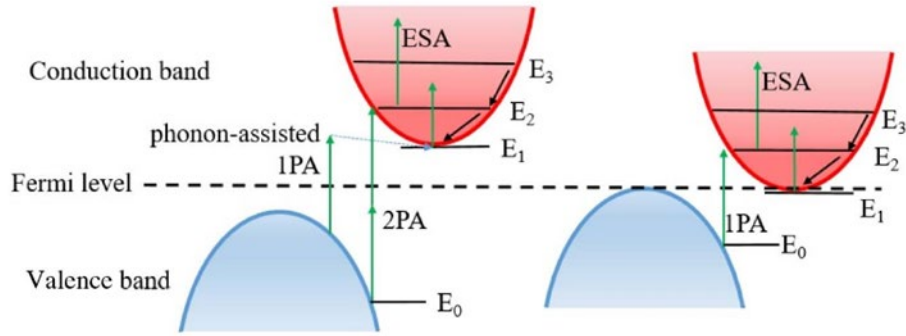
Fig. 5.4 Schematic diagram illustrating the photon absorption process within a four-energy level model, where the E_0, E_1, E_2, and E_3 are the ground state, first, second, and third excited state, respectively. 1PA and 2PA represent the single-photon absorption and two-photon absorption, respectively. ESA stands for the excited-state absorption[26].
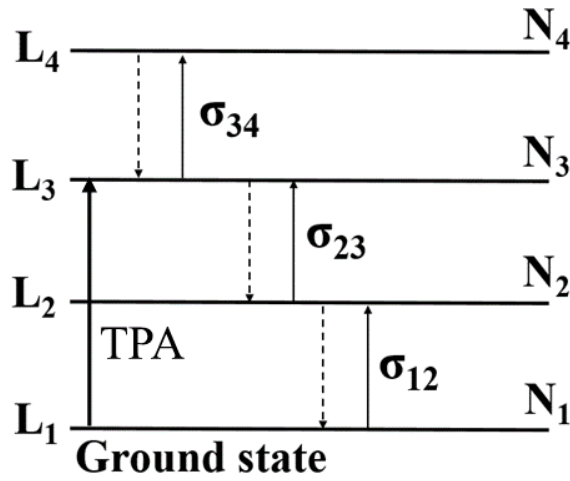
Fig. 5.5 Four energy level electronic transition model.

As a pioneer work for studying the NLO properties of group 10 TMDs material, there are several follow-up works can be applied to enrich the understanding of the NOA behaviors of Pt/Pd based TMDs, one example is to investigate the NOA response of the nonlinear material in picosecond or femtosecond interaction time regime and process a comparison with the result in nanosecond regime. Previous liteture had reported the pulse duration-dependent NOA response of the nonlinear TMDs material [25] and suggested that the interband exciton decay lifetime and intraband relaxation life-time of the nonlinear materials have a significant influence on the NOA response of the material, which a pump-probe measurement

should process to quantify the corresponding decay parameters. Second, it is worth to expend the NOA study among the Pt/Pd TMDs group, where it had been demonstrated that both $PtSe_2$ and $PtTe_2$ also possess with superior nonlinear saturable absorption property and able to induce ultrafast laser pulses, even one of our preliminary works had shown that the PdS_2 and $PdSe_2$ also possess SA behaviour as well.

5.4 Chapter summary

To the best of our knowledge, this is the first demonstration of modulating the NOA response of Pt-based TMD by controlling the morphological features of the nonlinear material. In the experiment, four PtS_2 samples with different distributions of nanosheets lateral dimension and layer thickness were prepared by using individual centrifugation method with distinct centrifugal forces. The samples are named as S3000, S5000, S7000, S9000, corresponding to the centrifugal speed of 3000 rpm (Relative Centrifugal Force RCF:1008 g), 5000 rpm (RCF:2800 g), 7000 rpm (RCF: 5488 g), and 9000 rpm (RCF: 9072 g), respectively. The AFM measurement shows that the average nanosheet lateral size and layer thickness dropped from around 565 nm to 110 nm, and 30 nm to 10 nm, respectively according to the samples from S3000 to S9000. By the Z-scan test, it shows that as the material nanosheets size and thickness reduced, it will enhance the excited state photon absorption (ESA) effect and two-photon absorption (TPA) effect, which promotes the reverse saturable absorption (RSA) response of the PtS_2 samples. As the sample S3000 is already close to the saturation limit of the RSA

response, further enhancement of photon absorption is resulting in a weakening of the RSA response, eventually induced a change of the nonlinear optical absorption behaviour from RSA of sample S3000 to saturable absorption (SA) of sample S9000.

5.5 References

1. Y. Zhao, J. Qiao, P. Yu, Z. Hu, Z. Lin, S. P. Lau, Z. Liu, W. Ji, Y. Chai, "Strong Interlayer Interaction in 2D Layered PtS$_2$," Adv. Mater. 28, 2399-2407(2016).
2. Q. H. Wang, K. K. Zadeh, A. Kis, J. N. Coleman, M. S. Strano, "Electronics and optoelectronics of two-dimensional transition metal dichalcogenides," Nat. Nanotechno. 7 699–712(2012).
3. K. F. Mak, C. Lee, J. Hone, J. Shan, T. F. Heinz, "Atomically Thin MoS2: A New Direct-Gap Semiconductor," Phys. Rev. Lett. 105, 136805(2010).
4. H. Long, L. Tao, C. Y. Tang, B. Zhou, Y. Zhao, L. Zeng, S. F. Yu, S. P. Lau, Y. Chai, Y. H. Tsang, "Tuning nonlinear optical absorption properties of WS2 nanosheets," Nanoscale 7, 17771-17777(2015).
5. K.G. Zhou, M. Zhao, M. J. Chang, Q. Wang, X. Z. Wu, Y.   Song, H. L. Zhang, "Size Dependent Nonlinear Optical Properties of Atomically Thin Transition Metal Dichalcogenide Nanosheets," Small. 11, 694-701(2015).
6. H. Long, L. Tao, C. P. Chiu, C. Y. Tang, K. H. Fung, Y. Chai, Y. H. Tsang, "The WS2 quantum dot: preparation, characterization and its optical limiting effect in polymethylmethacrylate," Nanotechno. 27, 414005(2016).
7. C. Y. Tang, P. K. Cheng, L. Tao, H. Long, L. H. Zeng, Q. Wen, Y. H. Tsang, "Passively Q-Switched Nd: YVO4 Laser Using WS2 Saturable Absorber Fabricated by Radio Frequency Magnetron Sputtering Deposition," J. Light. Techno. 35, 4120-4124(2017).
8. Y. Shi, H. Long, S. Liu, Y. H. Tsang, Q. Wen, "Ultra-small 2D NbSe2 based quantum dots used for low threshold ultrafast lasers," J. Mater. Chem. C. 6, 12638-12642(2018).
9. X. Wang, P. K. Cheng, C. Y. Tang, H. Long, H. Yuan, L. Zeng, S. Ma, W. Qarony, Y. H. Tsang, "Laser Q-switching with PtS2 microflakes saturable absorber," Opt. Express 26, 13055-13060(2018).
10. L. Tao, X. Huang, J.He, Y. Lou, L. Zeng, Y. Li, H. Long, J. Li, L. Zhang, Y. H. Tsang, "Vertically standing PtSe2 film: a saturable absorber for a passively mode-locked Nd: LuVO4 laser,"   Photon. Res. 6, 750-755(2018).
11. M. L. Tsai, S. H. Su, J. K. Chang, D. S. Tsai, C. H. Chen, C. I. Wu, L. J. Li, L. J. Chen, J. H. He, "Monolayer MoS2 Heterojunction Solar Cells,"ACS Nano. 8, 8317–8322(2014).
12. M. Bernardi, M. Palummo, J. C. Grossman, "Extraordinary Sunlight Absorption and One Nanometer Thick Photovoltaics Using Two-Dimensional Monolayer Materials," Nano Lett. 13,   3664–3670(2013).
13. Z. X. Zhang, L. H. Zeng, X.W. Tong, Y. Gao, C. Xie, Y. H. Tsang, L. B. Luo, Y. C.Wu, "Ultrafast, Self-Driven, and Air-Stable Photodetectors Based on Multilayer PtSe2/Perovskite Heterojunctions," J. Phys. Chem. Lett. 9 1185–1194(2018).
14. L. Zeng, L. Tao, C. Y. Tang, B. Zhou, H. Long, Y. Chai, S. P. Lau, Y. H. Tsang, "High-responsivity UV-Vis Photodetector Based on Transferable WS2 Film Deposited by Magnetron Sputtering," Scient. Rep. 6, 20343(2016).
15. Z. Sun, A. Martinez, F. Wang, "Optical modulators with 2D layered materials," Nat. Photon. 10, 227–238(2016).
16. I. R. Whittall, A. M. McDonagh, M. G. Humphrey, M. Samoc, "Organometallic complexes in nonlinear optics II: third-order nonlinearities and optical limiting studies," Adv. in organometallic chem. 43, 349-405(1999).
17. J. K. Anthony, H. C. Kim, H. W. Lee, S. K. Mahapatra, H. M. Lee, C. K. Kim, and F. Rotermu, "Particle size-dependent giant nonlinear absorption in nanostructured Ni-Ti alloys," Opt. Exp. 16(15), 11193-11202(2008).
18. S. Hughes, G. Spruce, B. S. Wherrett, K. R. Welford, and A. D. Lloyd, "The saturation limit to picosecond, induced absorption in dyes," Opt. Commun. 100(1-4), 113-117(1993).
19. P. P. Kiran, D. R. Reddy, B. G. Maiya, A. K. Dharmadhikari, G. R. Kumar, and D. N. Rao, "Nonlinear absorption properties of 'axial-bonding'type tin (IV) tetratolylporphyrin based hybrid porphyrin arrays," Opt. Commun. 252(1-3), 150-161(2005).
20. T. Boggess, K. Bohnert, K. Mansour, S. Moss, I. Boyd, A. Smirl, "Simultaneous measurement of the two-photon coefficient and free-carrier cross section above the bandgap of crystalline silicon," IEEE J. quant. electron. 22 360-368(1986).
21. C. Backes, R. J. Smith, N. McEvoy, N. C. Berner, D. McCloskey, H. C. Nerl, A. O. Neill, P. J. King, T. Higgins, D. Hanlon, N. Scheuschner, J. Maultzsch, L. Houben, G. S. Duesberg, J. F. Donegan, V. Nicolosi, J. N. Coleman, "Edge and confinement effects allow in situ measurement of size and thickness of liquid-exfoliated nanosheets," Nat. Commun. 5, 4576(2014).
22. X. Yin, Z. Ye, D. A. Chenet, Y. Ye, K. O. Brien, J. C. Hone, X. Zhang, "Edge nonlinear optics on a MoS2 atomic monolayer," Science 344, 488-490(2014).
23. Y. H. Lin, C. Y. Yang, J. H. Liou, C. P. Yu, and G. R. Lin, "Using graphene nano-particle embedded in photonic crystal fiber for evanescent wave mode-locking of fiber laser," Opt. Exp. 21(14), 16763-16776(2013).
24. L. Tao, B. Zhou, G. Bai, Y. Wang, S. F. Yu, S. P. Lau, Y. H. Tsang, J. Yao, D. Xu, "Fabrication of covalently functionalized graphene oxide incorporated solid-state hybrid silica gel glasses and their improved nonlinear optical response,"   J. Phys. Chem. C 117, 23108-23116(2013).
25. G. Liang, L. Zeng, Y. H. Tsang, L. Tao, C. Y. Tang, P. K. Cheng, H. Long, X. Liu, J. Li, J. Qu, Q. Wen, "Technique and model for modifying the saturable absorption (SA) properties of 2D nanofilms by considering interband exciton recombination," J. Mater. Chem. C. 6 , 7501-7511(2018).
26. P. K. Cheng, , et al. "Passively Q-switched and femtosecond mode-locked erbium-doped fiber laser based on a 2D palladium disulfide (PdS 2) saturable absorber." Photonics Research 8.4, 511-518(2020).

CHAPTER 6
Conclusion

6.1 Conclusion

In this thesis, the research work is mainly focused on the explorations of the nonlinear optical properties of novel two-dimensional layered transition metal dichalcogenides, where the TMDs materials were applied as saturable absorber and installed into different laser cavity to induce ultrashort laser pulses generation.

The applied laser systems include of diode-end-pumped solid-state (DPSS) Nd:YVO$_4$ laser and Erbium-doped fibre ring cavity laser. And the studies on materials NOA properties began with the promising nonlinear TMD, group 6 tungsten disulfide (WS$_2$). The WS$_2$ saturable absorber was fabricated by a two-step synthesis method, which consists of RF magnetron sputtering deposition of WS$_2$ precursor and followed by a post-annealing treatment. The synthesised WS$_2$ thin film was deposited on a highly-transmissive quartz substrate to act as a transmission type saturable absorber and inserted within a DPSS Nd: YVO$_4$ laser cavity to test the corresponding NOA properties. Restricted by the experimental conditional, Q-switched operation was solely be demonstrated, where maximum single pulse energy of 145 nJ was achieved and is comparable to the results of others WS$_2$-SA-based Q-switched laser, including erbium-doped fibre laser (EDFL) and ytterbium-doped fibre laser (YDFL). This work has enriched the understanding of the applicability of WS$_2$-SA in diverse laser systems. Meanwhile, in the two-step synthesis process, experiences of controlling the material qualities

of TMDs materials were obtained, in which different synthesis parameters, such as the thickness of the precursor thin film, post-annealing time and temperature profile will significantly affect to the nanosheets growth direction, crystalline structure and stoichiometry ratio of the synthesised TMDs thin film. These experiences had built the foundation of the successor works of applying vertically aligned group 10 TMDs to fabricate high-efficient photodetector and image sensor, which was demonstrated and published in high-quality Journal.

To move on, the NOA study of TMDs material had also extended to group 10 air-stable candidates, which both PtS_2 saturable absorber and $PtTe_2$ saturable absorber-based passively mode-locked EDFLs were experimentally demonstrated. Two separate synthesis methods were applied to fabricate the saturable absorbers. For the PtS_2 saturable absorber, the ultrasonic exfoliated PtS_2 nanosheets were incorporated within polyvinyl alcohol (PVA) polymer to form a matrix composite thin film and followed by sandwiching between two FC/APC fibre connectors to act as a transmission type saturable absorber. And for the $PtTe_2$-SA, the ultrasonic exfoliated $PtTe_2$ nanosheets were deposited onto the evanescent-field region of a side-polished single-mode fibre. It is found that incorporation method of the saturable absorber will prominently interfere with the passively mode-locking performance, especially the thermal-induced damge problem and the laser stability. The achieved pulse duration of the mode-locked EDFLs are 2.064 ps and 1.66 ps corresponding to the PtS_2 saturable absorber and $PtTe_2$ saturable absorber, respectively, which are comparable to other low dimensional materials-based results. It indicates that both of the platinum-based TMDs can apply as a promising nonlinear saturable absorber. To the best of our knowledge, the demonstrations of

mode-locked EDFLs based on PtS$_2$ saturable absorber and PtTe$_2$ saturable absorber are a pioneer study within the nonlinear photonic field and has not been reported previously.

After the study works on the ultrafast laser pulses generation, the NOA dependence on the lateral size and layer thickness of PtS$_2$ nanosheets was also demonstrated. By using the individual centrifugation method with distinct centrifugal forces, four PtS$_2$-NMP suspension samples with different distributions of lateral dimension and thickness were prepared. The samples are named as S3000, S5000, S7000, S9000, corresponding to the centrifugal speed of 3000 rpm (Relative Centrifugal Force RCF:1008 g), 5000 rpm (RCF:2800 g), 7000 rpm (RCF: 5488 g), and 9000 rpm (RCF: 9072 g), respectively. The AFM measurement shows that the average PtS$_2$ nanosheets lateral size and layer thickness dropped from around 565 nm to 110 nm, and 30 nm to 10 nm, respectively, as the centrifugation speed raised from 3000 rpm to 9000 rpm. By the Z-scan measurement, it shows that as the PtS$_2$ nanosheets lateral dimension and layer thickness reduced, it will enhance the excited state photon absorption (ESA) effect and two-photon absorption (TPA) effect, which promoted the reverse saturable absorption (RSA) response of the PtS$_2$ samples. As the sample S3000 is already close to the saturation limit of the RSA response, further enhancement of photon absorption was resulting in a weakening of the RSA response, and eventually induced a change of the NOA behaviour from RSA of sample S3000 to saturable absorption (SA) of sample S9000. This work provides the method and strategy for further optimising the group 10 Pt/Pd-based saturable absorber performance by modifying the morphological features of the TMDs nanosheets.

6.2 Future works

As emphasised previously, ambient air stability is a critical factor for commercialising the newly-developed functional materials as nonlinear photonic devices. Our future works will mainly focus on the air-stable group 10 TMDs family. The NOA properties study, as well as the fabrication of group 10 TMDs-based saturable absorber, will extend to the palladium (Pd) based family, where preliminary works on the manufacturing of PdS_2 and $PdSe_2$ saturable absorber is in progress.

Second, the application of the group 10 TMDs in diverse laser systems is also worth to be further studies, where we had preliminarily applied the PtS_2 and $PtTe_2$ saturable absorber in the 1 μm ytterbium-doped fibre ring cavity for laser pulses generation. The parameters of the absorbers, including of modulation depth, initial transmission ratio, need to be further optimised to adjust to the laser system with different operational wavelength. Meanwhile, the group 10 TMDs absorber will also apply to compact DPSS and waveguide laser system.

Third, the NOA properties of group 10 TMDs materials will be comprehensively investigated, in which the NOA response of group 10 TMDs in different pulse duration regime, from nanosecond to femtosecond will be studied in order to analyse the relation between the electronic structure and the NOA response of the Pt/Pd-based TMDs materials.

Appendix

ABCD matrix program code(for simulation the radius variation of the lasing mode with the solid-state laser cavity):

```
% lasing cavity with thermal lensing effects introduced by the pumped
% crystals in (mm)
clc;
clear;
R1=;      % M1
R2=;      % M2 concave mirror 808HT 1064HR coating
R3=;      % M3 thermal lensing
R4=;      % M4 Output coupler Transmission mirror T=20% with 2-degree cutting
n=1;
lambda=1.064*10^-3;      % wavelength in mm scale
d1=;     %Distance between M1 and M2
d2=;     %Distance between M2 and M3
d3=;     %Distance between M3 and M4
m=d1+d2+d3;    %Total cavity length (mm)

for x=0:1:m

    if (x>=0&&x<=d1) %begin from any one point of the back of M1
      m1=[1,x;0,1];
      m2=[1,0;-2/R1,1];
      m3=[1,d1;0,1];
      m4=[1,0;-2/R2,1];
      m5=[1,d2;0,1];
      m6=[1,0;-2/R3,1];
      m7=[1,d3;0,1];
      m8=[1,0;-2/R4,1];
      m9=[1,d3;0,1];
      m10=[1,0;-2/R3,1];
      m11=[1,d2;0,1];
      m12=[1,0;-2/R2,1];
      m13= [1,d1-x;0,1];

    elseif (x>d1&&x<=d1+d2)    %begin from any one point of the back of M2
      m1=[1,x-d1;0,1];
      m2=[1,0;-2/R2,1];
      m3=[1,d1;0,1];
      m4=[1,0;-2/R1,1];
      m5=[1,d1;0,1];
      m6=[1,0;-2/R2,1];
      m7=[1,d2;0,1];
```

```matlab
            m8=[1,0;-2/R3,1];
            m9=[1,d3;0 1];
            m10=[1,0;-2/R4,1];
            m11=[1,d3;0 1];
            m12=[1,0;-2/R3,1];
            m13=[1,d1+d2-x;0,1];

        else
            m1=[1,x-d1-d2;0,1];          %begin from any one point of the back of M3
            m2=[1,0;-2/R3,1];
            m3=[1,d2;0,1];
            m4=[1,0;-2/R2,1];
            m5=[1,d1;0,1];
            m6=[1,0;-2/R1,1];
            m7=[1,d1;0,1];
            m8=[1,0;-2/R2,1];
            m9=[1,d2;0 1];
            m10=[1,0;-2/R3,1];
            m11=[1,d3;0,1];
            m12=[1,0;-2/R4,1];
            m13=[1,d1+d2+d3-x;0,1];
        end

M=m1*m2*m3*m4*m5*m6*m7*m8*m9*m10*m11*m12*m13;
        a=M(1,1);
        b=M(1,2);
        c=M(2,1);
        d=M(2,2);
        if (abs((a+d)/2)<=1)
            w(n)=sqrt(lambda*abs(b)/(pi*sqrt(1-((a+d)/2)^2)));
            y(n)=x;
            z(n) =abs((a+d)/2);
            n=n+1;
        end
end
plot(y,w,'r');
hold on;
xlabel('Position within the laser cavity (mm)');
ylabel('Lasing mode radius (mm)');
title('Lasing mode radius for the 4 mirror cavity')
plot(y,z,'r');
hold on;
Y = y';
W = w';
C = horzcat(Y, W);
xlswrite('LD1.xls', C);
```

List of abbreviations

1. Two-dimensional layered transition metal dichalcogenides(2D-TMDs)
2. Diode-end-pumped solid-state (DPSS)
3. Erbium-doped fiber laser (EDFL)
4. Nonlinear optical absorption (NOA)
5. Tungsten disulfide (WS_2)
6. Saturable absorber (SA)
7. Platinum disulfide (PtS_2)
8. Platinum ditelluride ($PtTe_2$)
9. Excited state photon absorption (ESA)
10. Two-photon absorption (TPA)
11. Reverse saturable absorption (RSA)
12. Nonlinear optical absorption (NOA)
13. Acousto-Optical Modulators (AOM)
14. Electro-Optical Modulators (EOM)
15. Semiconductor saturable absorber mirror (SESAM)
16. Metal oxide chemical vapor deposition (MOCVD)
17. Gallium arsenide (GaAs)
18. Silicon (Si)
19. N- methyl-2-pyrrolidone (NMP)
20. N-vinyl-2-pyrrolidone (NVP)
21. Isopropanol (IPA)
22. Dimethyl sulfoxide (DMSO)
23. Dimethylformamide (DMF)
24. Polyvinyl alcohol (PVA)
25. Electron density of state (eDOS)
26. Continuous wave (CW)
27. Radio frequency (RF)
28. Direct-current (DC)
29. Highly reflective (HR)
30. Highly transmissive (HT)
31. Partially transmissive (PT)
32. Output coupler (OC)
33. Wavelength-division multiplexer (WDM)